



**TÉCNICO**  
LISBOA

## **Autonomous orbit control of a LEO spacecraft**

**Bruno Filipe Antunes Midões**

Thesis to obtain the Master of Science Degree in

### **Aerospace Engineering**

Supervisors: Prof. Pedro Tiago Martins Batista  
Dr. Sérgio Daniel Gonçalves Gante Brás

#### **Examination Committee**

Chairperson: Prof. Jorge Manuel dos Santos Ribeiro Fernandes  
Supervisor: Dr. Sérgio Daniel Gonçalves Gante Brás  
Member of the Committee: Dr. Pedro António Duarte Marques Lourenço

**December 2023**



*To my grandfather,  
for teaching me the joy in mathematics.*



## Declaration

I declare that this document is an original work of my own authorship and that it fulfills all the requirements of the Code of Conduct and Good Practices of the Universidade de Lisboa.



## **Acknowledgments**

Firstly, I would like to thank my supervisors, Prof. Pedro Batista and Dr. Sérgio Brás, for the invaluable support they provided throughout all the stages of this work. Without their insight and care, the development of this thesis would have been nothing short of impossible.

A special thanks to my family for the years of support and patience that cannot be understated. My appreciation goes out to my parents, my grandparents, and my sister, who I deeply cherish.

Finally, I also have to express my gratitude to my friends and colleagues. Thank you for making my days more interesting.



## Resumo

De modo a continuar a explorar órbitas terrestres baixas de forma economicamente viável, a indústria aeroespacial necessita de soluções de controlo orbital eficientes e de baixo custo. Devido a recentes inovações em tecnologias de propulsão elétrica e à possibilidade emergente de implementação de *software* complexo a bordo de satélites, os sistemas de controlo orbital autónomo surgem como a solução mais indicada para satisfazer esta procura. Na presente dissertação, o problema de controlo orbital é formulado como um problema de voo em formação, no qual o satélite líder (virtual) cumpre os requisitos da missão. A dinâmica do problema é descrita utilizando um modelo linear periódico discreto que exhibe precisão comparável a modelos não lineares presentes na literatura. De modo a desenvolver um regulador linear-quadrático para controlo orbital, propõe-se um algoritmo eficiente para a solução da equação de Riccati periódica discreta. A solução de controlo desenvolvida na presente dissertação controla todos os elementos Keplerianos, apresentando consumo reduzido de combustível e dependendo apenas de atuação na direção transversal e perpendicular ao plano da órbita. O método proposto explora, de forma notável, a mecânica orbital inerente ao problema, priorizando manobras em locais ótimos ao longo da órbita. Simulações realizadas num propagador de alta fidelidade mostram que o controlador desenvolvido atinge um seguimento da órbita de referência mais preciso, com menor consumo de combustível, do que um dos métodos mais eficientes de controlo orbital, desenvolvido para a missão PRISMA. Por fim, o algoritmo desenvolvido é validado também para correção de erros de injeção na órbita.

**Palavras-chave:** Controlo orbital autónomo, satélite em órbita terrestre baixa, equação de Riccati periódica discreta, propulsão elétrica



## Abstract

The increasing number of satellites orbiting Earth, alongside recent advances in electric propulsion technologies and in on-board computational capability, call for novel autonomous orbit control solutions. In this thesis, the orbit control problem is formulated as a formation keeping problem, where the reference spacecraft fulfills the mission requirements. Taking advantage of the periodic characteristics of a satellite's orbit, a discrete-time linear periodic model of the relevant dynamics is developed. The proposed model is shown to have comparable accuracy to nonlinear models of the same dynamics found in the literature. A novel solution for the discrete-time periodic Riccati equation (DPRE) is proposed, and then leveraged in the design of a linear-quadratic regulator (LQR) for autonomous orbit control. The proposed algorithm for the solution of the DPRE is computationally efficient and can be applied to singular systems, contrary to some alternative algorithms. The control system proposed in this thesis achieves accurate reference tracking of all Keplerian elements, with low fuel consumption, resorting solely to transverse and normal actuation. Notably, the control algorithm leverages the dominant orbital mechanics of the problem, prioritizing station-keeping maneuvers at the optimal locations along the orbit, while remaining computationally light. Resorting to high-fidelity simulations, it is shown that the proposed control algorithm attains more accurate reference tracking, with lower fuel consumption, than an autonomous orbit control system designed for the PRISMA mission: one of the most precise orbit control systems found in the literature. Lastly, the control system is also validated for the correction of orbit injection errors.

**Keywords:** Autonomous orbit control, LEO spacecraft, discrete-time periodic Riccati equation, electric propulsion



# Contents

|  |          |
|--|----------|
| Acknowledgments . . . . .                        | vii      |
| Resumo . . . . .                                 | ix       |
| Abstract . . . . .                               | xi       |
| List of Tables . . . . .                         | xvii     |
| List of Figures . . . . .                        | xix      |
| Nomenclature . . . . .                           | xxi      |
| Acronyms . . . . .                               | xxv      |
| <b>1 Introduction</b>                            | <b>1</b> |
| 1.1 Motivation . . . . .                         | 1        |
| 1.2 State of the art . . . . .                   | 2        |
| 1.3 Objectives . . . . .                         | 4        |
| 1.4 Contributions . . . . .                      | 5        |
| 1.5 Thesis Outline . . . . .                     | 6        |
| <b>2 Background</b>                              | <b>7</b> |
| 2.1 Reference frames . . . . .                   | 7        |
| 2.1.1 Geocentric frame . . . . .                 | 7        |
| 2.1.2 Satellite coordinate systems . . . . .     | 8        |
| 2.2 Orbital Mechanics . . . . .                  | 9        |
| 2.2.1 The two-body problem . . . . .             | 9        |
| 2.2.2 Keplerian element representation . . . . . | 10       |
| 2.3 Perturbations . . . . .                      | 11       |
| 2.3.1 Earth's oblateness . . . . .               | 12       |
| 2.3.2 Atmospheric drag . . . . .                 | 14       |
| 2.3.3 Third-body perturbations . . . . .         | 16       |
| 2.3.4 Solar radiation pressure . . . . .         | 16       |
| 2.3.5 Other perturbations . . . . .              | 17       |
| 2.3.6 Perturbed motion . . . . .                 | 17       |
| 2.4 Sensors and actuators . . . . .              | 21       |
| 2.4.1 Sensors . . . . .                          | 21       |

|          |  |           |
|----------|--|-----------|
| 2.4.2    | Actuators . . . . .  | 22        |
| 2.5      | Control methodology . . . . .  | 25        |
| <b>3</b> | <b>Problem statement</b>   | <b>27</b> |
| 3.1      | Modelling the effects of the main perturbations . . . . .                    | 27        |
| 3.1.1    | Atmospheric drag . . . . .   | 27        |
| 3.1.2    | Earth's gravitational field . . . . .  | 29        |
| 3.2      | Nonlinear model . . . . .  | 30        |
| <b>4</b> | <b>On the LQR design for discrete-time linear periodic systems</b>           | <b>33</b> |
| 4.1      | Preliminaries . . . . .  | 34        |
| 4.1.1    | Equivalent augmented linear time-invariant system . . . . .                  | 35        |
| 4.1.2    | Efficient LQR design for the augmented system . . . . .                      | 36        |
| 4.2      | Feedback of the most recent state . . . . .                                  | 37        |
| 4.2.1    | Proposed solution for singular $\tilde{A}$ . . . . .                         | 40        |
| 4.2.2    | Algorithm . . . . .  | 41        |
| 4.3      | Numerical results and algorithm efficiency . . . . .                         | 41        |
| <b>5</b> | <b>Periodic model of the orbital motion</b>                                  | <b>45</b> |
| 5.1      | Linearized dynamic model . . . . .   | 45        |
| 5.1.1    | Open-loop poles . . . . .  | 47        |
| 5.2      | Periodic approximation . . . . .   | 48        |
| 5.2.1    | Time-invariant state matrix . . . . .  | 48        |
| 5.2.2    | Periodic input matrix . . . . .  | 50        |
| 5.2.3    | Discrete-time linear periodic system . . . . .                               | 51        |
| 5.3      | Model validation . . . . .   | 51        |
| 5.3.1    | Validation with a high-fidelity simulator . . . . .                          | 54        |
| 5.3.2    | Effect of the Earth's gravitational field and the atmospheric drag . . . . . | 56        |
| <b>6</b> | <b>Controller design and simulation results</b>                              | <b>59</b> |
| 6.1      | LQR design and controller validation . . . . .                               | 59        |
| 6.2      | PRISMA mission . . . . .   | 63        |
| 6.2.1    | Relative Earth-fixed elements . . . . .                                      | 63        |
| 6.2.2    | PRISMA's linear feedback methodology . . . . .                               | 65        |
| 6.2.3    | LQR design: relative Earth-fixed elements . . . . .                          | 66        |
| 6.2.4    | Ideal simulation scenario . . . . .  | 67        |
| 6.2.5    | Realistic simulation scenario . . . . .                                      | 71        |
| 6.3      | Orbit injection . . . . .  | 76        |
| <b>7</b> | <b>Conclusions</b>   | <b>79</b> |
| 7.1      | Future Work . . . . .  | 80        |

|   |           |
|---|-----------|
| <b>Bibliography</b>   | <b>81</b> |
| <b>A Linear model's state and input matrices</b>                | <b>87</b> |
| <b>B Addendums to Chapter 4</b>                                 | <b>91</b> |
| B.1 Necessary conditions for the solution of the DPRE . . . . . | 91        |
| B.2 Solution to the augmented Riccati equation . . . . .        | 92        |
| B.3 Structure of the augmented state feedback matrix . . . . .  | 94        |
| B.4 Equivalence of the Riccati solutions . . . . .              | 95        |
| B.5 Validation for singular systems . . . . .                   | 96        |



# List of Tables

|      |  |    |
|------|--|----|
| 2.1  | Some coefficients of the GRACE GGM02C Earth gravity field model . . . . .                    | 14 |
| 2.2  | GNSS receivers for space applications . . . . .  | 22 |
| 2.3  | Efficiency of various propulsion technologies . . . . .                                      | 23 |
| 4.1  | Execution time comparison for a synthetic system . . . . .                                   | 43 |
| 5.1  | Initial state of the reference orbit . . . . .   | 47 |
| 5.2  | Main parameters of the MANGO spacecraft . . . . .  | 48 |
| 5.3  | Propagation parameters and perturbations considered by the high-fidelity simulator . . . . . | 54 |
| 6.1  | Performance and maneuver budget . . . . .  | 62 |
| 6.2  | Design parameters . . . . .  | 66 |
| 6.3  | Main characteristics - Ideal scenario . . . . .  | 71 |
| 6.4  | Absolute navigation accuracy - PODRIX GNSS receiver . . . . .                                | 71 |
| 6.5  | Orbit determination accuracy with data from the PODRIX GNSS Receiver . . . . .               | 72 |
| 6.6  | PRISMA's propulsion system: performance parameters . . . . .                                 | 72 |
| 6.7  | Alta's FT-150 Thruster: performance parameters. . . . .                                      | 72 |
| 6.8  | Main characteristics - Realistic scenario . . . . .  | 76 |
| 6.9  | Ariane 6 launcher's sun-synchronous orbit injection accuracy . . . . .                       | 76 |
| 6.10 | 4x QinetiQ T5 ion thrusters: performance parameters . . . . .                                | 76 |



# List of Figures

|      |   |    |
|------|---|----|
| 2.1  | Geometry of the vernal equinox . . . . .  | 8  |
| 2.2  | RTN and MVH coordinate frames . . . . .   | 9  |
| 2.3  | Classical orbital elements on a geocentric-equatorial frame . . . . .   | 11 |
| 2.4  | Magnitude of the main perturbations on a geocentric orbit . . . . .   | 12 |
| 2.5  | Spatial structure of spherical harmonics . . . . .  | 13 |
| 2.6  | Osculating and true orbits . . . . .  | 18 |
| 2.7  | Effects of perturbations on an orbital element . . . . .  | 20 |
| 2.8  | Thrust and specific impulse provided by some propulsion technologies . . . . .                                    | 24 |
| 4.1  | Effect of process noise on both feedback methodologies . . . . .  | 42 |
| 5.1  | Evolution of the non-null eigenvalues of the time-varying state matrix over 10 orbits . . . . .                   | 48 |
| 5.2  | Evolution of the eigenvalues of the non-periodic and the periodic state matrices . . . . .                        | 50 |
| 5.3  | Evolution of the relative orbital element vector for spacecraft in free fall . . . . .                            | 52 |
| 5.4  | Difference between the results of the nonlinear model and the linear models (free fall) . . . . .                 | 52 |
| 5.5  | Difference between the results of the nonlinear model and the linear models (with constant actuation) . . . . .   | 53 |
| 5.6  | Evolution of the relative orbital element vector for a spacecraft in free fall . . . . .                          | 54 |
| 5.7  | Difference between propagation with a high-fidelity simulator and the LTP model (free fall) . . . . .             | 55 |
| 5.8  | Difference between propagation with linear model and high-fidelity simulator (free fall) . . . . .                | 56 |
| 5.9  | Difference between propagation with a high-fidelity simulator and the LTP model . . . . .                         | 56 |
| 5.10 | Evolution of the relative orbital element vector (considering drag and the Earth's gravitational field) . . . . . | 57 |
| 6.1  | Along-track optimal periodic feedback gains over a reference orbit . . . . .                                      | 60 |
| 6.2  | Cross-track optimal periodic feedback gains over a reference orbit . . . . .                                      | 61 |
| 6.3  | Distance between real and virtual spacecraft . . . . .  | 62 |
| 6.4  | Evolution of the relative orbital elements over one month . . . . .   | 62 |
| 6.5  | Executed maneuvers, in terms of delta-v per time step . . . . .   | 63 |
| 6.6  | Geometry of the relative Earth-fixed elements . . . . .   | 64 |
| 6.7  | Evolution of the relative Earth-fixed elements (at the ascending node) . . . . .                                  | 67 |
| 6.8  | Evolution of the relative orbital elements . . . . .  | 68 |

|   |    |
|---|----|
| 6.9 Executed maneuvers for the impulsive control scheme . . . . .                                   | 69 |
| 6.10 Executed maneuvers for the proposed continuous control scheme . . . . .                        | 69 |
| 6.11 Continuous maneuvers executed between orbits 20 and 35 . . . . .                               | 70 |
| 6.12 Distance between the true and the reference orbit . . . . .                                    | 70 |
| 6.13 Thrust accuracy of Alta's microthruster at nominal temperature . . . . .                       | 73 |
| 6.14 Evolution of the relative Earth-fixed elements - Realistic scenario . . . . .                  | 74 |
| 6.15 Evolution of the relative orbital element vector - Realistic scenario . . . . .                | 74 |
| 6.16 Executed maneuvers for the impulsive control scheme - Realistic scenario . . . . .             | 75 |
| 6.17 Executed maneuvers for the continuous control scheme - Realistic scenario . . . . .            | 75 |
| 6.18 Evolution of the relative orbital element vector . . . . .                                     | 77 |
| 6.19 Executed maneuvers . . . . .   | 78 |
| 6.20 Distance between the reference and the true spacecraft . . . . .                               | 78 |
| <br>  |    |
| B.1 Evolution of the state vector of a system with a singular $\tilde{\mathbf{A}}$ matrix . . . . . | 96 |

# Nomenclature

The following list describes several symbols that are consistently utilized along the body of the present thesis. Matrices are denoted in bold typeface and uppercase. Vectors are denoted in bold typeface and lowercase. Scalars are displayed in light typeface.

## Greek symbols

|                   |   |
|-------------------|---|
| $\epsilon$        | Relative orbital element vector.          |
| $\xi$             | Mean orbital element vector difference.   |
| $\lambda$         | Longitude.                                |
| $\mu$             | Standard gravitational parameter.         |
| $\Omega$          | Right ascension of the ascending node.    |
| $\omega$          | Argument of perigee.                      |
| $\omega_{\oplus}$ | Angular velocity of the Earth's rotation. |
| $\rho$            | Atmospheric density.                      |
| $\varphi$         | Latitude.                                 |
| $v$               | True anomaly.                             |

## Roman symbols

|                          |  |
|--------------------------|--|
| $a_M, a_V, a_H$          | Acceleration components in an MVH reference frame.                 |
| $a_R, a_T, a_N$          | Acceleration components in an RTN reference frame.                 |
| $\Delta \mathbf{v}$      | Velocity increment vector in an RTN reference frame.               |
| $\Delta \mathbf{v}_2$    | Velocity increment vector in the transverse and normal directions. |
| $\delta a$               | Relative semi-major axis.  |
| $\delta e_x, \delta e_y$ | Components of the relative eccentricity vector.                    |
| $\delta h$               | Normalized altitude difference.                                    |

|                                      |   |
|--------------------------------------|---|
| $\delta i_x$                         | Relative orbit inclination.                   |
| $\delta i_y$                         | Relative ascending node.                      |
| $\delta L_\lambda, \delta L_\varphi$ | Components of the phase difference vector.    |
| $\Delta t$                           | Duration of a station-keeping maneuver.       |
| $\delta u$                           | Relative argument of latitude.                |
| $\Delta v$                           | Delta-v: impulse per unit of spacecraft mass. |
| $\ell$                               | Semi-latus rectum.                            |
| <b>A</b>                             | State matrix.                                 |
| <b>B</b>                             | Input matrix.                                 |
| <b>k</b>                             | Mean orbital element vector.                  |
| $\mathbf{k}_{\text{osc}}$            | Osculating orbital element vector.            |
| <b>r</b>                             | Position vector.                              |
| <b>u</b>                             | Input.  |
| <b>v</b>                             | Velocity vector.                              |
| $\mathbf{w}_r$                       | Sensor noise.                                 |
| <b>x</b>                             | State.  |
| <b>y</b>                             | Output.                                       |
| <i>A</i>                             | Satellite cross-sectional area.               |
| <i>a</i>                             | Semi-major axis.                              |
| <i>b</i>                             | Semi-minor axis.                              |
| $B^*$                                | Ballistic coefficient.                        |
| $C_d$                                | Drag coefficient.                             |
| <i>e</i>                             | Eccentricity.                                 |
| $e_x, e_y$                           | Components of the eccentricity vector.        |
| <i>G</i>                             | Gravitational constant.                       |
| <i>h</i>                             | Altitude of the spacecraft.                   |
| $h_m$                                | Angular momentum per unit of mass.            |
| <i>i</i>                             | Orbit inclination.                            |

|              |  |
|--------------|--|
| $I_{sp}$     | Specific impulse.                          |
| $M$          | Mean anomaly.                              |
| $m$          | Spacecraft mass.                           |
| $n$          | Mean motion.                               |
| $p$          | Period of a discrete-time periodic system. |
| $R_{\oplus}$ | Earth's (equatorial) radius.               |
| $T$          | Orbital period.                            |
| $U$          | Gravitational potential.                   |
| $u$          | Argument of latitude.                      |
| $v$          | Orbital velocity.                          |

### Subscripts

|          |                            |
|----------|----------------------------|
| $N$      | Across-track (normal).     |
| $R$      | Reference.                 |
| $T$      | Along-track (transversal). |
| $\odot$  | Sun.                       |
| $\oplus$ | Earth.                     |
| sat      | Satellite.                 |

### Superscripts

|     |            |
|-----|------------|
| $T$ | Transpose. |
|-----|------------|



# Acronyms

|             |  |
|-------------|--|
| <b>AOK</b>  | Autonomous Orbit Keeping.                |
| <b>CPU</b>  | Central Processing Unit.                 |
| <b>DPRE</b> | Discrete-time Periodic Riccati Equation. |
| <b>GNSS</b> | Global Navigation Satellite System.      |
| <b>GPS</b>  | Global Positioning System.               |
| <b>LEO</b>  | Low Earth Orbit.                         |
| <b>LQR</b>  | Linear-Quadratic Regulator.              |
| <b>LTI</b>  | Linear Time-Invariant.                   |
| <b>LTP</b>  | Linear Time-Periodic.                    |
| <b>MPC</b>  | Model Predictive Control.                |



# Chapter 1

## Introduction

Since 1957, when the first artificial satellite was launched, thousands more have been placed into orbit, with about 8700 satellites still currently operating [1, 2]. Society depends on satellites for numerous services; they provide information, assure real-time communications, and support global security and defense [3]. The vantage point satellites possess allows them to see large portions of Earth at one time. As a result, satellite technology can collect and distribute data more efficiently than instruments on the ground [4].

### 1.1 Motivation

Out of the 8700 satellites orbiting Earth, almost 8000 occupy a low Earth orbit (LEO) [1, 2]. Low Earth orbits are characterized by being relatively close to the Earth's surface. Their upper bound is often defined as 2000 km, yet satellites in these orbits usually occupy an altitude of less than 1000 km, reaching as low as 160 km [5]. Satellites in low Earth orbit are commonly used for Earth observation missions, which provide vital information used to monitor and evaluate changes in the natural and human-made environment [6]. Low Earth orbits are also home to large satellite constellations, such as Starlink and OneWeb, which aim to provide worldwide broadband coverage [7]. A satellite's proximity to Earth leads to lower response time (latency), higher bandwidth, and diminished radiation damage. It also presents benefits when it comes to end-of-life operations, as de-orbiting is facilitated [8]. Placing a satellite in a low Earth orbit requires the lowest amount of energy, and thus cost, for the satellite launch [9]. This makes LEO very attractive to countries that are not at the forefront of space technology, as only a few institutions are able to launch satellites to higher Earth orbits [10].

During its motion, a satellite is strongly influenced by various perturbations, with diverse magnitudes and directions, disturbing the satellite and leading to deviations from the desired orbit [11]. A satellite's orbit determines its position in the sky, conditioning the data it can gather and communicate. Therefore, orbit maintenance is a common problem in the operation of satellites and is key for the success of most missions [12]. This is particularly true for a satellite in LEO, as the denser atmosphere close to the Earth's surface substantially increases the impact of the atmospheric drag on the satellite's orbit.

Additionally, orbit decay in LEO can lead to a satellite reentering and burning in the atmosphere, resulting in complete mission failure [13].

Orbit control is a well-established concept in traditional space missions. This technique is often dependent on ground operations and fulfills a wide range of applications, from single spacecraft to formation flying orbit control [14, 15]. While orbit control still mostly depends on ground operations, the current landscape of a related system, spacecraft attitude control, is very different. Autonomy in attitude is well established and is considered essential [14]. Yet, a failure in an attitude control system is more dramatic than a failure in an orbit control system, since it can result in an uncontrolled, tumbling spacecraft, while a failure in the orbit control system would only cause the orbit to decay slowly, giving ground operations more time to troubleshoot the problem and take recovery measures. This comparison highlights the fact that the main roadblock to introducing autonomous orbit control is simply tradition. Orbit control has always been done from the ground, and new programs are very risk-averse and slow to embrace the innovative autonomous orbit control systems [14]. Still, autonomous orbit control presents many benefits. It guarantees better accuracy and flexibility than ground based orbit control, and allows for simpler ground operations [16]. Moreover, the implementation of autonomous orbit control would free the staff on-ground to accomplish other tasks. Autonomous orbit control can also lead to significant savings on propellant mass since it allows the use of efficient low-thrust propulsion systems, such as electric propulsion systems [17]. As the required accuracy for orbit control increases, the time between two consecutive orbit-keeping maneuvers becomes smaller and, due to the latency between two consecutive ground station contacts, the choice of an autonomous (on-board) orbit control system becomes the only feasible way to precisely control a spacecraft's orbit [18].

Many recent developments are catalysts for the research of novel autonomous orbit control technologies. First, the augmented CPU capability on-board satellites allows for faster and more accurate orbit propagation, leading to more precise control and decreasing the dependence on on-ground operations [19]. The increase in the amount of satellites in space also strengthens the importance of the implementation of autonomous orbit control, particularly when satellites are utilized as part of large constellations, since the ground operations associated with orbit control must be highly efficient in order to support a complex mission without an oversized ground segment [20]. Furthermore, for small low-cost satellites, ground-based control actions can represent a significant portion of both cost and mission risk. To allow such systems to be economically viable, a need for low-cost, accurate orbit maintenance systems arises [14]. The necessity for accurate low-cost orbit maintenance systems and the emerging possibility to implement complex software on-board a spacecraft call for a paradigm shift in the industry towards autonomous orbit control.

## **1.2 State of the art**

Over the last two decades, several theoretical studies and in-flight demonstrations have been conducted to develop and validate autonomous orbit control systems for LEO satellites [18]. Microcosm was amongst the first companies to work on autonomous orbit control, in the early 1990s, developing

the orbit control kit (OCK) software. Microcosm's OCK aimed to keep the satellite's orbit from decaying, maintaining the satellite in a "box" which kept a predictable position relative to users on the ground [21]. The software was tested in 1999 on the UoSAT-12 mission and, in 2006, on-board the TacSat-2 satellite. The results from these missions demonstrated that the OCK software was capable of autonomously controlling the spacecraft's position in its orbital plane (within about 1 km). Moreover, the algorithm did not require complex orbital mechanics and orbit propagation, as it depended on simple geometric calculations [22]. Despite the success in controlling the spacecraft, the fuel spent in the station-keeping maneuvers was equivalent to what would have been required to return the spacecraft to its initial orbit had all the thrust been applied at the end of the test [21]. In 2004, the French DEMETER (Detection of Electromagnetic Emissions Transmitted from Earthquake Regions) satellite was controlled autonomously, further demonstrating the capability of applying autonomous orbit control as a routine feature without causing any deterioration to the scientific mission of the satellite [23].

The autonomous orbit keeping (AOK) controller, tested on the PRISMA mission in 2011, is one of the most recent and accurate autonomous orbit control methods validated in-flight [18]. The algorithm maintains the ascending node of the orbit within the required tolerance (10 m) by means of along-track maneuvers (i.e. maneuvers along the orbital plane) which adjust the semi-major axis [24]. The following year, a novel control system for the PRISMA mission was validated, via high-fidelity software simulations, revealing better performance than the AOK algorithm [16]. The locations of the maneuvers were decided *a priori*, employing an analytical rule, and the optimal maneuver at the selected location was computed via a linear-quadratic regulator (LQR). An alternative method employing a linear control law based on a simplified model was also validated in [16], displaying similar performance to the LQR. The control system hinged on a linear time-varying model of the relevant dynamics which, however, did not include all the six orbital elements. Moreover, the in-plane and out-of-plane control problems were solved separately.

A control system employing model predictive control (MPC) was proposed in [25]. One of the advantages of this control methodology is that it can guarantee optimality (with respect to some performance measure) while simultaneously satisfying constraints on system states and inputs [26]. The study performed in [25] showed that, in some cases, the fuel consumption for station-keeping can be substantially lower when employing model predictive control instead of LQR. This can be attributed to the fact that LQR, having no inequality constraints, can command an optimal maneuver that leads to the saturation of the actuators, ending up realizing a suboptimal maneuver. Besides, the fuel consumption of the LQR algorithm applied in the PRISMA mission will depend on where the problem is solved, since the maneuver might be calculated and executed in a suboptimal location (decided *a priori*). On the other hand, MPC can predict the behavior of the system and therefore execute a calculated maneuver at the optimal location in the satellite's orbit [25]. Still, MPC is severely limited by its substantial computational complexity, due to the limited CPU capability on-board a satellite.

Nonlinear feedback control laws can be studied as an option to solve the problem at hand. Employing nonlinear control can prove beneficial in improving robustness and in increasing the region of the state space in which the system can be successfully controlled. On the other hand, there are no well-defined

methodologies of choosing gains for the nonlinear control law, and it can be a laborious task to find good values due to the complexity of the system [27]. Finding ways to exploit the dominant orbital mechanics of the problem has been an issue while applying this methodology to orbit control. Ideally, some feedback gains should be maximum for a very short time and practically zero for the remainder of the orbit, in order to perform the maneuvers in the portion of a satellite's orbit where they are known *a priori* to be more effective [27, 28]. A method of choosing suitable feedback gains in order to accomplish this goal was proposed in [28]. With this method, performances of at least similar accuracy to the LQR algorithm applied to the PRISMA mission were achieved. Moreover, the nonlinear control laws proposed in [28] were shown to decrease the reference tracking error to as low as a few meters, even when starting kilometers away from the reference orbit.

Various autonomous orbit control techniques, such as [16, 21, 23, 25], employ chemical propulsion technologies, relying on a few large maneuvers every orbit (or every few orbits). The emergence of efficient electric propulsion techniques enables new control strategies. For instance, a control method employing a low-thrust electric propulsion system was proposed in [17]. This autonomous control system relied on continuous actuation for along-track corrections, employing a Lyapunov-based control methodology, while the cross-track corrections (i.e. maneuvers perpendicular to the orbital plane) were impulsive and computed analytically. The efficiency of the low-thrust electric propulsion system utilized allowed for significant savings on propellant mass, leading to an increase in the spacecraft's lifetime [17].

The autonomous orbit control problem can be described as a formation keeping problem, where the (virtual) reference orbit is affected solely by the Earth's gravitational field. This virtual orbit fulfills the mission requirements, and the real orbit will deviate from this reference due to perturbations (e.g. atmospheric drag, third-body perturbations, and solar radiation pressure). The goal is then to counteract the effects of these perturbations with efficient orbital maneuvers. This definition of a reference orbit is often seen in the literature [16, 17, 25, 28]. A nonlinear model expressing the deviation between the spacecraft's true orbit and the reference orbit can be obtained in order to apply Lyapunov-based analysis, as seen in [17]. An accurate linearized (time-variant) model can be derived in order to employ an LQR or MPC, as shown in [16] and [25], respectively.

### 1.3 Objectives

This thesis is motivated by the advances in electric propulsion technologies, and the needs in orbital station-keeping, which call for novel autonomous, adaptive, and flexible space robotic control solutions. This work aims to develop an autonomous control system which keeps the satellite's orbit close to the reference orbit, counteracting the (undesired) effects of perturbations. Particularly, the aim is set in developing a computationally light control algorithm which, nonetheless, attains accurate reference tracking with minimum fuel usage, leveraging the dominant orbital mechanics of the problem. With this in consideration, the goals of this thesis are:

1. Derive suitable mathematical descriptions of the perturbations affecting a satellite's orbit, in order to characterize the motion of the satellite.

2. Develop a model which describes the effects of perturbations on the orbit of a LEO satellite, with suitable accuracy, and that can be leveraged using advanced control methodologies. Validate the models utilizing the ephemerides resultant from orbital propagation with a high-fidelity simulator.
3. Design a novel automatic control system for single satellites, taking advantage of the derived model, aiming for good reference tracking with minimal fuel usage and low computational cost.
4. Validate the proposed control solution with a high-fidelity orbital simulator, including on-board navigation errors and realistic actuators.

## 1.4 Contributions

Taking advantage of the periodic characteristics of a spacecraft's orbit, a discrete-time linear periodic model expressing the deviation of the true orbit from the reference orbit is developed. While various models of the intended dynamics have been developed, these are either nonlinear [17], or linear time-varying (non-periodic) models [16], limiting the applicability of control techniques. Moreover, the dynamics of the in-plane and out-of-plane motion of the satellite are often separated in the literature, to develop simpler control laws, which often do not maintain all six orbital elements [16, 17]. The proposed linear periodic model includes the full dynamics of the problem and is shown to be very accurate when compared to nonlinear models of the same dynamics found in the literature. Furthermore, it is discussed how the discrete-time linear periodic model can be rewritten as an equivalent linear time-invariant (LTI) model, to which powerful well-known control techniques can be applied. Since the developed LTI system is equivalent to the original linear periodic system, it is likewise very accurate when compared to existing nonlinear models. This is the first major contribution of this work. The development of an accurate linear periodic and an (equivalent) linear time-invariant model, which include the full dynamics of the problem, pave the way for future work employing advanced control solutions.

Another contribution of this thesis is the development of a novel solution to the discrete-time periodic Riccati equation, in order to develop an LQR control solution for the periodic system. The proposed method relies on an algorithm that converts a discrete-time linear periodic system into a linear time-invariant equivalent, whereupon standard techniques for the algebraic Riccati equation can be applied. This solution is computationally efficient and can be applied to singular periodic systems, contrary to alternative algorithms to solve discrete-time periodic Riccati equations.

The control law proposed herein addresses the main shortcomings of autonomous orbit control systems found in the literature. Contrary to various existing methods, the control system proposed efficiently maintains every Keplerian element, resorting solely to maneuvers in the along-track and cross-track directions (i.e. no actuator aligned in the radial direction is required). Moreover, the control system takes full advantage of the orbital dynamics associated with the problem, prioritizing maneuvers at the optimal locations along the orbit. As a result, the developed control strategy allows for tight reference tracking with low fuel consumption. The proposed solution is also computationally light when compared to methods such as MPC; a sizable benefit when implementing software on-board a satellite.

## 1.5 Thesis Outline

The remainder of this thesis is organized as follows. Chapter 2 is composed by a summary of background concepts necessary for the intended research. It consists of a description of the employed reference frames, an introduction to the two-body problem, and a discussion of the effects of perturbations on the motion of a spacecraft. Additionally, commercially available sensors and actuators are presented, alongside an introduction to the control methodology employed. Chapter 3 discusses how the perturbations acting on the spacecraft can be modelled, and how a nonlinear model of the spacecraft's reference and true orbit can be developed. In Chapter 4, an efficient solution to the discrete-time periodic Riccati equation is proposed. The algorithm is validated, and it is shown to be more efficient than existing methods. Chapter 5 includes the development of a linear periodic model for the deviation of the true orbit from the reference orbit. The model is validated, being compared to a nonlinear model, a linear time-varying (non-periodic) model, and the true motion of the spacecraft, obtained via high-fidelity simulations. Chapter 6 provides an overview of the proposed control methodology. The proposed control system is validated and compared with an impulsive control strategy designed for the PRISMA mission. Additionally, the control scheme is validated for the correction of orbit injection errors. Finally, Chapter 7 summarizes the findings of this thesis and discusses future work.

# Chapter 2

## Background

The current chapter offers important background, necessary to set and address the problem of satellite orbit control. Section 2.1 offers insight into suitable reference frames to describe the problem. Section 2.2 presents an introduction to the two-body problem. This theory is a good starting point for the study of orbital motion, however, perturbations acting on the system need to be taken into account to properly model the problem. Section 2.3 describes the most important perturbations, how these can be modelled, and their effects on the motion of a spacecraft. Next, Section 2.4 presents existing sensors and propulsion technologies applicable to orbit control. Lastly, Section 2.5 introduces some basics of the control methodology that is at the root of the proposed design.

### 2.1 Reference frames

The first step for describing an orbit is defining a suitable reference frame [29]. The coordinate systems used to describe orbits in the solar system are typically either heliocentric (Sun-centered) or geocentric (Earth-centered). However, the origin may occasionally be taken at the center of another small body [30]. For a spacecraft orbiting Earth, the most suitable choices of reference frame are a geocentric frame and a frame centered on the orbiting body.

#### 2.1.1 Geocentric frame

The Earth and its orbit around the Sun form the basis of geocentric coordinate systems. The plane of the Earth's mean orbit around the Sun is denominated the ecliptic, and the angle between Earth's equator and the ecliptic is called the obliquity of the ecliptic ( $\gamma \approx 23.5^\circ$ ). The line of intersection between these two planes, denominated line of nodes, aids in fixing a principal direction for the coordinate system, whose reference direction is chosen towards the vernal equinox [31]. The direction of the vernal equinox (often referred to as the first point of Aries) is designated  $\Upsilon$ . This point is defined as the location where the sun crosses the equator from south to north, as seen from Earth [30, 31].

A geocentric-equatorial reference frame can then be characterized by an  $\hat{I}$ -axis pointing in the vernal equinox direction, a  $\hat{K}$ -axis pointing in the direction of the North Pole, and a  $\hat{J}$ -axis which completes

the right-handed set of coordinate axis, as shown in Figure 2.1 [29]. By definition, a geocentric-ecliptical system is inclined in relation to the geocentric-equatorial frame (by the obliquity of the ecliptic). Due to the precession of Earth's polar axis, in a cycle that spans approximately 26000 years, these frames are in motion, and are therefore non-inertial. Theoretical work is done with respect to the equator and equinox of a standard epoch. Currently, the equator and equinox of the year 2000 are in use (J2000 Earth-centered inertial frame). In order to obtain accurate data from observing instruments, the epoch of the standard frame is occasionally changed. The next change will happen in 2025 [32].

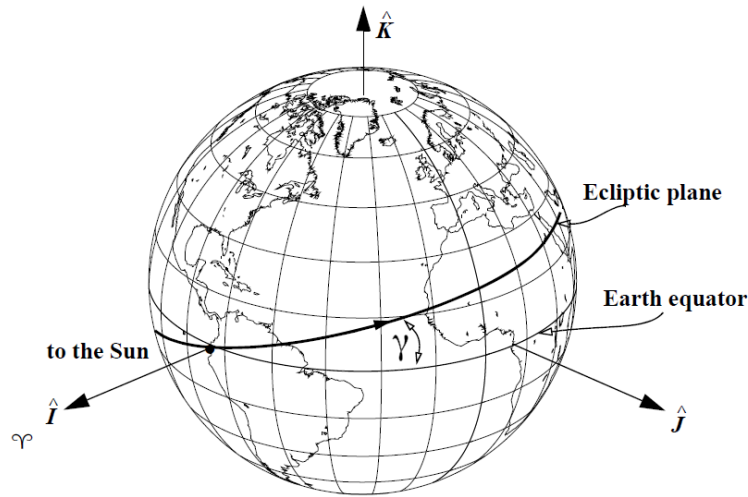


Figure 2.1: Geometry of the vernal equinox. Adapted from [31].

## 2.1.2 Satellite coordinate systems

The satellite coordinate systems, centered on the orbiting body, can be applied to studies of the relative motion of a spacecraft. Such a system is the so called RTN (Radial-Transverse-Normal) frame, composed by an  $\hat{R}$  axis pointing along the radius vector (from the Earth to the satellite), a  $\hat{T}$  axis which is closely aligned with the satellite's velocity, and an  $\hat{N}$  axis normal to the orbital plane, along the angular momentum vector, in order to complete the right-handed coordinate system. The  $\hat{T}$  axis is not necessarily parallel to the satellite's velocity. However, this is always the case for circular orbits. Radial displacements are often defined as being parallel to the position vector ( $\hat{R}$  axis). Along-track displacements are normal to the position vector (along the  $\hat{T}$  axis), and cross-track displacements are normal to the orbital plane (along the  $\hat{N}$  axis) [31].

It can be beneficial to have an axis aligned with the satellite's velocity, instead of having an axis aligned with the radius vector. In this case, an MVH frame can be employed, where the  $\hat{V}$  axis is aligned with the satellite's velocity vector, the  $\hat{M}$  vector is closely aligned with the radius vector, and the  $\hat{H}$  axis completes the right-handed coordinate system. The  $\hat{M}$  axis is not necessarily parallel to the radius vector. However, this is always the case for circular orbits [31]. These two local (non-inertial) frames are represented in Figure 2.2. For near-circular orbits, the difference between these frames is small (as the velocity is almost normal to the radius vector), and these frames coincide for circular orbits.

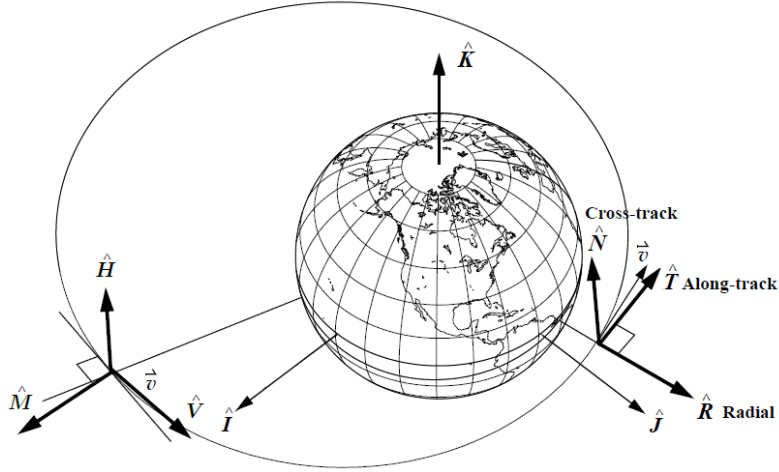


Figure 2.2: RTN and MVH coordinate frames. Adapted from [31].

## 2.2 Orbital Mechanics

The two-body problem is a fundamental cornerstone of the study of astrodynamics, often serving as the starting point of more complex studies. In fact, practically any study of orbital motion will depend on Newton's laws, Kepler's laws, and on the universal law of gravitation [31].

### 2.2.1 The two-body problem

Let the masses of the Earth and a satellite be denoted by  $M_{\oplus}$  and  $m$ , respectively. For an inertial coordinate system, the universal law of gravitation (for the force of gravity of the Earth acting on the satellite) is given by

$$\mathbf{F}_g = -\frac{GM_{\oplus}m}{r^2} \left(\frac{\mathbf{r}}{r}\right), \quad (2.1)$$

where  $\mathbf{r}$  is the position vector of the satellite, measured from the center of mass of the primary body,  $r$  is the distance between the bodies, and  $G$  is the gravitational constant. Considering Newton's third law, the force the satellite exerts on Earth has the same magnitude and opposite direction to (2.1). Denoting  $\mathbf{r}_{\oplus}$  and  $\mathbf{r}_{\text{sat}}$  as the position vector of the Earth and the satellite, respectively, then  $\ddot{\mathbf{r}} = \ddot{\mathbf{r}}_{\text{sat}} - \ddot{\mathbf{r}}_{\oplus}$ , leading to

$$\ddot{\mathbf{r}} = \frac{\mathbf{F}_g}{m} - \frac{\mathbf{F}_g}{M_{\oplus}} = -\frac{G(M_{\oplus} + m)}{r^2} \left(\frac{\mathbf{r}}{r}\right) \quad (2.2)$$

or, considering that the mass of the satellite is much smaller than the mass of the primary body:

$$\ddot{\mathbf{r}} = -\frac{\mu_{\oplus}}{r^3} \mathbf{r}, \quad (2.3)$$

where  $\mu_{\oplus} = GM_{\oplus}$  is the gravitational parameter of the central body - Earth in this case. Equation (2.3) is the two-body equation. It is often called the relative form, because the motion is written in reference to the primary body [31]. To derive this equation, it was assumed that no forces act on the system, except for the gravitational forces of the two bodies, and the satellite and Earth were modelled

as spherically symmetrical, with uniform density, so as to treat each as a point mass. Additionally, the mass of the satellite was disregarded, as it will be orders of magnitude smaller than the Earth's mass, for the foreseeable future.

The two-body problem is a three degree of freedom dynamical system, and a particular orbit is completely specified by the initial position and velocity vectors ( $\mathbf{r}_0$  and  $\dot{\mathbf{r}}_0$ , given at some initial time  $t_0$ ). While this is true in a mathematical sense, these initial conditions do not convey helpful information to intuitively visualize the orbit. It is often advantageous to employ alternative representations that lend themselves to being directly visualized. Hence, the most common approach to representing an orbit is employing the six Keplerian elements (often simply denominated as orbital elements), which innately describe the shape and orientation of the orbit [30, 32].

## 2.2.2 Keplerian element representation

One of Newton's greatest achievements was showing that the motion under the influence of his law of gravitation was described by a conic section, implying that all closed orbits are elliptical and showing how the first Kepler law arises [29, 33]. With this knowledge, three parameters can be used to characterize the motion of the satellite within its orbital plane (irrespective of its relation to the reference frame). Two of these parameters characterize the shape of the conic section: the conic's semi-major axis ( $a$ ) and eccentricity ( $e$ ). The final parameter, true anomaly  $\nu$ , denotes the angle between the periapsis<sup>1</sup> and the orbiter, describing the current position of the body along the conic. Alternatively, the true anomaly  $\nu_0$  at a certain epoch  $t_0$  can be utilized, as the rate of change of the true anomaly can always be obtained (as a function of  $\nu$ , and the conic's semi-major axis and eccentricity) [30, 32]. Commonly, the epoch of passage at the periapsis ( $\nu_0 = 0$ ) is utilized.

It is often beneficial to consider other quantities, such as the mean anomaly  $M$ , which denotes the fraction of an (elliptical) orbit's period that has elapsed since the orbiting body passed the periapsis. Defining  $T = 2\pi\sqrt{a^3/\mu}$  as the orbital period, the mean motion  $n$  (i.e. average rate of sweep) can be written as  $n = 2\pi/T$ , and

$$M = n(t - \tau_p), \quad (2.4)$$

where  $\tau_p$  is the epoch of passage at the periapsis and  $t$  denotes the current epoch. As shown in Figure 2.3, three other quantities are required for the spatial orientation of the orbit. These are the right ascension of the ascending node  $\Omega$ , the orbital inclination  $i$ , and the argument of periapsis  $\omega$  [32]. The right ascension of the ascending node (also denominated as longitude of the ascending node, for geocentric orbits), is the angle in the equatorial plane, measured positive eastward, from the unit vector  $\hat{\mathbf{I}}$  (pointing to the first point of Aries) to the point where the satellite crosses the equator from south to north, denominated ascending node. The inclination is expressed as the angle between the reference frame and the orbital plane, and the argument of periapsis (or argument of perigee, for geocentric orbits) is the angle between the ascending node and the periapsis, measured along the orbital plane [31].

---

<sup>1</sup>Periapsis denotes the point (along a bodies orbit) where the orbiter is closest to the primary body.

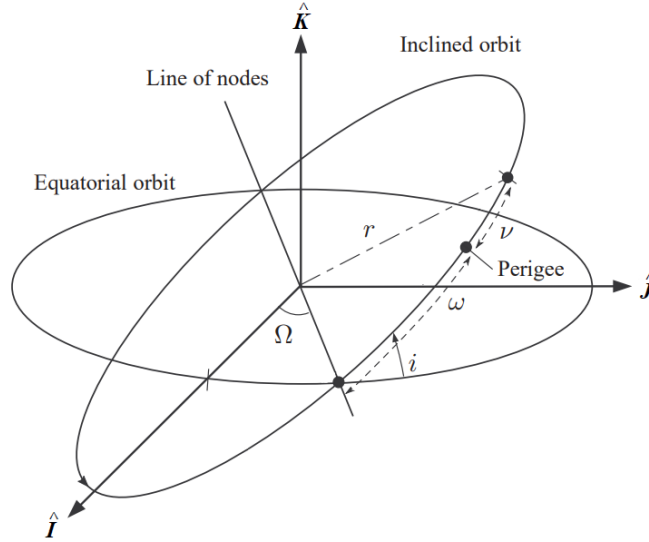


Figure 2.3: Classical orbital elements on a geocentric-equatorial frame. Adapted from [34].

## 2.3 Perturbations

In the universe, there are more than two bodies, and these bodies can have irregular shapes, leading to strongly nonspherical mass distributions. There will be a multitude of forces applied to the system described in the previous section, so real orbits can seldom be properly modelled taking into consideration the hypothesis of a two-body problem with spherical mass distributions. In order to accurately model the motion of a body, especially for long periods of time, other forces need to be taken into account. To do so, the effects of the main perturbations on the system must be properly modelled [35]. One way to account for these effects is to simply add the perturbing accelerations to the two-body equation, deriving a more accurate equation of motion. This method is denominated Cowell's formulation [31], and can be expressed as

$$\ddot{\mathbf{r}} = -\frac{\mu}{r^3} \mathbf{r} + \mathbf{a}_p, \quad (2.5)$$

where  $\mathbf{a}_p$  represents the accelerations caused by perturbations on the satellite. Setting  $\mathbf{a}_p$  to zero, the equation of motion is reduced to the ideal Keplerian situation, where the central body is a sphere with symmetrical mass distribution and all other disturbances are null (i.e. two-body problem) [27].

The main influence on a satellite orbiting Earth is the Earth's gravitational field, more explicitly the first term of its gravitational potential (representing the solution to the two-body problem). The second term of the potential, denominated  $J_2$  coefficient, also has a significant impact, as depicted in Figure 2.4. Thus, the gravitational field is often modelled at least up to this term. The relative importance of the remaining perturbations heavily depends on the altitude of the satellite's orbit. For satellites in low Earth orbits, atmospheric drag takes a fairly large importance, becoming the most important factor besides the Earth's gravitational field. Other perturbations, such as the influence from third-bodies (especially from the Moon and the Sun), solar radiation pressure, and tides have smaller effects [36].

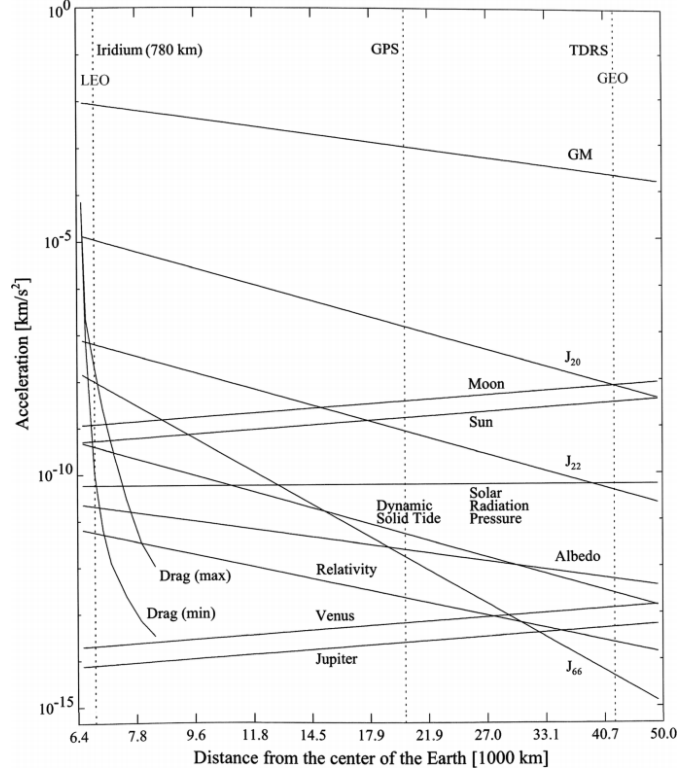


Figure 2.4: Magnitude of the main perturbations on a geocentric orbit. Retrieved from [36].

To numerically integrate Cowell's formulation, mathematical models for each perturbing force must first be derived [31]. The most impactful disturbing forces acting on the orbit of a satellite orbiting Earth, such as the perturbation caused by the nonspherical mass distribution of the primary body, the atmospheric drag, third-bodies, and the solar radiation pressure, are discussed in the following sections.

### 2.3.1 Earth's oblateness

To accurately describe the gravitational force of a primary body, a potential function that includes the perturbing accelerations due to the nonspherical mass distribution of that central body must be formed. Integrating the potential of a differential mass element over the (central) body results in

$$U(r) = G \int_{\beta} \frac{dm(\boldsymbol{\rho})}{\|\mathbf{r} - \boldsymbol{\rho}\|}, \quad (2.6)$$

where  $\boldsymbol{\rho}$  is the position vector of the differential mass element ( $dm$ ) and  $\beta$  is the collection of all mass elements. The gravitational potential (2.6) satisfies Laplace's equation outside the body ( $\nabla^2 U = 0$ ) and Poisson's equation inside the body ( $\nabla^2 U = -4\pi G\sigma_d$ ), where  $\sigma_d$  represents the local density [35]. For a sphere with uniform density, the integral of (2.6) yields (outside the body)

$$U = \frac{\mu}{r}, \quad (2.7)$$

which agrees with the previously presented solution for the two-body problem.

There are several methods to specify the gravitational potential of a nonspherical body. In fact, any

solution which corresponds to the physical mass distribution of the body and that satisfies Laplace's equations will generally work [35]. The potential function  $U$  can be developed (see [31, 35]) to show that the general form for the spherical harmonic potential for a gravity field at a point outside the body is

$$U = \frac{\mu}{r} \sum_{w=0}^{\infty} \sum_{q=0}^w \left(\frac{R}{r}\right)^w P_{w,q}(\sin \varphi) (C_{w,q} \cos q\lambda + S_{w,q} \sin q\lambda), \quad (2.8)$$

where the summation introduces the  $w$  and  $q$  indices as degree and order, respectively,  $R$  is a normalizing radius (chosen as the equatorial radius of the body<sup>2</sup>),  $P_{w,q}$  are associated Legendre functions,  $C_{w,q}$  and  $S_{w,q}$  are the gravity field harmonic coefficients, which characterize the mass distribution of the body, and  $\varphi$  and  $\lambda$  are the latitude and the longitude of the point, respectively [35]. Another very common form of this relation, which separates the terms with  $q = 0$  from the terms with  $q \neq 0$ , is given by

$$U = \frac{\mu}{r} \left( 1 - \sum_{w=2}^{\infty} J_w \left(\frac{R}{r}\right)^w P_{w,0}(\sin \varphi) + \sum_{w=2}^{\infty} \sum_{q=1}^w \left(\frac{R}{r}\right)^w P_{w,q}(\sin \varphi) (C_{w,q} \cos q\lambda + S_{w,q} \sin q\lambda) \right), \quad (2.9)$$

where  $J_w = -C_{w,0}$  [31]. Note that the sign in the definition of  $J_w$  is merely a matter of convention, chosen to make  $J_2$  positive [37]. The first term of (2.9) coincides with (2.7), representing the gravitational potential of a spherical body with radially symmetric mass density distribution. The following terms specify the influence of the deviations of the body's shape and mass density distribution from a uniform sphere. Particularly, the second term (zonal harmonics,  $q = 0$ ) models the deviations in the north-south direction and the third term (tesseral and sectorial harmonics) represents the deviations in the north-south and east-west directions. For the tesseral harmonics  $q \neq w$  holds, whereas for the sectorial harmonics  $q = w$  [37]. The spatial structure of the spherical harmonics is presented in Figure 2.5, where the shading represents regions of additional mass.

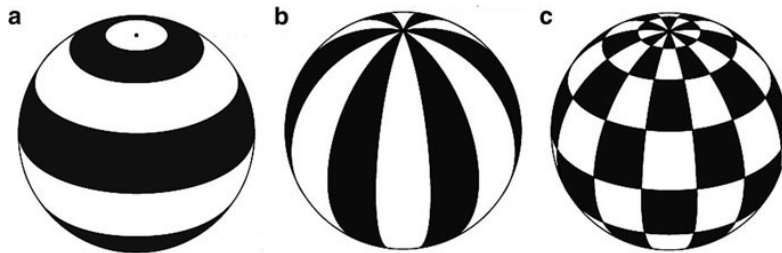


Figure 2.5: Spatial structure of spherical harmonics. (a) zonal harmonic  $P_6$ , (b) sectorial harmonic  $P_{6,6}$ , (c) tesseral harmonic  $P_{12,6}$ . Retrieved from [38].

Modern models for the Earth's gravitational field often contain coefficients up to large order and degree (2150 or higher). However, for bodies whose shape and mass distribution is roughly spherical (such as planets) it is often viable to employ simpler versions of these models, as the first terms of the gravitational potential will accurately model the gravitational field [37]. Consider Table 2.1, which contains some coefficients  $J_w$  from the GRACE GGM02C Earth gravity field model. It can be noted that  $J_2$  is, by far, the strongest perturbation due to the Earth's shape, over 400 times larger than the next largest coefficient ( $J_3$ ). The  $J_2$  coefficient accounts for most of the Earth's gravitational departure from

<sup>2</sup>It can alternatively be defined as the mean radius of the body [37].

a perfect sphere, and primarily characterizes the Earth's equatorial bulge [31]. Therefore, the motion of a satellite orbiting Earth can often be properly modelled as an ideal two-body problem, perturbed by the effect of the second term of the expansion,  $J_2$  [39].

Table 2.1: Some coefficients of the GRACE GGM02C Earth gravity field model. Adapted from [37].

| $w$ | $J_w (10^{-6})$ |
|-----|-----------------|
| 2   | 1082.6357       |
| 3   | -2.5324737      |
| 4   | -1.6199743      |
| 5   | -0.2279051      |

### 2.3.2 Atmospheric drag

A spacecraft orbiting Earth suffers an acceleration due to the atmospheric drag. By definition, this acceleration has opposite direction to the velocity of the vehicle relative to the rotating atmosphere [29]. The acceleration caused by the atmospheric drag is usually modelled by

$$\mathbf{a}_D = -\frac{1}{2} \frac{C_d A}{m} \rho v_{\text{rel}}^2 \left( \frac{\mathbf{v}_{\text{rel}}}{\|\mathbf{v}_{\text{rel}}\|} \right), \quad (2.10)$$

where  $\rho$  is the atmospheric density,  $\mathbf{v}_{\text{rel}}$  is the orbital velocity in relation to the rotating atmosphere (with magnitude  $v_{\text{rel}}$ ),  $C_d$  is the drag coefficient of the spacecraft,  $A$  is its cross-sectional area and  $m$  its mass, as previously defined [31]. The velocity vector considered in (2.10) is not the velocity vector  $\dot{\mathbf{r}}$ , typically found in the state vector, as the velocity is taken in relation to the atmosphere which has a mean motion due to the Earth's rotation. This velocity can be obtained as

$$\mathbf{v}_{\text{rel}} = \frac{d\mathbf{r}}{dt} - \boldsymbol{\omega}_{\oplus} \times \mathbf{r}, \quad (2.11)$$

where  $\boldsymbol{\omega}_{\oplus}$  indicates the angular velocity vector of the Earth's rotation, with magnitude  $\omega_{\oplus}$  [31]. The drag coefficient depends on the spacecraft configuration, as it essentially reflects the spacecraft's susceptibility to drag forces [31]. However, a value of approximately 2.2 is widely used [40]. The atmospheric density indicates how dense the atmosphere in the vicinity of the satellite is, and is often the most difficult parameter to determine. The cross-sectional area is defined as the area of the spacecraft normal to the satellite's velocity vector [31]. Usually, these three quantities are grouped and presented as the ballistic coefficient

$$B^* = \frac{C_d A}{m}, \quad (2.12)$$

which is an important measure of a satellite's susceptibility to the effects of the atmospheric drag<sup>3</sup>. Atmospheric drag has important effects on the semi-major axis of the orbit, reducing it by hundreds of meters to several kilometers per year, depending on the height of the orbit and the ballistic coefficient of the spacecraft [41]. While the ballistic coefficient of the spacecraft is an important property, the decisive factor for the magnitude of the acceleration caused by the atmospheric drag is the height of the orbit,

<sup>3</sup>Many organizations use the reciprocal:  $B_2^* = m/(C_d A)$ .

since the atmospheric density decreases (approximately) exponentially with height.

### Determining the atmospheric density

Atmospheric density has a remarkable variability over time, making atmospheric drag estimation very difficult [18]. In fact, the atmosphere is substantially impacted by factors such as the solar heat input and, as such, the atmospheric density at a specific location may vary considerably over time. A diurnal variation of the atmospheric density can be noted, due to the Earth's rotation relative to the direction of the Sun. The Sun's rotation about its axis will also cause a 27-day variation of the solar input, and thus, of the atmospheric density. Furthermore, many other semiregular and irregular variations have noticeable effects. As a result, the atmospheric conditions are not only a function of the altitude, but also dependent on the time of the day and the solar activity [37].

In order to develop a simple model of the atmosphere, assume a spherically symmetrical distribution of particles and an exponentially decreasing atmospheric density. Based on these assumptions, the atmospheric density (as a function of the satellite's altitude) can be written as

$$\rho = \rho_0 e^{-\frac{h}{H_0}}, \quad (2.13)$$

where  $\rho_0$  is a reference density,  $h$  is the satellite altitude, and  $H_0$  is the scale height

$$H_0 = \frac{R_g T_k}{M_p g}, \quad (2.14)$$

which depends on the gas constant  $R_g$ , the mean atmospheric temperature  $T_k$ , the mean mass of a mol of particles  $M_p$ , and the gravitational acceleration at the location. To accurately represent the real atmosphere, the appropriate scale height  $H_0$  (and reference density  $\rho_0$ ) will vary with factors such as height and solar activity. Hence, atmospheric models often propose a different scale height and reference density for different intervals of altitude (i.e. layers).

In order to increase the reliability of the estimation of the atmospheric drag, numerous phenomena (such as solar activity) must be captured. To this end, various atmospheric models have been developed over the past decades [31]. The U.S. Standard Atmosphere (1976), for instance, aims to provide a standard reference model for moderate solar activity. The model consists of tabulated data of the atmospheric parameters (such as density, pressure, temperature, and scale height) at a latitude of 45° N. Starting in the late 1970s, the MSIS-class models (Mass Spectrometer Incoherent Scatter radar) were developed by NASA. This class of atmospheric models is based on space-based mass spectrometry and ground-based incoherent scatter radar readings. The consistent development of the MSIS-class models resulted in an upgraded model, NRLMSISE-00, published in 2002. Besides the data employed in the MSIS-class models, the novel NRLMSISE-00 atmospheric model employs satellite accelerometer data and orbit decay databases [37].

### 2.3.3 Third-body perturbations

While the dominant force affecting the orbital motion of a satellite is usually the gravitational field of the mother planet, significant perturbations arise from other sources, such as nearby planets, stars, or other large orbiters. The acceleration due to the gravitational attraction that a perturbing body applies to a satellite can be written as

$$\mathbf{a}_{sp} = -\frac{\mu_p}{\|\mathbf{r}_{sp}\|^3}\mathbf{r}_{sp}, \quad (2.15)$$

where  $\mu_p$  is the gravitational parameter of the perturbing body and  $\mathbf{r}_{sp}$  is the vector from the satellite to the perturbing body [35]. However, note that the motion of the satellite must be obtained in relation to Earth, so the relative acceleration is needed (i.e. the difference between the acceleration that the third-body induces on the orbiter and on Earth). Therefore, assuming that the mass of the satellite is negligible in relation to the masses of the Earth and the perturbing body, the acceleration due to a third-body perturbation is given by

$$\mathbf{a}_{TB} = -\mu_p \left( \frac{\mathbf{r}_{sp}}{\|\mathbf{r}_{sp}\|^3} - \frac{\mathbf{r}_{\oplus p}}{\|\mathbf{r}_{\oplus p}\|^3} \right), \quad (2.16)$$

where  $\mathbf{r}_{\oplus p}$  is a vector from the Earth to the perturbing body. In case multiple bodies are attracting the spacecraft with significant importance, a different perturbing acceleration may be written for each one. These perturbations may then be summed in order to obtain the total perturbing acceleration by third-bodies. The distance between the spacecraft and the perturbing bodies may either be obtained from ephemerides or theory (i.e. two-body problem) [35].

### 2.3.4 Solar radiation pressure

Similarly to the atmospheric drag, the effect of the solar radiation pressure varies substantially with height. However, contrary to the atmospheric drag, the effect of the solar radiation has a larger influence at higher altitudes. Determining the effect of the solar radiation is often a complex task, as it involves predicting variations in the solar flux, and modelling the effect of the Earth's shadowing on the spacecraft [31]. Depending on the solar activity, the solar radiation pressure may be either relatively significant (e.g. due to phenomena such as solar storms) or it may be negligible [31].

The solar radiation pressure is given by the force that the incoming radiation exerts on the satellite divided by the incident area exposed to the Sun. Hence, to compute the solar radiation pressure, the solar flux must first be determined. While the solar flux varies over time, many programs employ an approximated constant value because the actual value is often very difficult to determine. The most commonly employed value is the so called solar-radiation constant ( $S_f = 1367 \text{ W/m}^2$ ). The perturbing acceleration on the satellite due to the solar radiation pressure can be modelled by

$$\mathbf{a}_{SRP} = -\frac{p_{SRP} c_r A_{\odot}}{m} \frac{\mathbf{r}_{s\odot}}{\|\mathbf{r}_{s\odot}\|}, \quad (2.17)$$

where  $c_r$  is the reflectivity of the spacecraft (a value between 0 and 2 which represents how the satellite

reflects incoming radiation),  $p_{\text{SRP}}$  is the solar radiation pressure,  $A_{\odot}$  is the exposed area to the Sun, and  $\mathbf{r}_{s\odot}$  is the vector from the spacecraft to the Sun [31]. Studying Figure 2.4, it can be noted that this perturbation is rather unimportant for very low Earth orbits, in comparison to other perturbations. However, it may be significant for low Earth orbits close to the upper limit of 2000 km of altitude.

### 2.3.5 Other perturbations

There exist a multitude of other forces which affect a satellite's orbit. However, these are often negligible, particularly for low Earth orbits, as the atmospheric drag and the  $J_2$  coefficient overbear the smaller effects of these perturbations. Some solar radiation that reflects off the Earth back onto a satellite (albedo) can affect its orbit. Solid-Earth tides, which are displacements of the Earth's surface due to third-body perturbations (particularly the Moon), also impact the motion of the satellite. Ocean tides, the effect of the Earth's magnetic field, and relativistic effects are some other sources of perturbations on the satellite's motion [31, 37].

### 2.3.6 Perturbed motion

As previously noted, it is often enriching to utilize the Keplerian elements to represent an orbit, as these make it easy to visualize. An additional advantage of representing the orbit with Keplerian elements is that most of the elements undergo small variations in perturbed motion, whereas the position and velocity vectors change rapidly over time. Orbital elements can be distinguished as either fast or slow variables, depending on their relative rate of change. Fast variables change substantially during one orbital revolution, even in the absence of perturbations. Examples are the true and mean anomalies, which change  $360^\circ$  over an orbit. On the other hand, slow variables (semi-major axis, eccentricity, inclination, longitude of the ascending node, and argument of perigee) hardly change throughout one orbital revolution. These small changes are caused by perturbations, and without them all the slow elements would remain constant [31].

#### Osculating and mean orbital elements

To each set of position and velocity vectors along the perturbed orbit corresponds a set of osculating orbital elements, from the Latin *osculare*, "to kiss" [33]. This term implies the contact between the osculating orbit and the true (perturbed) orbit. The osculating orbit, described by the osculating orbital elements at a certain epoch, is the orbit which would result if all perturbing forces were removed at that instant, leading to each point on the perturbed trajectory having a (unique) corresponding set of osculating elements [29, 31]. The osculating elements capture the periodic variations of the satellite's orbit, and thus vary quite erratically. At the time the osculating orbital elements are obtained, the true and osculating orbits are in contact. However, these soon diverge, as the true orbit continues to be perturbed. Figure 2.6 displays the true orbit and two (differing) osculating orbits obtained at two different epochs<sup>4</sup>.

---

<sup>4</sup>The process called "rectification", mentioned in Figure 2.6, simply means that a new epoch and starting point coincident with the true orbital path are considered, and a new osculating orbit is calculated (see Encke's method [29]).

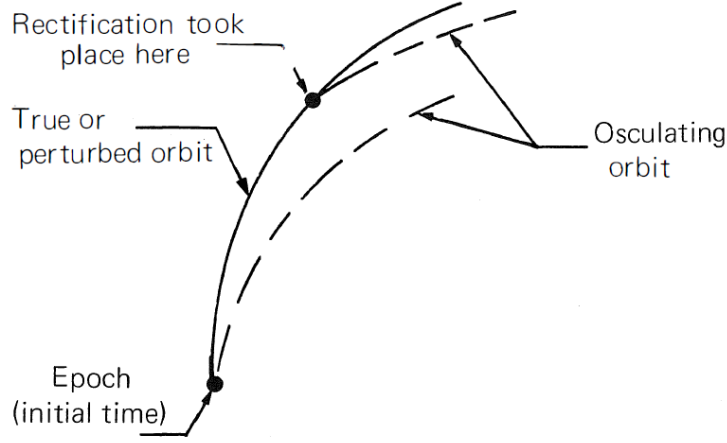


Figure 2.6: Osculating and true orbits. Adapted from [29].

Contrary to the osculating orbital elements, the mean orbital elements are averaged over some selected time. These elements define an approximate orbit considering only fast motions (e.g. true anomaly) and discarding the slower motions caused by perturbations on the orbit, not representing the true values of position and velocity, but varying less erratically over time than their osculating counterpart [42]. These elements are useful for mission planning because they approximate the satellite's long-term behavior, not including short-periodic variations [31].

### Gauss' variational equations for near-circular non-equatorial orbits

The equations of motion of a controlled spacecraft, in terms of the osculating orbital elements, are given by Gauss' form of Lagrange's planetary equations [30, 35]

$$\frac{da}{dt} = \frac{2a^2}{h_m} \left( e \sin v a_R + \frac{\ell}{r} a_T \right), \quad (2.18a)$$

$$\frac{de}{dt} = \frac{1}{h_m} (\ell \sin v a_R + [(\ell + r) \cos v + re] a_T), \quad (2.18b)$$

$$\frac{di}{dt} = \frac{r \cos u}{h_m} a_N, \quad (2.18c)$$

$$\frac{d\Omega}{dt} = \frac{r \sin u}{h_m \sin i} a_N, \quad (2.18d)$$

$$\frac{d\omega}{dt} = \frac{1}{h_m e} (-\ell \cos v a_R + (\ell + r) \sin v a_T) - \frac{r \sin u \cos i}{h_m \sin i} a_N, \quad \text{and} \quad (2.18e)$$

$$\frac{dM}{dt} = n + \frac{b}{ah_m e} ((\ell \cos v - 2re) a_R - (\ell + r) \sin v a_T), \quad (2.18f)$$

where  $a_R$ ,  $a_T$  and  $a_N$  are the radial, along-track (perpendicular to orbit radial direction), and cross-track acceleration components (caused by perturbations), respectively,  $u = \omega + v$  is the argument of latitude, and  $b$ ,  $h_m$ , and  $\ell$  are the semi-minor axis, the angular momentum (per unit of mass), and the semi-latus rectum, respectively. Studying (2.18), it can be noted that, if no perturbations acted on the satellite, all the orbital elements would be constant, besides the mean anomaly, which would vary over time

respecting  $dM/dt = n$  (two-body problem).

Valuable low Earth orbits are often near-circular ( $e \approx 0$ ) [16, 22, 23]. For near-circular orbits, the semi-minor and semi-major axis of the orbit have approximately the same length, and the distance between the spacecraft and the Earth remains approximately constant. As a result, the approximations

$$\begin{cases} e = 0, \\ r = a = b, \text{ and} \\ h_m = \sqrt{\mu a} \end{cases} \quad (2.19)$$

can be applied, and Gauss' form of Lagrange's planetary equations for near-circular orbits can be written as

$$\frac{da}{dt} = \frac{2a^2}{\sqrt{\mu a}} a_T = \frac{2a}{v} a_T, \quad (2.20a)$$

$$\frac{de}{dt} = \frac{1}{\sqrt{\mu a}} (a \sin v a_R + 2a \cos v a_T) = \frac{\sin v}{v} a_R + \frac{2 \cos v}{v} a_T, \quad (2.20b)$$

$$\frac{di}{dt} = \frac{a}{\sqrt{\mu a}} \cos u a_N = \frac{\cos u}{v} a_N, \text{ and} \quad (2.20c)$$

$$\frac{d\Omega}{dt} = \frac{\sin u}{v \sin i} a_N, \quad (2.20d)$$

where  $v$  is the orbital velocity. Notice how the classical orbital element representation leads to singular equations for (2.18e) and (2.18f) when the eccentricity is zero. This requires an alternative parametrization of the problem to be chosen. Consider the parametrization  $\mathbf{k}_{\text{osc}}$ , in terms of osculating orbital elements,

$$\mathbf{k}_{\text{osc}} = \begin{bmatrix} a \\ e_x \\ e_y \\ i \\ \Omega \\ u \end{bmatrix} = \begin{bmatrix} a \\ e \cos \omega \\ e \sin \omega \\ i \\ \Omega \\ \omega + M \end{bmatrix} \quad (2.21)$$

as, for near-circular orbits  $v - M = 2e \sin M$ , such that  $v \approx M$  and  $u \approx \omega + M$ . With this parametrization, Gauss' variational equations of motion adapted for near-circular non-equatorial orbits can be written, utilizing an RTN orbital frame, as

$$\frac{d}{dt} \begin{bmatrix} a \\ e_x \\ e_y \\ i \\ \Omega \\ u \end{bmatrix} = \frac{1}{v} \begin{bmatrix} 0 & 2a & 0 \\ \sin u & 2 \cos u & 0 \\ -\cos u & 2 \sin u & 0 \\ 0 & 0 & \cos u \\ 0 & 0 & \sin u / \sin i \\ -2 & 0 & -\sin u / \tan i \end{bmatrix} \begin{bmatrix} a_R \\ a_T \\ a_N \end{bmatrix} + \begin{bmatrix} 0 \\ 0 \\ 0 \\ 0 \\ 0 \\ n \end{bmatrix}. \quad (2.22)$$

While this parametrization avoids singular equations for near circular orbits, it will still lead to singular

equations for equatorial orbits ( $i = 0^\circ$ ), but this will not be the case studied [16]. If the orbit to be studied were equatorial, then a different set of orbital elements, denominated equinoctial orbital elements, could be employed. These would result in nonsingular equations, except for  $h_m = 0$  (rectilinear orbits), and for orbits with inclination  $i = \pi$  rad (retrograde equatorial orbits) [30].

### Effect of perturbations on the orbital elements

Perturbations affecting the orbital motion result in secular and periodic changes for the orbital elements. Figure 2.7 shows an example of each of these effects. Secular changes cause a particular element to grow over time. The orbital element may grow linearly over time or, in some cases, proportionally to some power of time. These secular changes result in unbounded error growth and, as a result, are the main cause of the deterioration of the accuracy of analytical satellite theories over long time intervals. Periodic changes can be classified as either short-periodic or long-periodic, depending on the length of time required for an effect to repeat. Typically, changes with a period similar to, or smaller than, the satellite's orbital period are considered short-periodic changes, whereas changes with cycles considerably longer (usually one or two orders of magnitude larger) than the orbital period are considered long-periodic changes. These long-periodic effects can last for over a month and are seen, for example, in the motion of the ascending node and the argument of perigee [31].

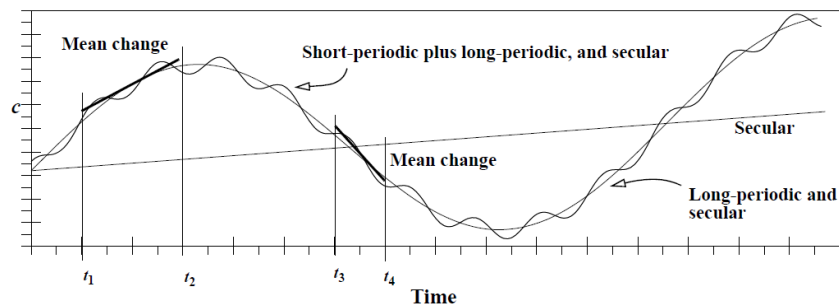


Figure 2.7: Effects of perturbations on an orbital element. Retrieved from [31].

Mean orbital elements are usually at the basis of the calculations of the ephemerides of artificial satellites [43]. Moreover, mean orbital elements are usually the ones employed in feedback laws for orbit control. However, in practice, the osculating elements of the orbit are the ones that are available. As a result, algorithms for the conversion between osculating and mean orbital elements are crucial [44]. A frequently utilized theory on the motion of artificial Earth satellites is Brouwer's analytical satellite theory [45]. For Brouwer's analytical satellite theory, the set of mean elements is understood as osculating orbital elements from which the short-periodic (functions of the mean anomaly) and long-periodic (multiples of the argument of perigee) perturbations of the Earth's gravitational field have been removed. An algorithm to convert osculating elements to mean elements, as understood by Brouwer, generally relies on a process that iterates the osculating orbital elements under the restraints of Brouwer's satellite theory. Applying this class of algorithms, a set of mean orbital elements can be obtained for each set of osculating orbital elements, at a certain epoch. The mean orbital elements do not include the short and long-period perturbations due to the Earth's gravitational field, and thus describe the long-

term behavior of the satellite [44]. This topic has been thoroughly discussed in the literature. Older publications such as [44] and [46] propose iterative procedures for the determination of the mean elements for Brouwer’s analytical theory. Alternatively, conversion algorithms based on Eckstein-Ustinov’s analytical satellite theory, first developed by Ustinov and later corrected by Eckstein [47, 48], can be employed. Eckstein-Ustinov’s satellite theory presents a large advantage for near-circular orbits, as it employs the nonsingular orbital elements of (2.21), which avoid singular Lagrange planetary equations when  $e = 0$  [49]. Since this thesis will study near-circular orbits, the conversion between osculating and mean orbital elements will be conducted by an algorithm based on Eckstein-Ustinov’s analytical satellite theory. Particularly, the conversion is performed by an algorithm included in the *osculating2mean* package, available at [50].

## 2.4 Sensors and actuators

### 2.4.1 Sensors

Global navigation systems (e.g. GPS, GLONASS, Galileo, and BeiDou) intend to provide positioning services for users on the ground. However, their signals spill into space and can likewise be received by other satellites. Satellites in low Earth orbit particularly benefit from these navigation systems, experiencing similar signal strength to users on the ground, without any natural or man-made obstacles to block the signal. Alternatively to (or supplementing) the readings of the GNSS, ground stations can be employed to determine the orbit of the satellite, with radar observations providing the radial distance and Doppler observations providing the radial velocity. Utilizing a combination of these sensors, and possibly using measurements from various ground stations, six independent quantities are determined in order to infer the satellite’s position and velocity vectors [51]. The obtained data is filtered and, depending on the observations, an appropriate preliminary orbit determination algorithm can be applied. Classical preliminary orbit determination algorithms include the Gibbs’ method, which predicts the orbit from three geocentric position vectors, and the Lambert’s problem, deducing the orbit from two position vectors and the time between them. The results from these preliminary analyses are then adjusted considering perturbations, as the algorithms mentioned are based on the two-body equation of motion [52]. An alternative to applying orbit determination algorithms, which require multiple measurements, is to utilize the GNSS estimated position and velocity vectors at a single epoch. These vectors can be converted to osculating orbital elements (see, for instance, Algorithm 9 of [31]), and then converted to mean orbital elements (e.g. utilizing Eckstein-Ustinov’s theory [48]). The sole utilization of GNSS provides many advantages in relation to traditional ground-based tracking systems. It offers continuous coverage (since it is not limited by contacts with a ground station), low system cost, and increased spacecraft autonomy, as no orbit determination process is required [53].

The spacecraft absolute position measured by a GNSS receiver  $\hat{\mathbf{r}}$ , can be modeled as the true absolute position  $\mathbf{r}$ , plus sensor noise  $\mathbf{w}_r$  (i.e.  $\hat{\mathbf{r}} = \mathbf{r} + \mathbf{w}_r$ ) [17]. The necessary on-board position and velocity knowledge depends on the mission of the satellite. For instance, Earth observation missions

require precise alignment of their instruments (e.g. cameras and altimeters). These requirements lead to necessary position and velocity knowledge with accuracies of about 10 m and 1-10 cm/s, respectively. Altimeter missions, to determine the mean sea level, require strict position requirements of about 1-2 cm in the radial direction. Satellite missions to monitor the troposphere measure the delay of a signal traversing Earth's atmosphere, and thus require precise knowledge of the satellite's velocity, usually with an uncertainty of less than 0.05-0.2 mm/s. These different missions not only require GNSS receivers with varying accuracies, but also lead to different orbit control requirements [53]. Besides the required position and velocity accuracy for the mission, the weight and the power requirement of the GNSS receiver are important factors for the choice of a suitable navigation system for the spacecraft. Table 2.2 summarizes these key parameters for a variety of GNSS receivers employed in various space missions.

Table 2.2: GNSS receivers for space applications. Adapted from [53].

| Mission    | Objective            | Receiver     | Type          | Power (W) | Mass (kg) |
|------------|----------------------|--------------|---------------|-----------|-----------|
| Sentinel-6 | Radar altimeter      | PODRIX GNSS  | GPS + Galileo | 15        | 3         |
| GOCE       | Map Earth's gravity  | Lagrange     | GPS           | 30        | 5.2       |
| SARah      | Radar Reconnaissance | LION         | GPS + GAL     | 15        | 3         |
| DEMETER    | Detect EM Emissions  | TopStar 3000 | GPS           | 1.5       | 1.5       |
| PRISMA     | Earth observation    | Phoenix      | GPS           | 0.9       | 0.1       |

## 2.4.2 Actuators

The actuators employed are often a set of thrusters, allowing for orbit corrections to be applied in multiple directions. However, the type of propulsion that is considered will depend on the goals of the mission [17].

### The rocket equation

In order to derive the equation of motion of a rocket, consider the ejection of a small mass of fuel during a short interval of time ( $dt$ ). Assume that there are no external forces on the rocket and that the exhaust gas is expanded at zero pressure. In these conditions, to conserve linear momentum, the equation of motion must read as

$$m \frac{d\mathbf{v}}{dt} = \mathbf{v}_e \frac{dm}{dt}, \quad (2.23)$$

where  $\mathbf{v}$  is the velocity vector of the spacecraft and  $\mathbf{v}_e$  is the exhaust velocity vector (velocity of the expelled mass of fuel in relation to the spacecraft) [32]. The quantity described by (2.23) is called thrust and has opposite direction to the expelled material, since  $dm/dt$  is negative. It is common to employ the specific impulse  $I_{sp}$  instead of the exhaust velocity. The specific impulse is usually defined as the amount of momentum gained per weight (instead of mass) of fuel consumed [32]. This parameter can be understood as a measure of how efficiently a reaction mass engine creates thrust and is given by

$$I_{sp} = \frac{v_e}{g_0}, \quad (2.24)$$

where  $v_e$  is the magnitude of the exhaust velocity and  $g_0$  is the standard mean acceleration of gravity on Earth, not the local acceleration of gravity. Note that this had to be the case, otherwise (2.24) would (wrongly) convey that the exhaust velocity of an engine becomes smaller near a planet with lower gravity, and zero when the vehicle is in free fall. While any propulsion system that produces thrust by ejecting mass obeys the rocket equation, different propulsion technologies have unique strengths and weaknesses as well as differing performances [32]. Table 2.3 lists some current propulsion technologies, with their exhaust velocities and specific impulses.

Table 2.3: Efficiency of various propulsion technologies. Adapted from [32].

| $v_e$ (km/s) | $I_{sp}$ (s) | Technology                        |
|--------------|--------------|-----------------------------------|
| 1.6 – 2.1    | 170 – 220    | Solid fuel                        |
| 1.9 – 3.4    | 200 – 350    | Hydrocarbon liquid fuel           |
| 4.4          | 455          | Liquid hydrogen and liquid oxygen |
| 3 – 7        | 300 – 700    | Plasma jet, Arcjet                |
| $10^2 \leq$  | $10^4 \leq$  | Ion, Magnetohydrodynamic          |

It can be noted that chemical rocket engines have the lowest performance out of the rocket technologies listed in Table 2.3. The efficiency of a chemical rocket engine is tied with the energy liberated by the chemical reactions  $E_{ch}$ , which can be written as

$$E_{ch} = \frac{1}{2}m_r v_e^2 \approx \frac{5}{2}k_B T_c, \quad (2.25)$$

where  $m_r$  is the mass of one molecule of the reaction product,  $T_c$  is the combustion temperature, and  $k_B$  is the Boltzmann's constant. It is possible to note that, to achieve good performance (i.e. large exhaust velocity), the mass of the exhaust product must be small. An efficient chemical rocket engine is employed in the space shuttle's main engine. This chemical rocket utilizes liquid hydrogen and liquid oxygen, achieving an  $I_{sp}$  of 455 s (out of a theoretical maximum of 457 s) [32].

In order to develop propulsion systems with better performances, it is necessary to break the first equality of (2.25). That is, the energy source must not be a chemical reaction. The energy may instead be provided by thermal processes, expelling a low mass working fluid such as liquid hydrogen or hydrazine. The plasma jet and arcjet technologies fall into this category. Still, these technologies also have an inherent limit to their performance. Note that by working the second equality of (2.25), it is possible to write

$$T_c \approx \frac{m_r v_e^2}{5k_B}. \quad (2.26)$$

Therefore, according to Table 2.3, an engine with the same exhaust velocity and fuel as the space shuttle's main engine would already be operating at a temperature of 6000 K. Since the exhaust temperature increases with the square of the exhaust velocity, any further (sizeable) progress should not be expected from a technology using a thermal process [32].

To progress further, it is necessary to break the equality of (2.26). That is, the mass must be ejected by a nonthermal process. The ion engines, which electrostatically accelerate ionized gas, and the magnetohydrodynamic (MHD) engines, in which an ionized gas is electromagnetically accelerated, fall

into this category. Ion thrusters can reach a very high specific impulse. However, when operated at high exhaust velocities, these engines require large quantities of electrical power. Since the power supply on-board a spacecraft is heavily limited, it is often beneficial to feed ion engines more fuel instead of more electricity. This would increase the available thrust, but it would also reduce the specific impulse of the engines [32].

Figure 2.8 follows a traditional approach of displaying the performance of propulsion systems for satellite orbit control, showing the range of thrust and specific impulse provided by various propulsion technologies. Two main categories of propulsion systems can be noted: 1) the chemical and thermal propulsion systems and 2) the electromagnetic and electrostatic propulsion systems. These categories are differentiated by the specific impulse and thrust range provided by the respective technologies [54]. The chemical and thermal propulsion systems are usually less efficient than the electromagnetic and electrostatic propulsion systems, as previously noted. However, the former deliver larger amounts of thrust, from 1 mN to 10 N. On the other hand, electromagnetic and electrostatic propulsion system are very efficient, providing a specific impulse up to 6000 s. Yet, these technologies provide a limited amount of thrust, from 10  $\mu$ N to 10 mN. As a result, the two defined categories of propulsion systems are useful for different missions. Chemical and thermal propulsion systems are recommended for missions that require fast maneuvers to be performed. On the other hand, electromagnetic and electrostatic propulsion systems are beneficial for mission profiles that need some maneuverability but do not require fast maneuvers [54]. Employing a low-thrust continuous control scheme allows the application of an electromagnetic or electrostatic propulsion system, providing higher efficiency at the cost of a low maximum actuation. On the other hand, orbit control methods relying on large impulsive maneuvers will likely require chemical or electrothermal propulsion systems.

Studying the specific impulse of the available propulsion systems can prove useful for an initial comparison. However, it is important to note that other system aspects, such as the hardware mass, the electric power supply, and the thermal shielding, must also be taken into consideration [54].

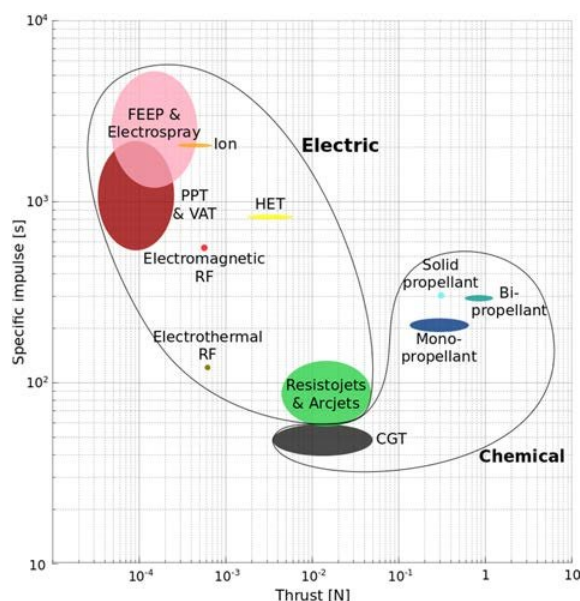


Figure 2.8: Thrust and specific impulse provided by some propulsion technologies. Retrieved from [54].

## 2.5 Control methodology

The control methodology that is at the root of this thesis is the LQR, applied to a linear time-invariant discrete system. Consider that the plant to be controlled is given by a linear time-invariant discrete system

$$\mathbf{x}_{k+1} = \mathbf{A}\mathbf{x}_k + \mathbf{B}\mathbf{u}_k, \quad (2.27)$$

where  $\mathbf{x}_k$  is the state of the system,  $\mathbf{u}_k$  is the control input,  $\mathbf{A}$  is the state matrix, and  $\mathbf{B}$  is the input matrix. The goal is to determine an optimal control policy  $\mathbf{u}_k$  which minimizes a certain performance measure  $J$ . For an infinite control window, the performance measure  $J$  can be written as the quadratic function

$$J = \frac{1}{2} \lim_{N \rightarrow \infty} \left[ \mathbf{x}_N^T \mathbf{S}_N \mathbf{x}_N + \sum_{k=0}^{N-1} (\mathbf{x}_k^T \mathbf{Q} \mathbf{x}_k + \mathbf{u}_k^T \mathbf{R} \mathbf{u}_k) \right], \quad (2.28)$$

where  $\mathbf{Q}$  and  $\mathbf{S}_N$  are symmetric positive semi-definite matrices ( $\mathbf{Q} = \mathbf{Q}^T \succeq 0$ ,  $\mathbf{S} = \mathbf{S}^T \succeq 0$ ) and  $\mathbf{R}$  is a symmetric positive definite matrix ( $\mathbf{R} = \mathbf{R}^T \succ 0$ ) [55]. In (2.28), the penalty on the state error is given by the term  $\mathbf{x}_k^T \mathbf{Q} \mathbf{x}_k$ , whereas the second term represents the necessary *cost* associated with the magnitude of the control. The weighting matrices  $\mathbf{Q}$  and  $\mathbf{R}$  are tuned to specify the relative importance of the error in each of the components of the state and of the actuation [16]. Let  $\mathbf{Q} = \mathbf{C}^T \mathbf{C}$ . Under the assumption of stabilizability of the pair  $(\mathbf{A}, \mathbf{B})$  and detectability of  $(\mathbf{A}, \mathbf{C})$ , the LQR design for this problem is associated with the discrete-time algebraic Riccati equation [55, 56]. Moreover, the optimal feedback law is given as

$$\mathbf{u}_k = -(\mathbf{R} + \mathbf{B}^T \mathbf{P} \mathbf{B})^{-1} \mathbf{B}^T \mathbf{P} \mathbf{A} \mathbf{x}_k, \quad (2.29)$$

where the steady-state solution  $\mathbf{P}$  can be found by backwards iteration of the dynamic Riccati equation (with terminal condition  $\mathbf{P}_N = \mathbf{S}_N$ ) until it converges and is, in fact, the unique positive definite solution of the discrete-time algebraic Riccati equation [55]

$$\mathbf{A}^T \mathbf{P} \mathbf{A} - \mathbf{A}^T \mathbf{P} \mathbf{B} (\mathbf{R} + \mathbf{B}^T \mathbf{P} \mathbf{B})^{-1} \mathbf{B}^T \mathbf{P} \mathbf{A} + \mathbf{Q} = \mathbf{P}. \quad (2.30)$$



# Chapter 3

## Problem statement

The absolute orbit control problem can be formulated as a two spacecraft formation flying control problem, in which one of the spacecraft is virtual and not affected by non-gravitational orbit perturbations [16]. The virtual orbit, or reference orbit, represents the mean nominal motion of the satellite over a long enough time interval and must generally include the perturbations that are not intended to be corrected [11]. For a sun-synchronous orbit, such as PRISMA's and DEMETER's orbit, the reference orbit's model should at least consider the nonspherical terms of the Earth's gravitational potential which cause the motion of the ascending node (intended to precess  $360^\circ$  per year, so that the satellite always oversees interest points on the Earth's surface at the same local time) [24]. Other secular, long-periodic and short-periodic perturbations can be included in the reference orbit, depending on the mission requirements. Deviations of the real orbit from the reference, which would eventually lead to a violation of the mission requirements, must be corrected by orbital maneuvers [11].

### 3.1 Modelling the effects of the main perturbations

In order to accurately model the reference orbit and the true orbit, the main perturbations acting on a LEO spacecraft must be modelled. The reference orbit is considered to be solely under the influence of the Earth's gravitational field. The Earth's gravitational potential is modelled up to its second term, since the secular motion of the ascending node must be maintained, and  $J_2$  is orders of magnitude larger than the coefficients of the remaining zonal harmonics. The effects of the remaining perturbations must be efficiently counteracted by orbital maneuvers. The model for the true orbit must include the largest forces acting on a body in LEO. As discussed in Chapter 2, these are: the Earth's gravitational potential, which will also be modelled up to the second harmonic, and the atmospheric drag.

#### 3.1.1 Atmospheric drag

First, consider a spacecraft subject to atmospheric drag. Recall that the acceleration due to the atmospheric drag is given by

$$\mathbf{a}_D = -\frac{1}{2} \frac{C_d A}{m} \rho v_{\text{rel}}^2 \left( \frac{\mathbf{v}_{\text{rel}}}{\|\mathbf{v}_{\text{rel}}\|} \right). \quad (2.10)$$

Neglecting the velocity of the rotating atmosphere in relation to the satellite's velocity, it can be written that  $\mathbf{v}_{\text{rel}} \approx \mathbf{v}$ . Therefore

$$\mathbf{a}_D = -\frac{1}{2} \frac{C_d A}{m} \rho v^2 \hat{\mathbf{a}}_V, \quad (3.1)$$

where  $\hat{\mathbf{a}}_V$  is a unit vector aligned with the spacecraft's velocity. If the orbit is not circular, then the velocity of the spacecraft is generally not perpendicular to the orbit's radial direction. As such, it becomes necessary to write the Gauss' variational equations with the acceleration components in an MVH frame [43]. Let  $a_V$  denote the acceleration component along the spacecraft's velocity vector,  $a_M$  the acceleration component in the same direction as the radius vector (but not necessarily parallel to it), and  $a_H$  the cross-track acceleration component, completing the right-handed frame. The unit vectors of the MVH frame  $\{\hat{\mathbf{a}}_M, \hat{\mathbf{a}}_V, \hat{\mathbf{a}}_H\}$  can be written as a function of the unit vectors of an RTN frame  $\{\hat{\mathbf{a}}_R, \hat{\mathbf{a}}_T, \hat{\mathbf{a}}_N\}$ , as

$$\hat{\mathbf{a}}_V = \frac{\mathbf{v}}{v} = \frac{h_m}{\ell v} \left( e \sin v \hat{\mathbf{a}}_R + \frac{\ell}{r} \hat{\mathbf{a}}_T \right), \quad (3.2a)$$

$$\hat{\mathbf{a}}_M = \frac{h_m}{\ell v} \left( \frac{\ell}{r} \hat{\mathbf{a}}_R - e \sin v \hat{\mathbf{a}}_T \right), \quad (3.2b)$$

and  $\hat{\mathbf{a}}_H = \hat{\mathbf{a}}_N$  [43]. Therefore, the transformation between the acceleration vector components in each frame can be compactly written as

$$\begin{bmatrix} a_R \\ a_T \\ a_N \end{bmatrix} = \frac{h_m}{\ell v} \begin{bmatrix} \ell/r & e \sin v & 0 \\ -e \sin v & \ell/r & 0 \\ 0 & 0 & \ell v/h_m \end{bmatrix} \begin{bmatrix} a_M \\ a_V \\ a_H \end{bmatrix}, \quad (3.3)$$

which, as expected, is an identity when  $e = 0$ . Applying the transformation (3.3) to (2.18), the Gauss' variational equations can be written in an MVH frame as

$$\frac{da}{dt} = \frac{2a^2 v}{\mu} a_V, \quad (3.4a)$$

$$\frac{de}{dt} = \frac{1}{v} \left( \frac{r}{a} \sin v a_M + 2(e + \cos v) a_V \right), \quad (3.4b)$$

$$\frac{di}{dt} = \frac{r \cos u}{h_m} a_H, \quad (3.4c)$$

$$\frac{d\Omega}{dt} = \frac{r \sin u}{h_m \sin i} a_H, \quad (3.4d)$$

$$\frac{d\omega}{dt} = \frac{1}{ev} \left( -\left(2e + \frac{r}{a}\right) \cos v a_M + 2 \sin v a_V \right) - \frac{r \sin u \cos i}{h_m \sin i} a_H, \text{ and} \quad (3.4e)$$

$$\frac{dM}{dt} = n + \frac{b}{aev} \left( \frac{r}{a} \cos v a_M - 2 \left(1 + e^2 \frac{r}{\ell}\right) \sin v a_V \right). \quad (3.4f)$$

Note that (3.4) is applicable for every orbit, as the near-circular orbit approximation of (2.19) was not employed. Finally, the expression for the effect of the atmospheric drag on the orbital elements can be

obtained by replacing the acceleration due to atmospheric drag, given by

$$\begin{bmatrix} \mathbf{a}_M \\ \mathbf{a}_V \\ \mathbf{a}_H \end{bmatrix} = \begin{bmatrix} 0 \\ \|\mathbf{a}_D\| \\ 0 \end{bmatrix}, \quad (3.5)$$

in (3.4). The rate of change of the mean orbital elements  $\mathbf{k} = [a \ e_x \ e_y \ i \ \Omega \ u]^T$ , due to the effect of atmospheric drag on a geocentric orbit, can then be written as

$$\dot{\mathbf{k}}_d = \tilde{\mathbf{A}}_d(\mathbf{k}) = -\frac{A}{m} C_D \rho \begin{bmatrix} \sqrt{\mu_\oplus a} \\ (e_x + \cos u) \sqrt{\mu_\oplus / a} \\ (e_y + \sin u) \sqrt{\mu_\oplus / a} \\ 0 \\ 0 \\ 0 \end{bmatrix}, \quad (3.6)$$

where the short-periodic effects of drag on the eccentricity (i.e. terms depending on trigonometric functions of the argument of latitude) are considered<sup>1</sup>.

### 3.1.2 Earth's gravitational field

Assume that the Earth is symmetric about its rotational axis. In this case, the gravitational potential derived in Section 2.3.1 can be greatly simplified, while still considering the effect of the Earth's oblateness [31]. With this approximation, the disturbance potential function for the  $J_2$  component of the spherical gravitational harmonics is given by

$$U_{J_2}(r, \varphi) = -\frac{\mu_\oplus R_\oplus^2}{2} \frac{J_2}{r^3} (3 \sin^2 \varphi - 1), \quad (3.7)$$

where  $R_\oplus$  is the Earth's equatorial radius. Note that (3.7) is no longer a function of the longitude  $\lambda$ , due to the assumption of rotational symmetry. In Cartesian coordinates  $\sin \varphi = z/r$ , therefore (3.7) can be written as [43]

$$U_{J_2}(r, z) = -\frac{\mu_\oplus R_\oplus^2}{2} \frac{J_2}{r^5} (3z^2 - r^2). \quad (3.8)$$

The components of the perturbing acceleration due to  $J_2$  can be expressed, in an RTN reference frame, as [57]

$$a_{R_{J_2}} = \frac{\partial U_{J_2}}{\partial r} + \frac{\partial U_{J_2}}{\partial z} \sin i \sin u, \quad (3.9a)$$

$$a_{T_{J_2}} = \frac{\partial U_{J_2}}{\partial z} \sin i \cos u, \quad \text{and} \quad (3.9b)$$

$$a_{N_{J_2}} = \frac{\partial U_{J_2}}{\partial z} \cos i. \quad (3.9c)$$

<sup>1</sup>As previously mentioned, in this context, mean orbital elements are understood as orbital elements where the perturbations of the Earth's gravitational potential are averaged in the differential equations of motion.

The accelerations resultant from (3.9) can be substituted in (2.18), similarly to the process employed in the previous section, in order to obtain the rate of change of the osculating orbital elements due to  $J_2$ . The complete results (instantaneous element rates) are discussed in [43, p. 509-510]. The  $J_2$  perturbation results in periodic changes (short-periodic oscillations and long-periodic oscillations) and in a secular rate. The short and long-periodic oscillations will not be considered in this problem since, for long-term orbit study, the interest is in studying the secular drift [43]. Using asymptotic expansion theory, it is possible to extract the secular rates and express the mean, or orbit average, effect of  $J_2$  on the mean orbital elements as

$$\frac{\overline{da}}{dt} = \frac{\overline{de}}{dt} = \frac{\overline{di}}{dt} = 0, \quad (3.10a)$$

$$\frac{\overline{d\Omega}}{dt} = -\frac{3}{2} \left( \frac{R_{\oplus}}{a} \right)^2 \frac{nJ_2}{(1-e^2)^2} \cos i, \quad (3.10b)$$

$$\frac{\overline{d\omega}}{dt} = \frac{3}{4} \left( \frac{R_{\oplus}}{a} \right)^2 \frac{nJ_2}{(1-e^2)^2} (5 \cos^2 i - 1), \text{ and} \quad (3.10c)$$

$$\frac{\overline{dM}}{dt} = \frac{3}{4} \left( \frac{R_{\oplus}}{a} \right)^2 \frac{nJ_2}{(1-e^2)^2} \sqrt{1-e^2} (3 \cos^2 i - 1), \quad (3.10d)$$

where the mapping between mean and osculating orbital elements is found as part of Brouwer's artificial satellite theory [43, 45]. The effect of the gravitational field must also include the first term of the expansion (i.e. the mean motion  $n$ ), in order to represent the secular variation of the orbital elements caused by the Earth's gravitational field up to the second term of the harmonics expansion. Hence, the rate of the change of the mean orbital elements  $\mathbf{k}$  due to the Earth's gravitational field<sup>2</sup> can be approximated by

$$\dot{\mathbf{k}}_{J_2} = \tilde{\mathbf{A}}_g(\mathbf{k}) = \frac{3}{4} \left( \frac{R_{\oplus}}{a} \right)^2 \frac{nJ_2}{(1-e^2)^2} \begin{bmatrix} 0 \\ -(5 \cos^2 i - 1)e_y \\ (5 \cos^2 i - 1)e_x \\ 0 \\ -2 \cos i \\ 5 \cos^2 i - 1 + (3 \cos^2 i - 1)\sqrt{1-e^2} \end{bmatrix} + \begin{bmatrix} 0 \\ 0 \\ 0 \\ 0 \\ 0 \\ n \end{bmatrix}. \quad (3.11)$$

## 3.2 Nonlinear model

The state-space model of the orbital motion of the real and the reference spacecraft can be described, considering the effect of the two major perturbations, as

$$\dot{\mathbf{k}} = \tilde{\mathbf{A}}_g(\mathbf{k}) + \tilde{\mathbf{A}}_d(\mathbf{k}) + \left( \frac{\partial \zeta}{\partial \mathbf{k}_{\text{osc}}} \right) \tilde{\mathbf{B}}(\mathbf{k}_{\text{osc}}) \Delta \mathbf{v} \text{ and} \quad (3.12)$$

$$\dot{\mathbf{k}}_R = \tilde{\mathbf{A}}_g(\mathbf{k}_R), \quad (3.13)$$

respectively, where the matrices  $\tilde{\mathbf{A}}_d$  and  $\tilde{\mathbf{A}}_g$  describe the behavior of the mean orbital elements, respectively under the influence of the atmospheric drag and the Earth's gravitational field (modelled up

<sup>2</sup>Note that the effects of short and long-periodic oscillations of the Earth's gravitational potential were averaged.

to  $J_2$ ),  $\Delta \mathbf{v} = [\Delta v_R \quad \Delta v_T \quad \Delta v_N]^T$  is a velocity increment vector in an RTN frame ( $\Delta \mathbf{v} \approx \mathbf{a} \Delta t$  where  $\Delta t$  is the duration of the station-keeping maneuver, assuming constant thrust is provided),  $\mathbf{k}_R$  is the set of reference mean orbital elements and

$$\mathbf{k} = \zeta(\mathbf{k}_{\text{osc}}) \quad (3.14)$$

is an analytical transformation from the osculating orbit elements  $\mathbf{k}_{\text{osc}}$  to the mean elements  $\mathbf{k}$ , as the effect of the actuators on the system  $\tilde{\mathbf{B}}(\mathbf{k}_{\text{osc}})$ , is given by the Gauss' form of Lagrange's planetary equations adapted for near-circular orbits, which describe the variation of osculating orbital elements [43]. Employing a first-order truncation of Brouwer's analytical satellite theory for the transformation between osculating and mean orbit elements, the matrix  $(\partial \zeta / \partial \mathbf{k}_{\text{osc}})$  becomes approximately a  $6 \times 6$  identity matrix with the off-diagonal terms being of order  $J_2$  or smaller [43, 45]. Therefore, for the purposes of developing a feedback control law, it is reasonable to approximate (3.12) as [43, p. 650-651]

$$\dot{\mathbf{k}} \approx \tilde{\mathbf{A}}_g(\mathbf{k}) + \tilde{\mathbf{A}}_d(\mathbf{k}) + \tilde{\mathbf{B}}(\mathbf{k}) \Delta \mathbf{v}, \quad (3.15)$$

where  $\tilde{\mathbf{B}}(\mathbf{k})$ , which can be immediately computed from (2.22), is given by

$$\tilde{\mathbf{B}}(\mathbf{k}) = \frac{1}{v \Delta t} \begin{bmatrix} 0 & 2a & 0 \\ \sin u & 2 \cos u & 0 \\ -\cos u & 2 \sin u & 0 \\ 0 & 0 & \cos u \\ 0 & 0 & \sin u / \sin i \\ -2 & 0 & -\sin u / \tan i \end{bmatrix}. \quad (3.16)$$

Notice how the mean motion  $n$  is not included in the input matrix since this term results from the interaction between two point masses (i.e. the solution to the unperturbed problem), and thus is included in  $\tilde{\mathbf{A}}_g$ .

Finally, defining the mean orbital element vector difference as  $\boldsymbol{\xi} = \mathbf{k} - \mathbf{k}_R$ , the dynamics of the error between the orbital element vector of the true orbit and of the reference orbit, i.e. the difference between (3.15) and (3.13), can be written as

$$\dot{\boldsymbol{\xi}}(\mathbf{k}, \Delta \mathbf{v}) = \tilde{\mathbf{A}}_g(\mathbf{k}) + \tilde{\mathbf{A}}_d(\mathbf{k}) - \tilde{\mathbf{A}}_g(\mathbf{k}_R) + \tilde{\mathbf{B}}(\mathbf{k}) \Delta \mathbf{v}. \quad (3.17)$$

Furthermore, (3.17) can be written in function of the error  $\boldsymbol{\xi}$  as

$$\dot{\boldsymbol{\xi}}(\boldsymbol{\xi}, \Delta \mathbf{v}) = \tilde{\mathbf{A}}_g(\boldsymbol{\xi} + \mathbf{k}_R) + \tilde{\mathbf{A}}_d(\boldsymbol{\xi} + \mathbf{k}_R) - \tilde{\mathbf{A}}_g(\mathbf{k}_R) + \tilde{\mathbf{B}}(\boldsymbol{\xi} + \mathbf{k}_R) \Delta \mathbf{v}. \quad (3.18)$$

This thesis is focused on developing an on-board feedback control system for the dynamics described by (3.18). In compliance with the described problem formulation, station-keeping is understood as maintaining the true satellite close to the reference satellite, which fulfills the mission requirements, as it is considered to be affected solely by the Earth's gravitational field. Hence, not only do the reference and

the true orbits coincide in space, but also in *time*, in the sense that there must be no phase difference between the position of the true and the reference satellites along their respective orbits. Particularly, this thesis is focused on counteracting every perturbation except the effect of the  $J_2$  coefficient, on a near-circular low Earth orbit. While the proposed control scheme is valid for every (near-circular) low Earth orbit, it is of particular interest for sun-synchronous orbits, as it maintains the desired effect of  $J_2$  in the precession of the ascending node ( $360^\circ$  per year).

A linear time-periodic model, as well as a linear time-invariant model, which are very accurate in relation to the nonlinear model (3.18) are derived herein. To derive a model which can be generally applied in future work, it is firstly considered that the satellite is capable of actuation in the three axis. However, for the control system design, it is considered that the satellite does not have thrusters aligned with the radial axis, such that only actuation in the along-track and cross-track directions can be applied. In fact, a satellite's orbit under the influence of the Earth's gravitational pull can be controlled solely by along-track and cross-track maneuvers [58].

The validation of the proposed control system is realized by means of numerical simulations employing a high-fidelity simulator. Throughout this thesis, the high-fidelity simulator provided by the TU Delft's Astrodynamics Toolbox (Tudat) will be employed. The documentation of the simulator is available at [59] and the source code is available at [60]. In order to offer practicality, and to further on implement a feedback control law, the simulation environment relies on an interface between the C++ Tudat application and Matlab. This interface is provided by the *tudat-matlab-thrust-feedback* package, available at [61].

## Chapter 4

# On the LQR design for discrete-time linear periodic systems

Linear periodic system descriptions appear in various applications [62], such as vibration reduction in helicopter flight [63], spacecraft attitude control [64], rotor-blade vibration suppression [65], and analysis of multi-rate filters [66]. Motivated by the periodic characteristics of various phenomena, the synthesis of both continuous-time and discrete-time periodic control systems has been thoroughly studied [62]. For discrete-time linear periodic systems, the solution to the LQR is associated with the discrete-time periodic Riccati equation (DPRE) [67]. Algorithms proposed in [56] and [68], hereby denominated Hench & Laub (1994) and Yang (2017) respectively, solve the DPRE using a symplectic system which arises from the Hamiltonian minimization necessary conditions. On the other hand, the algorithm proposed in [69], hereby denominated Yang (2018), relies on a lifting method that converts the discrete-time linear periodic system into an augmented linear time-invariant equivalent, whereupon standard techniques for the algebraic Riccati equation can be applied. This solution is particularly efficient, as it takes advantage of the special structure of the augmented linear time-invariant system to solve the associated Riccati equation. However, with this methodology, the actuation is computed only once per period. Therefore, disturbances on the system are not considered until the feedback law for the next lifting period is applied.

This chapter builds on the lifting method proposed in Yang (2018) to develop an alternative algorithm to compute the optimal feedback controller gains for the discrete-time linear periodic system, always using the latest state in the feedback loop, similarly to Hench & Laub (1994) and Yang (2017). As a result, while the methodology of Yang (2018) and the one proposed in this chapter are equivalent in the absence of disturbances, the latter leads to improved robustness to system disturbances. Moreover, similarly to Yang (2018), the proposed algorithm is generally faster than both Hench & Laub (1994) and Yang (2017), and can be efficiently applied to singular periodic systems, unlike Hench & Laub (1994) and Yang (2017).

Section 4.1 briefly describes the solution to the discrete-time periodic Riccati equation, employing the algorithms of Hench & Laub (1994) and Yang (2017), as well as the lifting method proposed in

Yang (2018). Section 4.2 proposes the novel algorithm to obtain the state feedback matrices. In Section 4.3, the proposed feedback methodology and the augmented state feedback methodology are compared in the presence of sensor and process noise. Lastly, the execution time of the proposed algorithm is compared with the algorithm proposed in Hench & Laub (1994).

## 4.1 Preliminaries

The dynamics of a linear discrete-time periodic system can be compactly written as

$$\mathbf{x}_{l+1} = \mathbf{A}_l \mathbf{x}_l + \mathbf{B}_l \mathbf{u}_l, \quad (4.1)$$

where  $\mathbf{A}_l = \mathbf{A}_{l+p} \in \mathbb{R}^{n \times n}$  and  $\mathbf{B}_l = \mathbf{B}_{l+p} \in \mathbb{R}^{n \times m}$  are periodic time-varying matrices. For the discrete-time linear periodic system (4.1), the LQR state feedback problem is to determine an optimal control policy  $\mathbf{u}_l$  which minimizes the performance measure

$$J = \frac{1}{2} \lim_{N \rightarrow \infty} \left[ \mathbf{x}_{Np}^T \mathbf{S}_{Np} \mathbf{x}_{Np} + \sum_{l=0}^{Np-1} (\mathbf{x}_l^T \mathbf{Q}_l \mathbf{x}_l + \mathbf{u}_l^T \mathbf{R}_l \mathbf{u}_l) \right], \quad (4.2)$$

where  $\mathbf{S}_{Np} \succeq 0$ ,  $\mathbf{Q}_l = \mathbf{Q}_{l+p} \succeq 0$ , and  $\mathbf{R}_l = \mathbf{R}_{l+p} \succ 0$  [67]. Let  $\mathbf{Q}_l = \mathbf{C}_l^T \mathbf{C}_l$ . If the matrix pair  $(\mathbf{A}_l, \mathbf{B}_l)$  is stabilizable and the matrix pair  $(\mathbf{A}_l, \mathbf{C}_l)$  is detectable for all  $l$ , then the optimal (periodic) feedback law is given by

$$\mathbf{u}_l = -\mathbf{K}_l \mathbf{x}_l = -(\mathbf{R}_l + \mathbf{B}_l^T \mathbf{P}_{l+1} \mathbf{B}_l)^{-1} \mathbf{B}_l^T \mathbf{P}_{l+1} \mathbf{A}_l \mathbf{x}_l, \quad (4.3)$$

where  $\mathbf{P}_l$  is the unique symmetric nonnegative definite periodic stabilizing solution to the discrete-time periodic Riccati equation

$$\mathbf{P}_l = \mathbf{Q}_l + \mathbf{A}_l^T \mathbf{P}_{l+1} \mathbf{A}_l - \mathbf{A}_l^T \mathbf{P}_{l+1} \mathbf{B}_l (\mathbf{R}_l + \mathbf{B}_l^T \mathbf{P}_{l+1} \mathbf{B}_l)^{-1} \mathbf{B}_l^T \mathbf{P}_{l+1} \mathbf{A}_l, \quad (4.4)$$

with final condition  $\mathbf{P}_{Np} = \mathbf{S}_{Np}$  [67]. The LQR design problem of (4.1)-(4.2) can be solved by finding the solution to  $p$  ( $n$ -dimensional) Riccati equations, in order to obtain the  $p$  nonnegative definite matrices  $\mathbf{P}_l$  ( $l = 1, \dots, p$ ), as  $\mathbf{P}_l = \mathbf{P}_{l+p}$  [67]. Algorithms such as Hench & Laub (1994) and Yang (2017) study the symplectic system which arises from the Hamiltonian minimization necessary conditions (Euler-Lagrange equations), in order to obtain the  $p$  Riccati solutions  $\mathbf{P}_l$ . The algorithm proposed in Yang (2017) is more efficient than Hench & Laub (1994), for the case where the state matrix of the periodic system is time-invariant. However, it offers no benefits in relation to the latter when the state matrix is time-varying. Additionally, Yang (2017) cannot be applied to systems where any of the state matrices are singular. A method proposed in Hench & Laub (1994) lends itself to be applied to these situations. However, this would result in a very complex algorithm.

### 4.1.1 Equivalent augmented linear time-invariant system

The linear time-periodic (LTP) system (4.1) can be reformulated as a linear time-invariant system, employing a lifting technique [69]. The lifting technique proposed in Yang (2018) is discussed in this section.

The state equations of the LTP system (4.1) can be expanded as

$$\begin{aligned}
 \mathbf{x}_1 &= \mathbf{A}_0 \mathbf{x}_0 + \mathbf{B}_0 \mathbf{u}_0, \\
 \mathbf{x}_2 &= \mathbf{A}_1 \mathbf{x}_1 + \mathbf{B}_1 \mathbf{u}_1, \\
 &\vdots \\
 \mathbf{x}_p &= \mathbf{A}_{p-1} \mathbf{x}_{p-1} + \mathbf{B}_{p-1} \mathbf{u}_{p-1}, \\
 \mathbf{x}_{p+1} &= \mathbf{A}_0 \mathbf{x}_p + \mathbf{B}_0 \mathbf{u}_p,
 \end{aligned} \tag{4.5}$$

and so forth. Equation (4.5) can be rewritten as a function of the final state of the previous period (i.e.  $\mathbf{x}_1$  to  $\mathbf{x}_p$  can be obtained as a function of  $\mathbf{x}_0$ ), leading to

$$\begin{aligned}
 \mathbf{x}_1 &= \mathbf{A}_0 \mathbf{x}_0 + \mathbf{B}_0 \mathbf{u}_0, \\
 \mathbf{x}_2 &= \mathbf{A}_1 \mathbf{A}_0 \mathbf{x}_0 + \mathbf{A}_1 \mathbf{B}_0 \mathbf{u}_0 + \mathbf{B}_1 \mathbf{u}_1, \\
 \mathbf{x}_3 &= \mathbf{A}_2 \mathbf{A}_1 \mathbf{A}_0 \mathbf{x}_0 + \mathbf{A}_2 \mathbf{A}_1 \mathbf{B}_0 \mathbf{u}_0 + \mathbf{A}_2 \mathbf{B}_1 \mathbf{u}_1 + \mathbf{B}_2 \mathbf{u}_2,
 \end{aligned} \tag{4.6}$$

and so forth. From (4.6) results an augmented linear time-invariant (LTI) system, equivalent to the LTP system (4.1), which can be compactly written as

$$\bar{\mathbf{x}}_{k+1} = \bar{\mathbf{A}} \bar{\mathbf{x}}_k + \bar{\mathbf{B}} \bar{\mathbf{u}}_k, \tag{4.7}$$

where  $\bar{\mathbf{x}}_k \in \mathbb{R}^{pn}$  and  $\bar{\mathbf{u}} \in \mathbb{R}^{pm}$  are the augmented state and input, respectively, and  $\bar{\mathbf{A}} \in \mathbb{R}^{pn \times pn}$ ,  $\bar{\mathbf{B}} \in \mathbb{R}^{pn \times pm}$  are the augmented time-invariant system matrices [70]. The augmented state and input can be written as

$$\bar{\mathbf{x}}_k = \begin{bmatrix} \mathbf{x}_{p(k-1)+1} \\ \mathbf{x}_{p(k-1)+2} \\ \vdots \\ \mathbf{x}_{p(k-1)+p} \end{bmatrix} \text{ with } \bar{\mathbf{x}}_0 := \begin{bmatrix} \mathbf{0} \\ \mathbf{0} \\ \vdots \\ \mathbf{x}_0 \end{bmatrix}, \text{ and } \bar{\mathbf{u}}_k = \begin{bmatrix} \mathbf{u}_{pk} \\ \mathbf{u}_{pk+1} \\ \vdots \\ \mathbf{u}_{pk+p-1} \end{bmatrix}, \tag{4.8}$$

respectively. The state and input matrices can be compactly written as

$$\bar{\mathbf{A}} = \left[ \begin{array}{ccc|ccc} \mathbf{0} & \cdots & \mathbf{0} & & & \mathbf{A}_0 \\ \mathbf{0} & \cdots & \mathbf{0} & & & \mathbf{A}_1 \mathbf{A}_0 \\ \vdots & \ddots & \vdots & & & \vdots \\ \mathbf{0} & \cdots & \mathbf{0} & & & \mathbf{A}_{p-2} \cdots \mathbf{A}_1 \mathbf{A}_0 \\ \hline \mathbf{0} & \cdots & \mathbf{0} & & & \mathbf{A}_{p-1} \cdots \mathbf{A}_1 \mathbf{A}_0 \end{array} \right] = \left[ \begin{array}{c|c} \mathbf{0} & \bar{\mathbf{A}}_1 \\ \hline \mathbf{0} & \bar{\mathbf{A}}_2 \end{array} \right] \text{ and} \tag{4.9}$$

$$\bar{\mathbf{B}} = \begin{bmatrix} \mathbf{B}_0 & \mathbf{0} & \cdots & \mathbf{0} & \mathbf{0} \\ \mathbf{A}_1\mathbf{B}_0 & \mathbf{B}_1 & \cdots & \mathbf{0} & \mathbf{0} \\ \vdots & \vdots & \ddots & \vdots & \vdots \\ \mathbf{A}_{p-2}\cdots\mathbf{A}_1\mathbf{B}_0 & \mathbf{A}_{p-2}\cdots\mathbf{A}_2\mathbf{B}_1 & \cdots & \mathbf{B}_{p-2} & \mathbf{0} \\ \mathbf{A}_{p-1}\cdots\mathbf{A}_1\mathbf{B}_0 & \mathbf{A}_{p-1}\cdots\mathbf{A}_2\mathbf{B}_1 & \cdots & \mathbf{A}_{p-1}\mathbf{B}_{p-2} & \mathbf{B}_{p-1} \end{bmatrix} = \begin{bmatrix} \bar{\mathbf{B}}_1 \\ \bar{\mathbf{B}}_2 \end{bmatrix}. \quad (4.10)$$

The LQR state feedback control problem for the augmented system (4.7) involves finding the optimal control policy  $\bar{\mathbf{u}}_k$  that minimizes the quadratic performance measure

$$\bar{J} = \frac{1}{2} \lim_{N \rightarrow \infty} \left[ \bar{\mathbf{x}}_N^T \bar{\mathbf{S}}_N \bar{\mathbf{x}}_N + \sum_{k=0}^{N-1} (\bar{\mathbf{x}}_k^T \bar{\mathbf{Q}} \bar{\mathbf{x}}_k + \bar{\mathbf{u}}_k^T \bar{\mathbf{R}} \bar{\mathbf{u}}_k) \right], \quad (4.11)$$

where  $\bar{\mathbf{S}}_N \in \mathbb{R}^{pn \times pn}$ ,  $\bar{\mathbf{Q}} = \text{diag}(\mathbf{Q}_0, \dots, \mathbf{Q}_{p-1}) \in \mathbb{R}^{pn \times pn}$ , and  $\bar{\mathbf{R}} = \text{diag}(\mathbf{R}_0, \dots, \mathbf{R}_{p-1}) \in \mathbb{R}^{pm \times pm}$ . Consider  $\bar{\mathbf{Q}} = \bar{\mathbf{C}}^T \bar{\mathbf{C}}$ . As discussed in Section 2.5, under the conditions of stabilizability of  $(\bar{\mathbf{A}}, \bar{\mathbf{B}})$  and detectability of  $(\bar{\mathbf{A}}, \bar{\mathbf{C}})$ , the optimal feedback matrix for the problem (4.7)-(4.11) is given by

$$\bar{\mathbf{u}}_k = -\bar{\mathbf{K}}\bar{\mathbf{x}}_k = -(\bar{\mathbf{R}} + \bar{\mathbf{B}}^T \bar{\mathbf{P}} \bar{\mathbf{B}})^{-1} \bar{\mathbf{B}}^T \bar{\mathbf{P}} \bar{\mathbf{A}} \bar{\mathbf{x}}_k, \quad (4.12)$$

where the steady-state solution  $\bar{\mathbf{P}}$  can be found by backwards iteration of the Riccati equation (with terminal condition  $\bar{\mathbf{P}}_N = \bar{\mathbf{S}}_N$ ) until it converges, and is the unique positive definite solution of the discrete-time algebraic Riccati equation [55]

$$\bar{\mathbf{A}}^T \bar{\mathbf{P}} \bar{\mathbf{A}} - \bar{\mathbf{A}}^T \bar{\mathbf{P}} \bar{\mathbf{B}} (\bar{\mathbf{R}} + \bar{\mathbf{B}}^T \bar{\mathbf{P}} \bar{\mathbf{B}})^{-1} \bar{\mathbf{B}}^T \bar{\mathbf{P}} \bar{\mathbf{A}} + \bar{\mathbf{Q}} = \bar{\mathbf{P}}. \quad (4.13)$$

The optimal control problem described by (4.7) and (4.13) is time-invariant, however, it is equivalent to the time-varying problem described by (4.1) and (4.2) [69]. Still, the condition that all the pairs  $(\mathbf{A}_l, \mathbf{B}_l)$  are stabilizable and all pairs  $(\mathbf{A}_l, \mathbf{C}_l)$  are detectable is not equivalent to the stabilizability of  $(\bar{\mathbf{A}}, \bar{\mathbf{B}})$  and the detectability of  $(\bar{\mathbf{A}}, \bar{\mathbf{C}})$ , respectively [71]. This remark is demonstrated in Appendix B.1.

#### 4.1.2 Efficient LQR design for the augmented system

The augmented state matrix  $\bar{\mathbf{A}}$  is not invertible, so the algebraic Riccati equation (4.13) cannot be directly solved by algorithms such as [72]. It can be solved by employing the method proposed in [73], which is, however, a very complex algorithm [69]. Additionally, it is computationally expensive to solve (4.13), particularly for systems with a large amount of samples per period, as it is a  $pn$ -dimensional Riccati equation. An algorithm which makes full use of the structure of  $\bar{\mathbf{A}}$ , in which the first  $(p-1)n$  columns are null, was proposed in Yang (2018). The main results are presented here, and the algorithm is thoroughly explained in Appendix B.2. Let  $\bar{\mathbf{Q}}_1 = \text{diag}(\mathbf{Q}_0, \dots, \mathbf{Q}_{p-2})$ ,  $\bar{\mathbf{R}}_1 = \text{diag}(\mathbf{R}_0, \dots, \mathbf{R}_{p-2})$ ,  $\bar{\mathbf{Q}}_2 = \mathbf{Q}_{p-1} \in \mathbb{R}^{n \times n}$ , and  $\bar{\mathbf{R}}_2 = \mathbf{R}_{p-1} \in \mathbb{R}^{m \times m}$ . Additionally, denote

$$\hat{\mathbf{A}} = \bar{\mathbf{A}}_2, \hat{\mathbf{B}} = \bar{\mathbf{B}}_2, \quad (4.14a)$$

$$\hat{\mathbf{Q}} = \bar{\mathbf{Q}}_2 + \bar{\mathbf{A}}_1^T \bar{\mathbf{Q}}_1 \bar{\mathbf{A}}_1 \in \mathbb{R}^{n \times n}, \quad (4.14b)$$

$$\hat{\mathbf{R}} = \bar{\mathbf{R}} + \bar{\mathbf{B}}_1^T \bar{\mathbf{Q}}_1 \bar{\mathbf{B}}_1 \in \mathbb{R}^{pm \times pm}, \text{ and} \quad (4.14c)$$

$$\hat{\mathbf{S}} = \bar{\mathbf{A}}_1^T \bar{\mathbf{Q}}_1 \bar{\mathbf{B}}_1 \in \mathbb{R}^{n \times pm}. \quad (4.14d)$$

One of the main results of Yang (2018) was showing that the solution to the Riccati equation (4.13) is given by  $\bar{\mathbf{P}} = \text{diag}(\bar{\mathbf{Q}}_1, \hat{\mathbf{P}})$ , where  $\hat{\mathbf{P}} \in \mathbb{R}^{n \times n}$  is the solution to the Riccati equation

$$\hat{\mathbf{A}}^T \hat{\mathbf{P}} \hat{\mathbf{A}} - \underbrace{\left( \hat{\mathbf{A}}^T \hat{\mathbf{P}} \hat{\mathbf{B}} + \hat{\mathbf{S}} \right)}_{n \times pm} \underbrace{\left( \hat{\mathbf{B}}^T \hat{\mathbf{P}} \hat{\mathbf{B}} + \hat{\mathbf{R}} \right)^{-1}}_{pm \times pm} \underbrace{\left( \hat{\mathbf{B}}^T \hat{\mathbf{P}} \hat{\mathbf{A}} + \hat{\mathbf{S}}^T \right)}_{pm \times n} + \hat{\mathbf{Q}} = \hat{\mathbf{P}}. \quad (4.15)$$

The Riccati equation (4.15) is discussed in [74], and can be solved by the algorithm implemented in the Matlab function `idare`. Employing the proposed algorithm, the optimal control problem for the time-invariant augmented system requires the solution of the Riccati equation (4.15), where  $\hat{\mathbf{P}} \in \mathbb{R}^{n \times n}$ , instead of the Riccati equation (4.13), where  $\bar{\mathbf{P}} \in \mathbb{R}^{pn \times pn}$ . Moreover, the proposed method only requires the solution of one  $n$ -dimensional Riccati equation, whereas Hench & Laub (1994) and Yang (2017) solve  $p$   $n$ -dimensional Riccati equations [69].

## 4.2 Feedback of the most recent state

Studying the expression of the augmented feedback matrix, given by (4.12), the following theorem can be derived.

**Theorem 1.** *The optimal feedback law for the lifted system can be written as  $\bar{\mathbf{u}}_k = - \left[ \mathbf{0}_{pm \times (p-1)n} \mid \hat{\mathbf{K}} \right]$ , where  $\hat{\mathbf{K}} \in \mathbb{R}^{pm \times n}$  is the optimal state feedback matrix associated with the Riccati equation (4.15).*

*Proof.* The theorem is proved in Appendix B.3.

From Theorem 1, it can be concluded that the first  $(p-1)n$  columns of the augmented state feedback matrix  $\bar{\mathbf{K}}$  are null and, as such, the augmented state feedback law applied over a period solely depends on the final time instant of the previous period. For systems with large periods, the state considered in the feedback law can be several hours old and unmodelled perturbations are not compensated until the feedback law for the following period is obtained. Additionally, due to sensor noise, the only measurement taken into consideration for the control policy applied to an entire period could be unreliable. This section proposes an algorithm to compute the set of feedback matrices  $\mathbf{K}_l$  for feedback of the most recent state that is available, utilizing the augmented state feedback matrix  $\bar{\mathbf{K}}$ .

For simplicity, consider  $k = 1$ . The augmented state feedback law is given by

$$\begin{bmatrix} \mathbf{u}_p \\ \mathbf{u}_{p+1} \\ \vdots \\ \mathbf{u}_{2p-1} \end{bmatrix} = - \left[ \mathbf{0} \mid \hat{\mathbf{K}} \right] \bar{\mathbf{x}}_1 = - \begin{bmatrix} \mathbf{0} & \dots & \mathbf{0} & \hat{\mathbf{K}}_0 \\ \vdots & \ddots & \vdots & \vdots \\ \mathbf{0} & \dots & \mathbf{0} & \hat{\mathbf{K}}_{p-1} \end{bmatrix} \begin{bmatrix} \mathbf{x}_1 \\ \mathbf{x}_2 \\ \vdots \\ \mathbf{x}_p \end{bmatrix}$$

where  $\hat{\mathbf{K}}_l \in \mathbb{R}^{m \times n}$ , and can be written as a function of the final state of the previous period,  $\mathbf{x}_p$ , as

$$\mathbf{u}_{p+l} = -\hat{\mathbf{K}}_l \mathbf{x}_p, \text{ for } l = 0, \dots, p-1. \quad (4.16)$$

Let  $\mathbf{\Pi}_l \in \mathbb{R}^{n \times n}$  be a linear transformation from  $\mathbf{x}_{p+l}$  to  $\mathbf{x}_{p+l+1}$ . Using the set of transformations  $\mathbf{\Pi}_l$ , it can be written that

$$\begin{aligned} \mathbf{x}_{p+1} &= \mathbf{\Pi}_0 \mathbf{x}_p, \\ \mathbf{x}_{p+2} &= \mathbf{\Pi}_1 \mathbf{x}_{p+1}, \\ \mathbf{x}_{p+3} &= \mathbf{\Pi}_2 \mathbf{x}_{p+2}, \end{aligned} \quad (4.17)$$

and so on. Consider, for now, that all transformations  $\mathbf{\Pi}_l$  are invertible. Then, it can be noted that the state  $\mathbf{x}_p$  can be written as a function of any state of the following period, following

$$\begin{aligned} \mathbf{x}_p &= \mathbf{\Pi}_0^{-1} \mathbf{x}_{p+1}, \\ \mathbf{x}_p &= (\mathbf{\Pi}_1 \mathbf{\Pi}_0)^{-1} \mathbf{x}_{p+2}, \\ \mathbf{x}_p &= (\mathbf{\Pi}_2 \mathbf{\Pi}_1 \mathbf{\Pi}_0)^{-1} \mathbf{x}_{p+3}, \end{aligned} \quad (4.18)$$

and so on, or generally

$$\mathbf{x}_p = \left( \prod_{i=0}^{l-1} \mathbf{\Pi}_{l-1-i} \right)^{-1} \mathbf{x}_{p+l}, \text{ for } l = 1, \dots, p-1. \quad (4.19)$$

Substituting (4.19) in (4.16), a new feedback law for the most recent state arises as

$$\begin{aligned} \mathbf{u}_{p+l} &= -\mathbf{K}_l \mathbf{x}_{p+l}, \text{ where} \\ \left\{ \begin{array}{l} \mathbf{K}_0 = \hat{\mathbf{K}}_0 \\ \mathbf{K}_l = \hat{\mathbf{K}}_l \left( \prod_{i=0}^{l-1} \mathbf{\Pi}_{l-1-i} \right)^{-1}, \text{ for } l = 1, \dots, p-1. \end{array} \right. \end{aligned} \quad (4.20)$$

Note that the feedback law for the first step of the period is the same for both methods, since at this step the most recent state is the final state of the previous period. Additionally, the (last) state feedback law of (4.20) coincides with the feedback law obtained by Hench & Laub (1994) and Yang (2017). Finally, it must be shown that the transformations  $\mathbf{\Pi}_l$  do not depend on the period ( $k$ ) considered. With that goal, consider the closed-loop plant. Given the specific structure of both  $\bar{\mathbf{A}}$  and  $\bar{\mathbf{K}}$ , it can be concluded that the first  $(p-1)n$  columns of  $\bar{\mathbf{A}} - \bar{\mathbf{B}}\bar{\mathbf{K}}$  are zero. Studying (4.17) and noting that

$$\bar{\mathbf{x}}_{k+1} = (\bar{\mathbf{A}} - \bar{\mathbf{B}}\bar{\mathbf{K}}) \bar{\mathbf{x}}_k, \quad (4.21)$$

it can be obtained that

$$\bar{\mathbf{A}} - \bar{\mathbf{B}}\bar{\mathbf{K}} = \left[ \begin{array}{ccc|ccc} \mathbf{0} & \dots & \mathbf{0} & & & \mathbf{\Pi}_0 \\ \mathbf{0} & \dots & \mathbf{0} & & & \mathbf{\Pi}_1 \mathbf{\Pi}_0 \\ \vdots & & \vdots & & & \vdots \\ \vdots & & \vdots & & & \mathbf{\Pi}_{p-2} \mathbf{\Pi}_{p-3} \dots \mathbf{\Pi}_0 \\ \hline \mathbf{0} & \dots & \mathbf{0} & & & \mathbf{\Pi}_{p-1} \mathbf{\Pi}_{p-2} \dots \mathbf{\Pi}_0 \end{array} \right]. \quad (4.22)$$

The closed-loop plant is time-invariant and, since (4.21) is applicable for every  $k$ , it can be noted that  $\mathbf{\Pi}_0 = \mathbf{\Pi}_p$ . Moreover, it can be written that  $\mathbf{\Pi}_1 \mathbf{\Pi}_0 = \mathbf{\Pi}_{p+1} \mathbf{\Pi}_p$ , so  $\mathbf{\Pi}_1 = \mathbf{\Pi}_{p+1}$  (considering that  $\mathbf{\Pi}_0^{-1}$  exists). Through this process, it can be shown that the transformations  $\mathbf{\Pi}_l$  do not depend on the period ( $k$ ) considered. As a result, the feedback matrices  $\mathbf{K}_l$  are periodic, with period  $p$  (as expected, since these coincide with the results from Hensch & Laub (1994) and Yang (2017)). Note that the transformations  $\mathbf{\Pi}_l$  do not need to be explicitly computed, since the last state feedback matrices can simply be obtained from

$$\begin{aligned} \mathbf{K}_0 &= \hat{\mathbf{K}}_0, \\ \mathbf{K}_1 &= \hat{\mathbf{K}}_1(\mathbf{\Pi}_0)^{-1}, \\ \mathbf{K}_2 &= \hat{\mathbf{K}}_2(\mathbf{\Pi}_1 \mathbf{\Pi}_0)^{-1}, \\ &\vdots \\ \mathbf{K}_{p-1} &= \hat{\mathbf{K}}_{p-1}(\mathbf{\Pi}_{p-2} \mathbf{\Pi}_{p-3} \dots \mathbf{\Pi}_0)^{-1}, \end{aligned} \quad (4.23)$$

where the matrices  $\mathbf{\Pi}_0, \mathbf{\Pi}_1 \mathbf{\Pi}_0, \dots, \mathbf{\Pi}_{p-2} \mathbf{\Pi}_{p-3} \dots \mathbf{\Pi}_0$  are given by (4.22). This approach aims to minimize the number of matrix inversions employed by the algorithm, to increase robustness to numerical error in case of ill-conditioned matrices  $\mathbf{\Pi}_l$ . Moreover, this approach is computationally faster than calculating the matrices  $\mathbf{\Pi}_l$  from (4.17).

In order to employ the proposed method, that obtains the last state feedback matrices from (4.23), the transformations  $\mathbf{\Pi}_l, l = 0, \dots, p-2$ , must be invertible. The following theorem provides a sufficient and necessary condition for the invertibility of all transformations  $\mathbf{\Pi}_l, l = 0, \dots, p-1$ .

**Theorem 2.** *All transformations  $\mathbf{\Pi}_l, l = 0, \dots, p-1$ , are invertible if and only if  $\tilde{\mathbf{A}} = \hat{\mathbf{A}} - \hat{\mathbf{B}}\hat{\mathbf{R}}^{-1}\hat{\mathbf{S}}^T \in \mathbb{R}^{n \times n}$  is invertible.*

*Proof.* Studying (4.9), (4.10), and (4.14), the closed-loop plant can be written as

$$\bar{\mathbf{A}} - \bar{\mathbf{B}}\bar{\mathbf{K}} = \left[ \begin{array}{c|c} \mathbf{0} & \bar{\mathbf{A}}_1 - \bar{\mathbf{B}}_1 \hat{\mathbf{K}} \\ \hline \mathbf{0} & \hat{\mathbf{A}} - \hat{\mathbf{B}}\hat{\mathbf{K}} \end{array} \right]. \quad (4.24)$$

Therefore, considering (4.22), it can be reasoned that  $\mathbf{\Pi}_{p-1} \mathbf{\Pi}_{p-2} \dots \mathbf{\Pi}_0 = \hat{\mathbf{A}} - \hat{\mathbf{B}}\hat{\mathbf{K}}$ . That is, the eigenvalues of the product of the transformations coincide with the closed-loop poles of the system associated with the Riccati equation (4.15). Denote

$$\tilde{\mathbf{A}} = \hat{\mathbf{A}} - \hat{\mathbf{B}}\hat{\mathbf{R}}^{-1}\hat{\mathbf{S}}^T \text{ and } \tilde{\mathbf{Q}} = \hat{\mathbf{Q}} - \hat{\mathbf{S}}\hat{\mathbf{R}}^{-1}\hat{\mathbf{S}}^T. \quad (4.25)$$

The Riccati equation (4.15) can be solved either by Schur decomposition or eigendecomposition of the generalized eigenvalue problem

$$\mathbf{M}\mathbf{z} = \lambda\mathbf{L}\mathbf{z} \quad (4.26)$$

with

$$\mathbf{L} = \begin{bmatrix} \mathbf{I} & \tilde{\mathbf{V}} \\ \mathbf{0} & \tilde{\mathbf{A}}^T \end{bmatrix} \text{ and } \mathbf{M} = \begin{bmatrix} \tilde{\mathbf{A}}^T & \mathbf{0} \\ -\tilde{\mathbf{Q}} & \mathbf{I} \end{bmatrix}, \quad (4.27)$$

where  $\tilde{\mathbf{V}} = \hat{\mathbf{B}}\tilde{\mathbf{R}}^{-1}\hat{\mathbf{B}}^T$  [56]. The  $2n$  eigenvalues of (4.26) include  $n$  eigenvalues inside the unit circle, which coincide with the closed-loop poles of the system. The remaining  $n$  are their inverse (in the discrete case) [73, 75]. Moreover, it can be shown that, for the generalized eigenvalue problem (4.26), if  $\lambda = 0$  is an eigenvalue with multiplicity  $r$ , then there are only  $2n - r$  finite eigenvalues for the problem. The  $r$  missing eigenvalues may be denominated as *infinite* eigenvalues (or *reciprocals of 0*) [73]. Therefore, the eigenvalues of this problem can be arranged as

$$\underbrace{0, \dots, 0}_r, \underbrace{\lambda_{r+1}, \dots, \lambda_n}_{n-r}, \underbrace{\frac{1}{\lambda_n}, \dots, \frac{1}{\lambda_{r+1}}}_{n-r}, \underbrace{\infty, \dots, \infty}_r, \text{ where} \quad (4.28)$$

$$0 < |\lambda_i| < 1, i = r + 1, \dots, n.$$

It can be noted that if  $\tilde{\mathbf{A}}$  is nonsingular, then all the eigenvalues of the generalized eigenvalue problem (4.26) and, by consequence, all the eigenvalues of  $\hat{\mathbf{A}} - \hat{\mathbf{B}}\hat{\mathbf{K}}$ , are nonzero. This can be proved by contradiction. If  $\lambda = 0$  were an eigenvalue, it would result from (4.26) that  $\mathbf{M}\mathbf{z} = \mathbf{0}$ . Therefore,

$$\begin{bmatrix} \tilde{\mathbf{A}}^T & \mathbf{0} \\ -\tilde{\mathbf{Q}} & \mathbf{I} \end{bmatrix} \begin{bmatrix} \mathbf{z}_1 \\ \mathbf{z}_2 \end{bmatrix} = \mathbf{0}, \quad (4.29)$$

which implies that  $\mathbf{z}_1 = \mathbf{0}$ , and  $\mathbf{z}_2 = \mathbf{0}$  (trivial solution). On the other hand, if  $\tilde{\mathbf{A}}$  is singular, there is at least one eigenvalue equal to zero, because (4.29) has a nontrivial solution [73]. Therefore, if  $\tilde{\mathbf{A}}$  is invertible, then the product  $\mathbf{\Pi}_{p-1}\mathbf{\Pi}_{p-2}\dots\mathbf{\Pi}_0$  is also invertible. Since the product of two matrices is invertible if and only if both matrices are invertible [76], it can be concluded that all transformations  $\mathbf{\Pi}_l$  are invertible. On the other hand, if  $\tilde{\mathbf{A}}$  is singular, then at least one of the transformations  $\mathbf{\Pi}_l$  must be singular.  $\square$

In order to avoid utilizing Matlab's `idare`, as it obtains more information than is strictly necessary, if  $\tilde{\mathbf{A}}$  is invertible (and by consequence, both  $\mathbf{L}$  and  $\mathbf{M}$  are invertible), then the eigenvalue problem (4.26) is reduced to solving the eigenvalue problem  $\mathbf{Z} = \mathbf{L}^{-1}\mathbf{M}$ . It can be shown that  $\mathbf{Z}$  is symplectic [69] and that, as a result, the Schur decomposition of  $\mathbf{Z}$  can be written as

$$\begin{bmatrix} \mathbf{W}_{11} & \mathbf{W}_{12} \\ \mathbf{W}_{21} & \mathbf{W}_{22} \end{bmatrix}^T \mathbf{Z} \begin{bmatrix} \mathbf{W}_{11} & \mathbf{W}_{12} \\ \mathbf{W}_{21} & \mathbf{W}_{22} \end{bmatrix} = \begin{bmatrix} \mathbf{U}_{11} & \mathbf{U}_{12} \\ \mathbf{0} & \mathbf{U}_{22} \end{bmatrix}, \quad (4.30)$$

where  $\mathbf{U}_{11}$  is upper-triangular and has all of its eigenvalues outside the unit circle [69]. The solution of the discrete-time algebraic Riccati equation (4.15) can then be written as [68]

$$\hat{\mathbf{P}} = \mathbf{W}_{21}\mathbf{W}_{11}^{-1}. \quad (4.31)$$

#### 4.2.1 Proposed solution for singular $\tilde{\mathbf{A}}$

According to Theorem 2, if  $\tilde{\mathbf{A}}$  is singular, then there exists at least one transformation  $\mathbf{\Pi}_l$  which is not invertible and, as such, the proposed method cannot be applied (unless only the transformation  $\mathbf{\Pi}_{p-1}$ , which does not appear in (4.23), is singular). However, the algorithm proposed in Yang (2018)

can compute the solution of the Riccati equation (4.15) regardless of the invertibility of  $\tilde{\mathbf{A}}$ . This section proposes a method to compute the last state feedback matrices  $\mathbf{K}_0, \dots, \mathbf{K}_{p-1}$  that relies on the Riccati solution  $\hat{\mathbf{P}}$  (and not  $\mathbf{\Pi}_l$ ). As a result, the proposed algorithm does not require  $\tilde{\mathbf{A}}$  to be invertible. The following theorem establishes a key result that enables the proposed algorithm.

**Theorem 3.** *The Riccati solution  $\hat{\mathbf{P}}$  is the initial solution  $\mathbf{P}_0$  of the DPRE (4.4).*

*Proof.* The theorem is proved in Appendix B.4.

After obtaining  $\hat{\mathbf{P}} = \mathbf{P}_0 = \mathbf{P}_p$ , the remaining Riccati solutions  $\mathbf{P}_l$  can be obtained by backwards iteration of (4.4), and the optimal feedback matrices can be obtained from (4.3).

## 4.2.2 Algorithm

The proposed algorithm can be summarized as follows.

---

**Algorithm 1** Solution to the DPRE via lifting method

---

**Data**  $\mathbf{A}_0, \dots, \mathbf{A}_{p-1}, \mathbf{B}_0, \dots, \mathbf{B}_{p-1}, \mathbf{Q}_0, \dots, \mathbf{Q}_{p-1}, \mathbf{R}_0, \dots, \mathbf{R}_{p-1}$ .

**Output** Augmented state and last state feedback matrices.

---

- *Step 1:* Form the lifted system matrices  $\tilde{\mathbf{A}}, \tilde{\mathbf{B}}, \tilde{\mathbf{Q}}$ , and  $\tilde{\mathbf{R}}$ .
  - *Step 2:* Obtain the augmented state feedback matrix  $\tilde{\mathbf{K}}$  (or the Riccati solution  $\hat{\mathbf{P}}$ ).
    - *Step 2.1* Form  $\hat{\mathbf{A}}, \hat{\mathbf{B}}, \hat{\mathbf{Q}}, \hat{\mathbf{R}}$ , and  $\hat{\mathbf{S}}$  (See [69] for an efficient algorithm to form these matrices).
    - *Step 2.2* Obtain the solution  $\hat{\mathbf{P}}$  of the Riccati equation (4.15), employing the Schur decomposition (4.30) if  $\hat{\mathbf{A}}$  is invertible, or using Matlab's `idare` or [73] if  $\hat{\mathbf{A}}$  is singular. The augmented state feedback matrix can be obtained according to Theorem 1.
  - *Step 3, Method 1:* Obtain the state feedback matrices  $\mathbf{K}_l$  (Applicable if  $\tilde{\mathbf{A}}$  is invertible).
    - Compute the block  $\tilde{\mathbf{A}}_1 - \tilde{\mathbf{B}}_1 \tilde{\mathbf{K}}$  of the closed-loop plant and obtain the necessary products of the transformations  $\mathbf{\Pi}_l$ , according to (4.22). Compute the state feedback matrices  $\mathbf{K}_l$  with (4.23).
  - *Step 3, Method 2:* Obtain the state feedback matrices  $\mathbf{K}_l$  (Always applicable).
    - Starting with  $\hat{\mathbf{P}} = \mathbf{P}_0 = \mathbf{P}_p$ , iterate backwards through (4.4) to find the remaining solutions  $\mathbf{P}_l$ , where  $l = 1, \dots, p - 1$ . Compute the state feedback matrices  $\mathbf{K}_l$  with (4.3).
- 

## 4.3 Numerical results and algorithm efficiency

Consider the synthetic discrete-time linear periodic system

$$\mathbf{x}_{l+1} = \mathbf{A}_l \mathbf{x}_l + \mathbf{B}_l \mathbf{u}_l, \quad (4.32)$$

where  $\mathbf{x} \in \mathbb{R}^3$  is the state vector,  $\mathbf{u} \in \mathbb{R}^2$  is the input vector, and the state and input matrices are

$$\mathbf{A}_l = \tau_s \begin{bmatrix} 1/\tau_s & -0.02 & 0.02 \\ -0.02 \sin(2\omega_0 \tau_s l) & 1/\tau_s & 0.05 \\ -0.02 & -0.05 & 1/\tau_s \end{bmatrix} \text{ and } \mathbf{B}_l = 10^{-2} \tau_s \begin{bmatrix} 0.2 & -0.2 \\ 0.2 & \cos(\omega_0 \tau_s l) \\ \sin(\omega_0 \tau_s l) & -0.2 \end{bmatrix}, \quad (4.33)$$

respectively, where  $\tau_s$  is the sample time and  $\omega_0 = 2\pi/T_p$ . Let  $\tau_s = 1$  and  $T_p = 100$ . In this case, the state matrix is periodic with period  $p_A = 50$ , while the input matrix has a period of  $p_B = 100$ . Therefore, the number of samples per period is  $p = 100$ . The lifting technique of Yang (2018) can be employed to obtain an equivalent linear time-invariant system, as in (4.7).

Consider that the disturbances acting on the system, as well as the sensor noise, can be modelled as white process noise,  $\mathbf{w}_p$  and  $\mathbf{w}_r$ , respectively. The discrete-time state space model is

$$\mathbf{x}_{l+1} = \mathbf{A}_l \mathbf{x}_l + \mathbf{B}_l \mathbf{u}_l + \mathbf{w}_{pl}, \quad (4.34)$$

and the state measurements are  $\hat{\mathbf{x}}_l = \mathbf{x}_l + \mathbf{w}_{rl}$ . The covariance matrices of the process noise and sensor noise are  $E(\mathbf{w}_{pl} \mathbf{w}_{pl}^T) = \sigma_p^2 \mathbf{I}$  and  $E(\mathbf{w}_{rl} \mathbf{w}_{rl}^T) = \sigma_r^2 \mathbf{I}$ , respectively. The root-mean-square (RMS) of the magnitude of the state vector (over  $N$  periods) can be written as

$$\text{RMS}(\|\mathbf{x}\|) = \sqrt{\frac{1}{Np} \sum_{l=0}^{Np} \|\mathbf{x}_l\|^2}. \quad (4.35)$$

The RMS of the state vector of the system (4.32)-(4.33) is represented in Figure 4.1, for the first 100 periods, as a function of the covariance of the process noise (considering no sensor noise, and sensor noise with  $\sigma_r^2 = 0.05$ ), for the augmented state feedback methodology of (4.16) and the last state feedback methodology of (4.20). The initial state is  $\mathbf{x}_0 = (1, 1, 1)^T$  and the weighting matrices were chosen as  $\mathbf{Q}_l = \text{diag}(10, 10, 10)$  and  $\mathbf{R}_l = \text{diag}(1, 1)$ , for all  $l$ . It can be noted that, in the absence of disturbances and uncertainty in the measurements ( $\sigma_p = \sigma_r = 0$ ), the studied feedback methods present the same results. However, when subjected to sensor noise and process noise, the last state feedback methodology is preferable to augmented state feedback. The fact that the closed-loop linear time-periodic system with state feedback is more robust to system disturbances than the closed-loop linear time-invariant system with augmented state feedback motivates the computation of the last state feedback matrices.

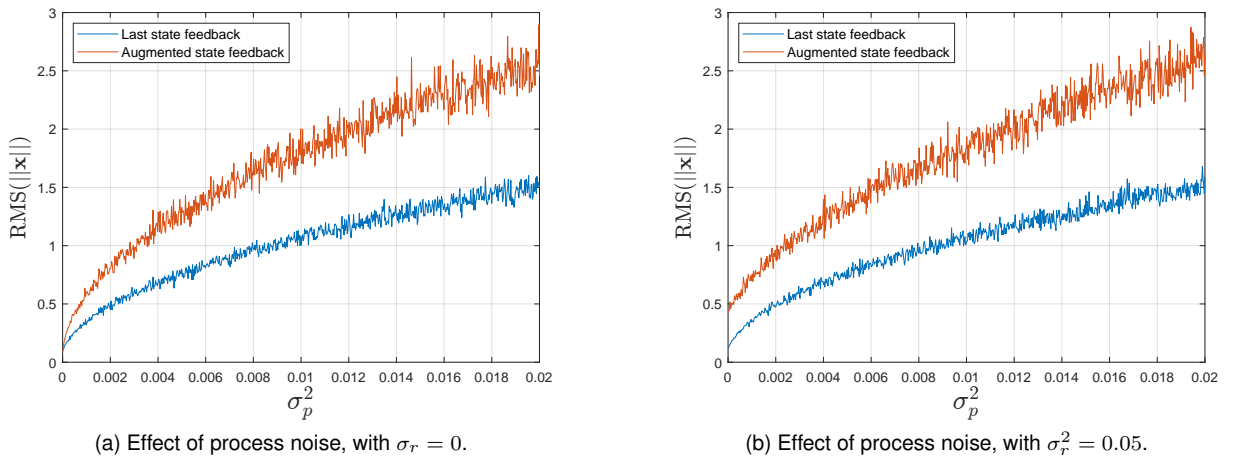


Figure 4.1: Effect of process noise on both feedback methodologies.

Yang (2017) has been shown to be less efficient than the lifting technique proposed in Yang (2018), except when the number of samples per period, the number of states and/or the number of inputs of the system is large [69]. The proposed algorithm employs the lifting technique proposed in Yang (2018), and obtaining the last state feedback matrices (third step of Algorithm 1) takes a very small percentage of the total execution time of the algorithm. In fact, as the number of samples per period increases, the execution time of the third step of the algorithm becomes negligible in relation to the time required to form the augmented system matrices. Therefore, the proposed algorithm remains more efficient than Yang (2017), when the number of samples per period is moderate.

For the synthetic system (4.32)-(4.33), the first method to obtain the last state feedback matrices (i.e. Step 3, Method 1 of Algorithm 1) is the most efficient when the number of samples per period is small or moderate (until  $p \sim 750$ ). When the number of samples per period increases, the second method becomes the most efficient. This is largely due to the fact that the first method requires the computation of the matrix  $\bar{\mathbf{A}}_1 - \bar{\mathbf{B}}_1 \hat{\mathbf{K}}$ , which takes significantly more time to obtain as  $p$  increases, whereas the second method involves iterating  $p - 1$  times through (4.4), which remains an  $n$ -dimensional equation and, as such, the execution time of the second method increases linearly with the number of samples per period.

The execution times of Hench & Laub (1994), when applied to the synthetic system (4.32)-(4.33) with varying number of samples per period, are presented in Table 4.1 alongside the total execution times of Algorithm 1. The third step of Algorithm 1 was conducted by the most efficient method for the number of samples per period tested. Hench & Laub (1994) is less efficient than the proposed algorithm, particularly if the number of samples per period is moderate. This may not be the case for augmented systems with larger number of states, inputs, or samples per period, as discussed in Yang (2018).

| Samples per period | Algorithm 1 | Hench & Laub (1994) |
|--------------------|-------------|---------------------|
| 50                 | 2.5 ms      | 9.4 ms              |
| 100                | 8.9 ms      | 34 ms               |
| 500                | 0.25 s      | 0.79 s              |
| 1000               | 1.1 s       | 3.2 s               |

Table 4.1: Execution time comparison for the synthetic system (4.32)-(4.33)<sup>1</sup>.

Besides being more efficient than Hench & Laub (1994) and Yang (2017), and being more robust to perturbations than Yang (2018), the method developed in this chapter also has the advantage of remaining simple and efficient when applied to singular systems, unlike Hench & Laub (1994) and Yang (2017). The algorithm is validated for a system with a singular matrix  $\tilde{\mathbf{A}}$  in Section B.5. Besides the computation of the state feedback matrices, the lifted time-invariant system remains a helpful tool for the analysis of the periodic system.

<sup>1</sup>The algorithms were implemented on version 2021a of Matlab, and executed by a machine with 16 GB of RAM and an AMD Ryzen 7 5800H (3.20 GHz) processor.



## Chapter 5

# Periodic model of the orbital motion

Considering the periodic properties of a satellite's orbit, it is feasible that a periodic model expressing the deviation of the true orbit from the reference orbit could be derived. An accurate discrete-time linear periodic model would prove beneficial, as an equivalent LTI model could then be obtained, and the LQR design problem would require the solution of the associated discrete-time algebraic Riccati equation, which can be efficiently computed by the technique outlined in Chapter 4. To that end, the present chapter aims to develop a linear periodic model of the relevant dynamics. In Section 5.1, the nonlinear system developed in Chapter 3 is linearized, resulting in a linear time-varying system. A discrete-time linear periodic system, aiming to approximate the linear time-varying system, is developed in Section 5.2. The discrete-time linear periodic model and, by extension, the equivalent augmented LTI model, are validated in Section 5.3, being compared with the nonlinear model developed in Chapter 3, the linear time-varying model, and the true motion of the spacecraft obtained with a high-fidelity simulator.

### 5.1 Linearized dynamic model

Recall that the dynamics of the error between the orbital element vector of the true orbit and the reference orbit can be written as

$$\dot{\boldsymbol{\xi}}(\boldsymbol{\xi}, \Delta \mathbf{v}) = \tilde{\mathbf{A}}_g(\boldsymbol{\xi} + \mathbf{k}_R) + \tilde{\mathbf{A}}_d(\boldsymbol{\xi} + \mathbf{k}_R) - \tilde{\mathbf{A}}_g(\mathbf{k}_R) + \tilde{\mathbf{B}}(\boldsymbol{\xi} + \mathbf{k}_R)\Delta \mathbf{v}, \quad (3.18)$$

where  $\boldsymbol{\xi}$  is a column vector of the difference between the real orbit's and the reference orbit's mean orbital elements (in the chosen parametrization  $\mathbf{k}$ ). Let the relative orbital element vector be defined as

$$\boldsymbol{\epsilon} := a_R \begin{bmatrix} \delta a \\ \delta e_x \\ \delta e_y \\ \delta i_x \\ \delta i_y \\ \delta u \end{bmatrix} = a_R \begin{bmatrix} (a - a_R)/a_R \\ e_x - e_{xR} \\ e_y - e_{yR} \\ i - i_R \\ (\Omega - \Omega_R) \sin i_R \\ u - u_R \end{bmatrix}, \quad (5.1)$$

where the subscript  $R$  indicates the reference orbital elements. The relative orbital element vector can be written as  $\epsilon = \mathbf{T}(\mathbf{k}_R)\xi$ , where  $\mathbf{T} = \text{diag}(1, a_R, a_R, a_R, a_R \sin i_R, a_R)$ . Since the reference orbit is only affected by the Earth's gravitational field, the reference semi-major axis and the reference inclination remain approximately constant. Therefore,  $\dot{\mathbf{T}} \approx 0$  and  $\dot{\epsilon}(\epsilon, \Delta\mathbf{v}) \approx \mathbf{T}\dot{\xi}(\xi, \Delta\mathbf{v})$ . Let

$$\begin{cases} \mathbf{A}_g(\mathbf{k}) = \mathbf{T}\tilde{\mathbf{A}}_g(\mathbf{k}), \\ \mathbf{A}_d(\mathbf{k}) = \mathbf{T}\tilde{\mathbf{A}}_d(\mathbf{k}), \text{ and} \\ \mathbf{B}(\mathbf{k}) = \mathbf{T}\tilde{\mathbf{B}}(\mathbf{k}). \end{cases} \quad (5.2)$$

The dynamics of the error between the orbital elements vector of the true orbit and the reference orbit can be written as a function of the relative orbital element vector as  $\dot{\epsilon} = f(\epsilon, \Delta\mathbf{v})$ , where

$$f(\epsilon, \Delta\mathbf{v}) = \mathbf{A}_g(\mathbf{k}_f) + \mathbf{A}_d(\mathbf{k}_f) - \mathbf{A}_g(\mathbf{k}_R) + \mathbf{B}(\mathbf{k}_f)\Delta\mathbf{v}, \quad (5.3)$$

with  $\mathbf{k}_f = \mathbf{T}^{-1}\epsilon + \mathbf{k}_R$ . Consider

$$\begin{cases} \epsilon(t) = \epsilon_0 + \delta\epsilon(t), \\ \Delta\mathbf{v}(t) = \Delta\mathbf{v}_0 + \delta(\Delta\mathbf{v}(t)), \end{cases} \quad (5.4)$$

where the pair  $(\epsilon_0, \Delta\mathbf{v}_0)$  is an equilibrium point and  $\delta\epsilon$ ,  $\delta(\Delta\mathbf{v})$  are small perturbations in  $\epsilon$  and  $\Delta\mathbf{v}$ , respectively. The pair  $(\epsilon_0 = \mathbf{0}, \Delta\mathbf{v}_0)$  is an equilibrium point, with

$$f(\mathbf{0}, \Delta\mathbf{v}_0) = \mathbf{A}_d(\mathbf{k}_R) + \mathbf{B}(\mathbf{k}_R)\Delta\mathbf{v}_0 = \mathbf{0}, \quad (5.5)$$

where the equilibrium delta-v is given by

$$\Delta\mathbf{v}_{0(\text{MVH})} = \frac{A}{m}C_D\rho \begin{bmatrix} 0 \\ \mu_{\oplus}/(2a_R) \\ 0 \end{bmatrix} \Delta t, \quad (5.6)$$

for an MVH frame. As previously noted, the transformation between an MVH frame and an RTN frame, expressed in (3.3), is an identity for circular orbits ( $e = 0$ ). As a result, for near-circular orbits, the equilibrium velocity in an RTN frame can be approximated as

$$\Delta\mathbf{v}_{0(\text{RTN})} \approx \Delta\mathbf{v}_{0(\text{MVH})}. \quad (5.7)$$

Hence, considering a near-circular orbit and assuming that the spacecraft's ballistic coefficient and the atmospheric density remain constant, the equilibrium delta-v can be considered constant in an RTN reference frame. Furthermore, with these assumptions, the equilibrium velocity increment is null in the radial and cross-track directions.

The Taylor series of  $f(\epsilon, \Delta \mathbf{v})$ , at the equilibrium point  $(\epsilon_0, \Delta \mathbf{v}_0)$ , is given by

$$f(\epsilon, \Delta \mathbf{v}) = f(\mathbf{0}, \Delta \mathbf{v}_0) + \left. \frac{\partial f(\epsilon, \Delta \mathbf{v})}{\partial \epsilon} \right|_{\substack{\epsilon_0 \\ \Delta \mathbf{v}_0}} \delta \epsilon + \left. \frac{\partial f(\epsilon, \Delta \mathbf{v})}{\partial (\Delta \mathbf{v})} \right|_{\substack{\epsilon_0 \\ \Delta \mathbf{v}_0}} \delta(\Delta \mathbf{v}) + \dots, \quad (5.8)$$

which can be approximated with the first-order Taylor approximation

$$f(\epsilon, \Delta \mathbf{v}) \approx \left. \frac{\partial f(\epsilon, \Delta \mathbf{v})}{\partial \epsilon} \right|_{\substack{\epsilon_0 \\ \Delta \mathbf{v}_0}} \delta \epsilon + \left. \frac{\partial f(\epsilon, \Delta \mathbf{v})}{\partial (\Delta \mathbf{v})} \right|_{\substack{\epsilon_0 \\ \Delta \mathbf{v}_0}} \delta(\Delta \mathbf{v}). \quad (5.9)$$

Substituting (5.3) in (5.9) results in the linear time-varying system

$$\delta \dot{\epsilon} = \mathbf{A}(\mathbf{k}_R, \Delta \mathbf{v}_0) \delta \epsilon + \mathbf{B}(\mathbf{k}_R) \delta(\Delta \mathbf{v}), \quad (5.10)$$

where

$$\mathbf{A}(\mathbf{k}_R, \Delta \mathbf{v}_0) = \left. \frac{\partial [\mathbf{A}_g(\mathbf{k}_f) + \mathbf{A}_d(\mathbf{k}_f) + \mathbf{B}(\mathbf{k}_f) \Delta \mathbf{v}]}{\partial \epsilon} \right|_{\substack{\epsilon_0 \\ \Delta \mathbf{v}_0}}. \quad (5.11)$$

The derivation of the state matrix  $\mathbf{A}$  of the linearized model (5.10), is shown in detail in Appendix A. The input matrix  $\mathbf{B}$  results directly from (5.2), evaluated at the reference orbit, and is also shown in Appendix A.

### 5.1.1 Open-loop poles

In order to compute the six eigenvalues of the state matrix of the linear time-varying system (5.10), a reference orbit was propagated employing the high-fidelity simulator provided by the TU Delft's Astrodynamics Toolbox (Tudat). The only force acting on a reference orbit is the Earth's gravitational field, which is modeled by the high-fidelity simulator employing the spherical harmonics model discussed in Section 2.3.1, considering coefficients up to degree and order 30. The relevant parameters of the reference orbit and of the spacecraft considered are displayed in Table 5.1 and Table 5.2, respectively. The model's (constant) atmospheric density was extracted from the tabulated U.S. Standard Atmosphere 1976 model, for an altitude of 710 km. The six eigenvalues of the state matrix of the linear time-varying system were computed over ten reference orbits. Three of these eigenvalues remain at the origin, one eigenvalue is real, and the remaining two eigenvalues are complex conjugates. The three time-varying eigenvalues of the state matrix  $\mathbf{A}$  are represented in Figure 5.1<sup>1</sup>. It can be noted that these eigenvalues remain nearly constant for the time studied. Still, all the orbital parameters of the reference orbit change over time and, as such, neither the state matrix  $\mathbf{A}$  nor the input matrix  $\mathbf{B}$  is time-invariant [16].

Table 5.1: Initial state of the reference orbit. Retrieved from [77].

| Mean O.E. | $a$ (km) | $e_x$   | $e_y$  | $i$ (deg) | $\Omega$ (deg) | $u$ (deg) |
|-----------|----------|---------|--------|-----------|----------------|-----------|
|           | 7087.297 | 0.00067 | 0.0013 | 98.1877   | 189.8914       | 0         |

<sup>1</sup>Henceforth, the "number of orbits completed" utilized in figures refers to the division between the time of the simulation and the period of a reference orbit.

Table 5.2: Main parameters of the MANGO spacecraft. Retrieved from [77].

| Spacecraft Model | Value              |
|------------------|--------------------|
| Mass             | 154.4 kg           |
| Drag area        | 1.3 m <sup>2</sup> |
| Drag coefficient | 2.5                |

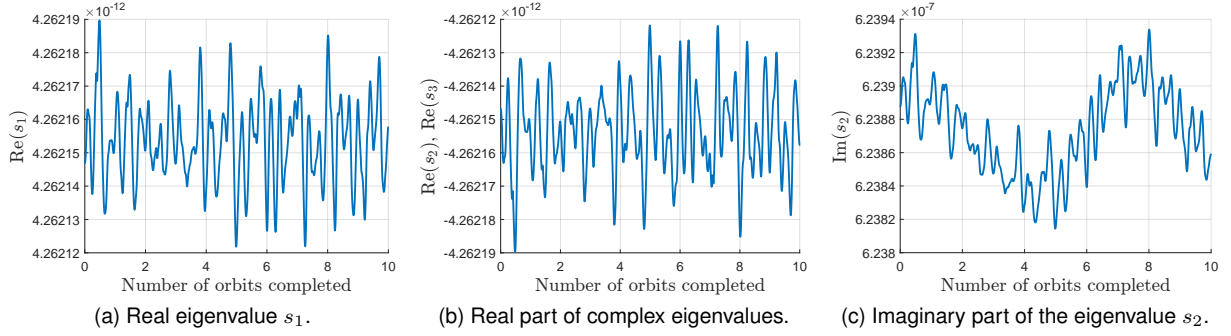


Figure 5.1: Evolution of the non-null eigenvalues of the time-varying state matrix over 10 orbits.

## 5.2 Periodic approximation

The effect of the  $J_2$  coefficient in the reference orbit causes the precession of the ascending node and the argument of perigee. However, the ascending node is not a parameter included in the model, and the precession of the argument of perigee can be disregarded, as this parameter only appears in the model in the form of  $e_x$  and  $e_y$ , which can be taken as approximately null for near-circular orbits. Even if this was not the case, it could still be considered that these secular changes are slow in comparison to the change in the argument of latitude. Equation (3.10) notes that the mean effect of the  $J_2$  coefficient on an orbit's semi-major axis, eccentricity, and inclination is null. Since the second term of the Earth's gravitational potential is around 400 times larger than the following terms, this is a good indication that the effect of the Earth's gravitational potential on these elements is small. Finally, the argument of latitude is only included in the linearized model as  $\sin u_R$  and  $\cos u_R$ , which results in a periodic variation (with a period of approximately one orbit). Given the relatively small secular changes of the slow orbital elements included in the model, and the approximately periodic change of the argument of latitude, this section aims to approximate the linear time-varying model (5.10) with a linear periodic model, composed by a time-invariant state matrix and a periodic input matrix, with a period of one reference orbit.

### 5.2.1 Time-invariant state matrix

In order to derive an approximation for the state matrix, note that the average of  $\sin u_R$  and  $\cos u_R$  over an orbit is approximately null (since  $\dot{v}_R \gg \dot{\omega}_R$ , so  $\dot{u}_R \approx \dot{v}_R$ ). Moreover, the terms that depend on  $\sin u_R$  and  $\cos u_R$ , in the state matrix  $\mathbf{A}$ , arise from the Jacobian of the matrices  $\mathbf{A}_d$  and  $\mathbf{B}\Delta\mathbf{v}$  and are (generally) orders of magnitude smaller than the terms arising from the Jacobian of  $\mathbf{A}_g$ , which do not depend on the reference argument of latitude  $u_R$ . For near-circular orbits, both the components

of the eccentricity vector remain approximately null. As a result, neglect the terms that depend on the argument of latitude and consider

$$e_R \approx 0, \quad a_R \approx a_{R_0}, \quad i_R \approx i_{R_0}, \quad \text{and} \quad n_{R_0} := \sqrt{\mu_{\oplus}/a_{R_0}^3}, \quad (5.12)$$

where the terms  $a_{R_0}$  and  $i_{R_0}$  are obtained from the average of  $a_R$  and  $i_R$  over the first reference orbit, propagated in advance. Furthermore, neglect the term  $a_{g64}$  of the time-varying state matrix  $\mathbf{A}$  (see Appendix A), in order to write the argument of latitude as an integrator of the semi-major axis (as discussed in [11]). Employing the proposed approximations, the state matrix  $\mathbf{A}$  can be approximated as the time-invariant matrix

$$\mathbf{A}_I = \left[ \begin{array}{ccc|ccc} a_{11} & 0 & 0 & 0 & 0 & 0 \\ 0 & a_{22} & a_{23} & 0 & 0 & 0 \\ 0 & a_{32} & a_{33} & 0 & 0 & 0 \\ \hline 0 & 0 & 0 & 0 & 0 & 0 \\ a_{51} & 0 & 0 & a_{54} & 0 & 0 \\ a_{61} & 0 & 0 & 0 & 0 & 0 \end{array} \right], \quad (5.13)$$

where

$$\begin{aligned} B^* &= \frac{A}{m} C_d, & C^* &= -\frac{3}{4} \left( \frac{R_{\oplus}}{a_{R_0}} \right)^2 n_{R_0} J_2, \\ a_{11} &= B^* \rho \sqrt{\frac{\mu_{\oplus}}{a_{R_0}}}, & a_{22} &= -B^* \rho \sqrt{\frac{\mu_{\oplus}}{a_{R_0}}}, \\ a_{23} &= C^* (5 \cos^2 i_{R_0} - 1), & a_{32} &= -a_{23}, \\ a_{33} &= a_{22}, & a_{51} &= \frac{7}{a_R} C^* \cos i_{R_0}, \\ a_{54} &= 2C^* \sin i_{R_0}, & a_{61} &= \frac{7}{2} C^* [5 \cos^2 i_{R_0} - 1 + (3 \cos^2 i_{R_0} - 1)] - 3n_{R_0}. \end{aligned}$$

The time-invariant state matrix  $\mathbf{A}_I$  is lower triangular by blocks. Therefore, the open-loop poles of the periodic system are simply the eigenvalues of the diagonal blocks of  $\mathbf{A}_I$  [76], given by

$$\begin{aligned} s_1 &= a_{11} = B^* \rho \sqrt{\frac{\mu_{\oplus}}{a_{R_0}}}, \\ s_2, s_3 &= a_{22} \pm a_{23} j = -B^* \rho \sqrt{\frac{\mu_{\oplus}}{a_{R_0}}} \pm C^* (5 \cos^2 i_{R_0} - 1) j, \\ s_4 &= s_5 = s_6 = 0. \end{aligned} \quad (5.14)$$

The eigenvalues of the time-invariant state matrix  $\mathbf{A}_I$  (i.e. the open-loop poles of the time-periodic system) are represented in Figure 5.2, alongside the eigenvalues of the time-varying state matrix  $\mathbf{A}$  (i.e. the set of open-loop poles of the time-varying system). It can be noted that the time-invariant poles take similar values to the set of eigenvalues of the time-varying matrix  $\mathbf{A}$ .

Alternatively, the state matrix can be approximated as a periodic matrix, by keeping the terms which depend on  $\sin u_R$  and  $\cos u_R$ . However, this approximation does not significantly improve the accuracy of the linear periodic model, in comparison to considering the time-invariant matrix of (5.13). Employing a time-invariant state matrix instead of a periodic state matrix simplifies the model, leads to an easier

discretization of the system, and allows for a simpler and more efficient implementation of the algorithm proposed in Chapter 4, as the augmented matrices can be computed more efficiently.

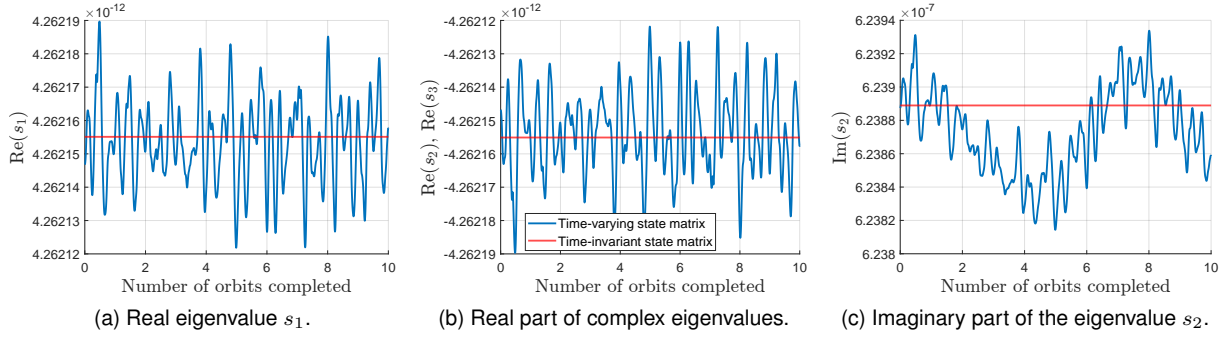


Figure 5.2: Evolution of the eigenvalues of the non-periodic and the periodic state matrices.

## 5.2.2 Periodic input matrix

To construct an accurate input matrix, the terms depending on the argument of latitude must be considered. Therefore, considering solely the approximations of (5.12), the input matrix  $\mathbf{B}(\mathbf{k}_R)$  of the linear time-varying system (5.10), can be approximated by

$$\mathbf{B}_{\text{per}}(\mathbf{k}_R) = \frac{1}{n_{R_0} \Delta t} \begin{bmatrix} 0 & 2a_{R_0} & 0 \\ \sin u_R & 2 \cos u_R & 0 \\ -\cos u_R & 2 \sin u_R & 0 \\ 0 & 0 & \cos u_R \\ 0 & 0 & \sin u_R \\ -2 & 0 & -\sin u_R / \tan i_{R_0} \end{bmatrix}, \quad (5.15)$$

for the first reference orbit, and considered periodic with the period of a reference orbit thereafter.

Finally, the linear time-varying system (5.10) can be approximately written as the linear time-periodic system

$$\delta \dot{\epsilon} = \mathbf{A}_I \delta \epsilon + \mathbf{B}_{\text{per}}(\mathbf{k}_R) \delta(\Delta \mathbf{v}_2). \quad (5.16)$$

As discussed in Chapter 3, for the LQR design, it will be considered that the satellite does not have thrusters aligned with the radial axis, such that only actuation in the along-track and cross-track directions can be applied. Since the equilibrium delta-v is also null in the radial direction (for near-circular orbits), the system (5.16) can be written considering actuation solely in the along-track and cross-track actuation, as

$$\delta \dot{\epsilon} = \mathbf{A}_I \delta \epsilon + \mathbf{B}_{\text{per}_2}(\mathbf{k}_R) \delta(\Delta \mathbf{v}_2), \quad (5.17)$$

where  $\mathbf{B}_{\text{per}_2}$  is comprised by the two last columns of  $\mathbf{B}_{\text{per}}$  and  $\delta(\Delta \mathbf{v}_2) = \delta \left( [\Delta v_T \ \Delta v_N]^T \right)$  is the input vector in the along-track and cross-track directions. For this problem, with an assumption of a near-circular orbit and no radial actuation, the periodic systems (5.16) and (5.17) are equivalent.

### 5.2.3 Discrete-time linear periodic system

The linear system (5.17) can be discretized, assuming zero-order hold for the input  $\delta(\Delta \mathbf{v}_2)$  and a suitable time step (generally a time step of about 10 to 20 seconds yields good results), leading to

$$\delta \epsilon_{l+1} = \mathbf{A}_l \delta \epsilon_l + \mathbf{B}_l \delta(\Delta \mathbf{v}_2)_l, \text{ where } \begin{cases} \mathbf{A}_l = e^{\mathbf{A}_1 \tau_s}, \text{ and} \\ \mathbf{B}_l \approx \left( \int_{\tau=0}^{\tau_s} e^{\mathbf{A}_1 \tau} d\tau \right) \mathbf{B}_{\text{per}_2}(\mathbf{k}_R) \Big|_{l\tau_s} \end{cases} \quad (5.18)$$

are the discretized state-space matrices, and  $\tau_s = \Delta t$  is the sample time. It was considered that the sample time is small enough so that the input matrix does not vary significantly between consecutive samples (i.e. the change in the argument of latitude of the reference orbit over the sample time is small). For the discrete-time linear periodic system, the state matrix  $\mathbf{A}_l = \mathbf{A}_{l+1}$  is time-invariant, and the input matrix  $\mathbf{B}_l = \mathbf{B}_{l+p}$  is periodic with period  $p$ . The LTI system equivalent to (5.18), that likewise considers null actuation in the radial direction, can be written as

$$\bar{\epsilon}_{k+1} = \bar{\mathbf{A}} \bar{\epsilon}_k + \bar{\mathbf{B}} \overline{\delta(\Delta \mathbf{v}_2)}_k, \quad (5.19)$$

where  $\bar{\epsilon} \in \mathbb{R}^{6p}$  is the augmented state,  $\overline{\delta(\Delta \mathbf{v}_2)} \in \mathbb{R}^{2p}$  is the augmented input (in the along-track and cross-track directions), and  $\bar{\mathbf{A}} \in \mathbb{R}^{6p \times 6p}$  and  $\bar{\mathbf{B}} \in \mathbb{R}^{6p \times 2p}$  are the augmented time-invariant matrices, as defined in Chapter 4. It can be noted that considering only along-track and cross-track actuation leads to a substantial reduction in the dimension of the augmented time-invariant system. Nonetheless, it is evident that an LTI system with actuation in the radial direction can be derived if necessary, following a similar procedure. Such an LTI system would be equivalent to the discretization of the system (5.16).

## 5.3 Model validation

In order to validate the developed discrete-time linear periodic model, consider the three following systems, which represent the dynamics of the relative orbital element vector  $\epsilon$ : 1) Nonlinear system (5.3), 2) Linear time-varying system (5.10), and 3) Discrete-time linear periodic system (5.18), equivalent to the LTI system (5.19). A discretization time step of  $\Delta t = 10$  s was considered. The atmospheric density of the models was chosen as the average atmospheric density over the first reference orbit's path, employing the NRLMSISE-00 atmospheric model. The main parameters of the orbit and of the spacecraft are represented in Table 5.1 and Table 5.2, respectively.

The motion of the spacecraft was initially propagated in the case of free fall (no actuation) with the three models. The results are shown in Figure 5.3. The semi-major axis of the spacecraft's orbit decreases linearly, since the three models assume constant atmospheric drag and ballistic coefficient. As expected, both of the eccentricity parameters have a periodic variation, with a much smaller secular component. The periodic variation is caused by the effect of drag, and has a period of one orbit, since it is modelled as a function of the argument of latitude. The inclination is modelled as constant, as neither of the modelled perturbations have a significant secular effect on this orbital element. The tracking error

of the reference argument of latitude ( $\delta u$ ) is an integrator of the tracking error of the reference semi-major axis ( $\delta a$ ).

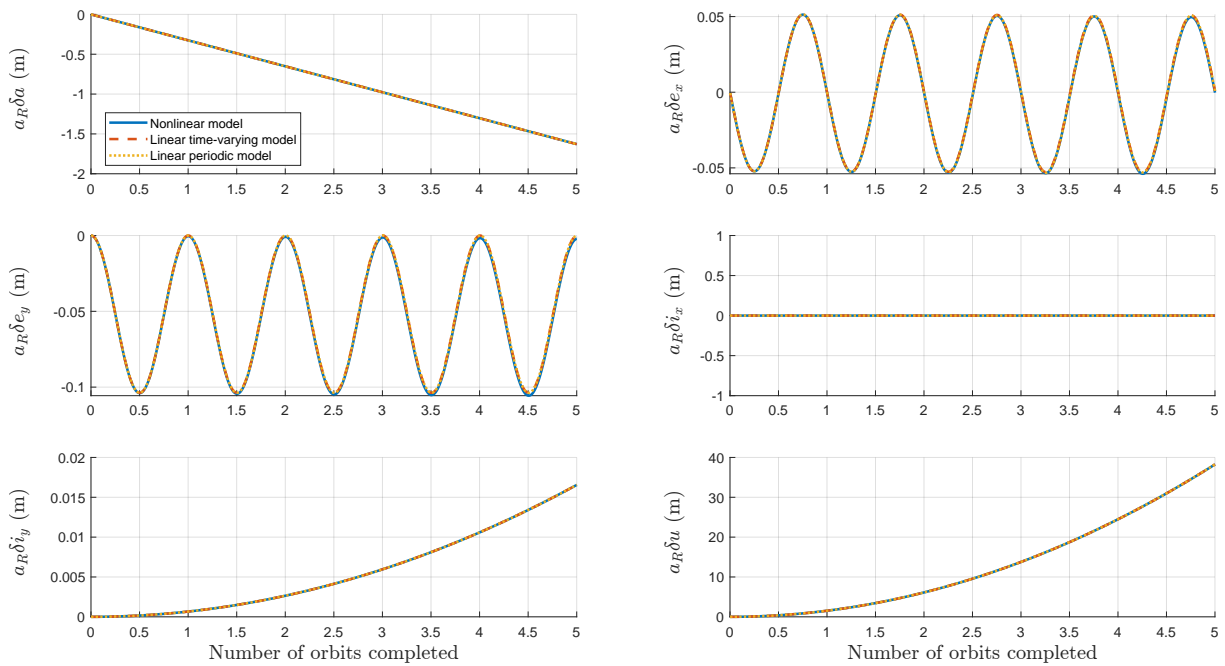


Figure 5.3: Evolution of the relative orbital element vector for a spacecraft in free fall.

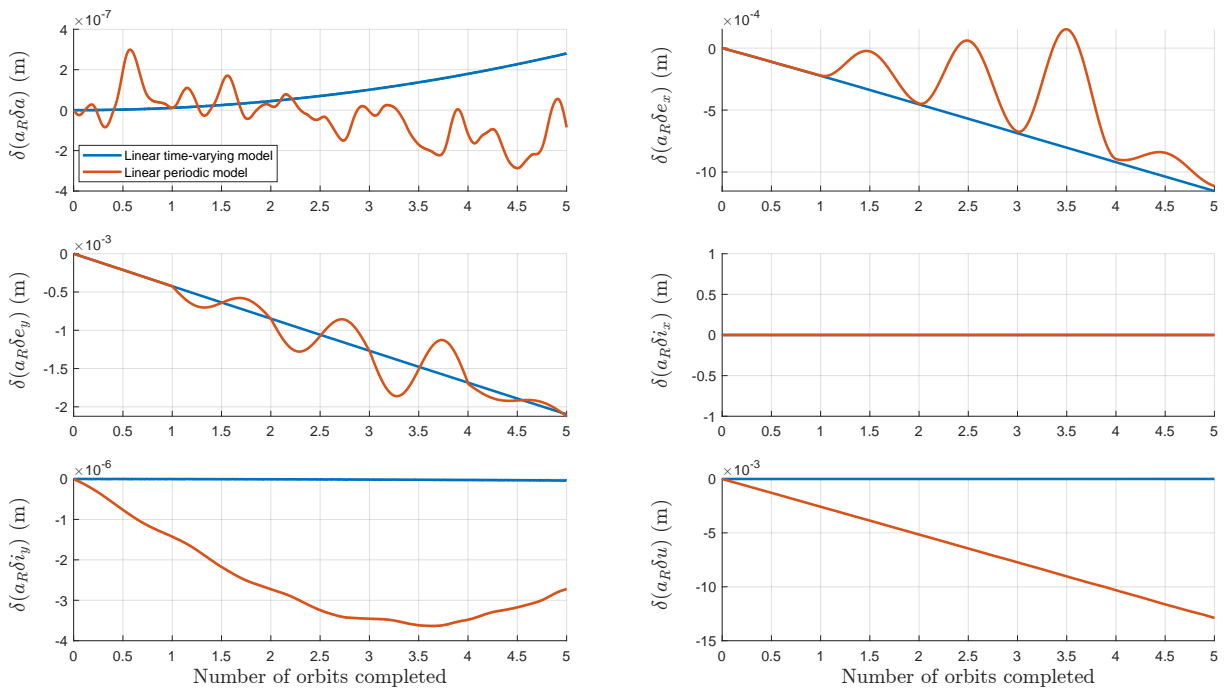


Figure 5.4: Difference between the results of the nonlinear model and the linear models (free fall).

The difference between the results from the orbit propagation with the nonlinear model and the two linear models is represented in Figure 5.4. For every relative orbital element difference, the error of the linear models is several orders of magnitude smaller than the value of the parameter. The largest relative error for both linear models is in the propagation of  $\delta e_x$  and  $\delta e_y$ . Still, the absolute error in the

propagation of these parameters is two orders of magnitude smaller than the amplitude of the periodic variations of the respective parameters, for the first two orbits. Generally, the linear periodic model presents a larger error than the linear time-varying (non-periodic) model. This is the case, particularly, for the propagation of the argument of latitude. Still, for this parameter, the error of the linear periodic model is around four orders of magnitude smaller than the value of the parameter  $\delta u$ . Note that while no actuation was applied, these results show that the periodic input matrix approximates accurately the effects of along-track maneuvers, since in free fall  $\delta(\Delta \mathbf{v}) = -\Delta \mathbf{v}_0 \neq \mathbf{0}$ .

In a second validation study, the motion of the spacecraft was propagated considering constant actuation in the along-track and cross-track directions, chosen as  $\Delta v_T = 5 \cdot 10^{-7}$  m/s and  $\Delta v_N = 10^{-7}$  m/s, respectively (with  $\Delta t = 10$  s). The difference between the results of the nonlinear model and the linear models is shown in Figure 5.5. The conclusions are similar to the case of free fall. The largest relative error is in the propagation of the eccentricity parameters. The error of the linear periodic system is generally larger than the error of the linear time-varying system, particularly for the propagation of the argument of latitude. However, this error still remains three orders of magnitude smaller than the value of  $\delta u$ . Due to the cross-track actuation, there is also a small error introduced in the propagation of the out-of-plane parameters  $\delta i_x$  and  $\delta i_y$ .

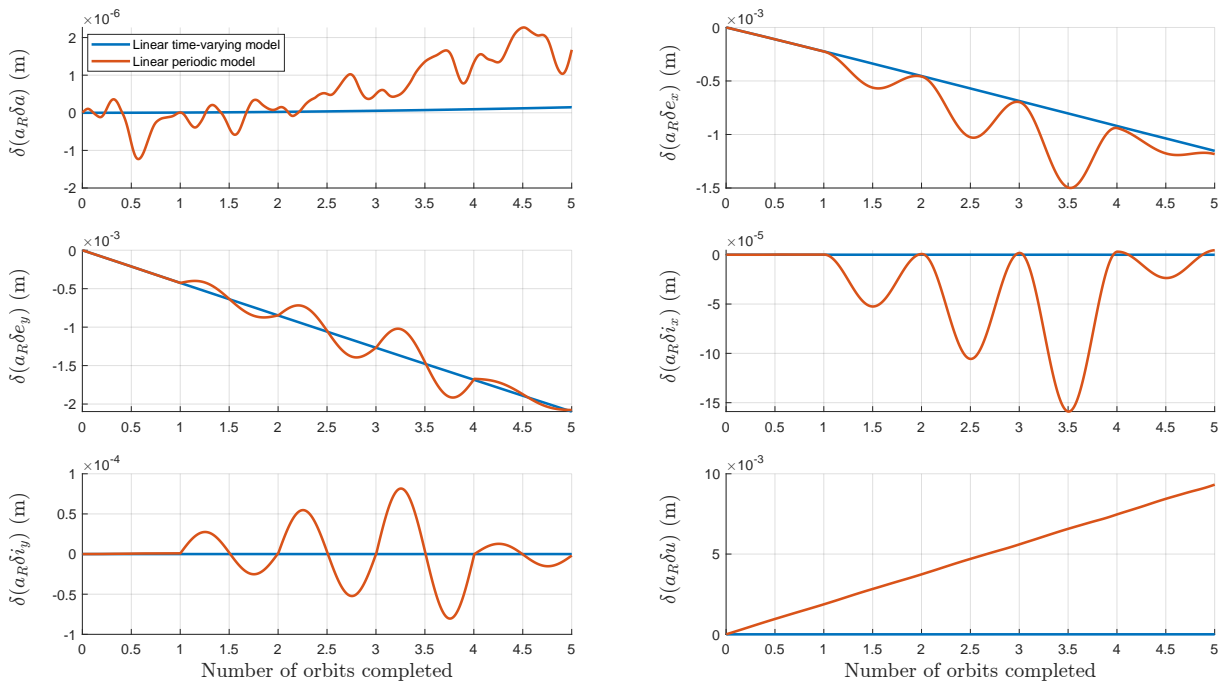


Figure 5.5: Difference between the results of the nonlinear model and the linear models (with constant actuation).

In conclusion, the nonlinear time-varying model (5.3) can be well approximated by the discrete-time linear periodic system (5.18) and, thus, by the equivalent LTI system (5.19), for the case of a spacecraft in free fall and for the case of a maneuvering spacecraft.

### 5.3.1 Validation with a high-fidelity simulator

In this section, the results obtained by the discrete-time periodic model are compared with the true motion of the spacecraft, obtained with a high-fidelity simulator (Tudat). The propagation parameters utilized for the high-fidelity simulator are presented in Table 5.3. In order to simulate the error between the reference orbit propagated on-board the spacecraft and the real gravitational field of the Earth, the real Earth's gravitational field was propagated with a spherical harmonics model of higher degree and order than the gravitational field considered for the propagation of the reference orbit.

Table 5.3: Propagation parameters and perturbations considered by the high-fidelity simulator.

| Spacecraft Model            | Value   |
|-----------------------------|---|
| Mass                        | 154.4 kg                                      |
| Drag area                   | 1.3 m <sup>2</sup>                            |
| Drag coefficient            | 2.5   |
| SRP Coefficient             | 1.3   |
| SRP Effective Area          | 1.3 m <sup>2</sup>                            |
| Orbit propagation           | Model   |
| RO Earth gravity field      | Spherical harmonics (30)                      |
| Earth gravity field         | Spherical harmonics (35)                      |
| Third-bodies gravity fields | Point-mass (Sun, Moon, Mars, Venus, Jupiter)  |
| Atmospheric density         | NRLMSISE-00                                   |
| Solar radiation pressure    | Cannonball model (w/ Earth as occulting body) |
| Relativistic corrections    | Schwarzschild metric                          |
| Numerical method            | RK45  |

The evolution of the relative orbital element vector, for the case of a spacecraft in free fall, is presented in Figure 5.6 for the linear periodic system and the high-fidelity simulator, over 5 orbits.

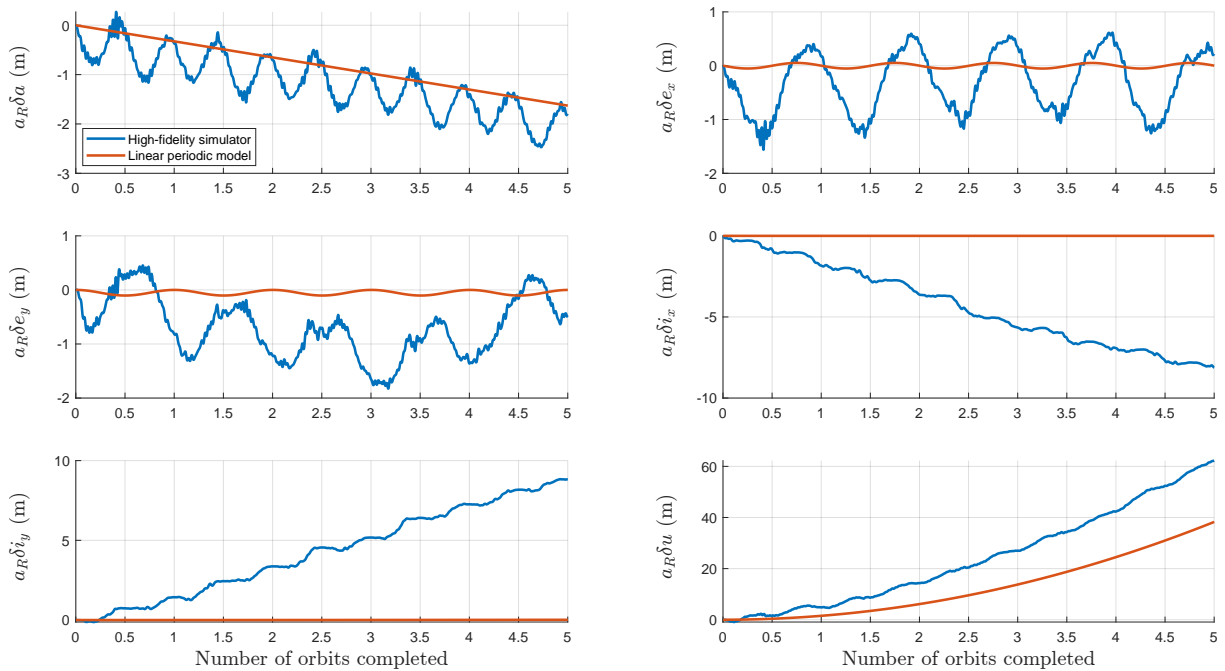


Figure 5.6: Evolution of the relative orbital element vector for a spacecraft in free fall.

The difference between the results of the high-fidelity simulator and the linear periodic model is presented in Figure 5.7. Observing Figure 5.6, it can be noted that the deviation of the true orbit's semi-major axis, obtained by the high-fidelity simulator, has a periodic component that the linear periodic model does not include. However, observing Figure 5.7, it can be noted that the error of the linear model in the estimate of the semi-major axis is close to null every half orbit. Therefore, it can be concluded that while there is a periodic effect that is not included in the model, the secular variation of the semi-major axis is modelled accurately. These periodic effects cause the relative orbital difference  $\delta a$  to be larger (in magnitude) for the high-fidelity simulator than for the periodic model, for the vast majority of the time. Since  $\delta u$  is essentially an integrator of  $\delta a$ , this results in this parameter increasing more rapidly in reality than the periodic model predicts. The relative orbital element differences  $\delta e_x$  and  $\delta e_y$  also have a small periodic component which is not included in the model. Still, the real secular variation of these variables is slow. In fact, the error for the propagation of  $\delta e_x$  is approximately null after the first orbit. As expected, the model lacks accuracy in the out-of-plane ( $\delta i_x, \delta i_y$ ) motion prediction since neither the third-body perturbations nor the solar radiation pressure (which are the main causes for the perturbation of the out-of-plane motion) are included in the original nonlinear model [16].

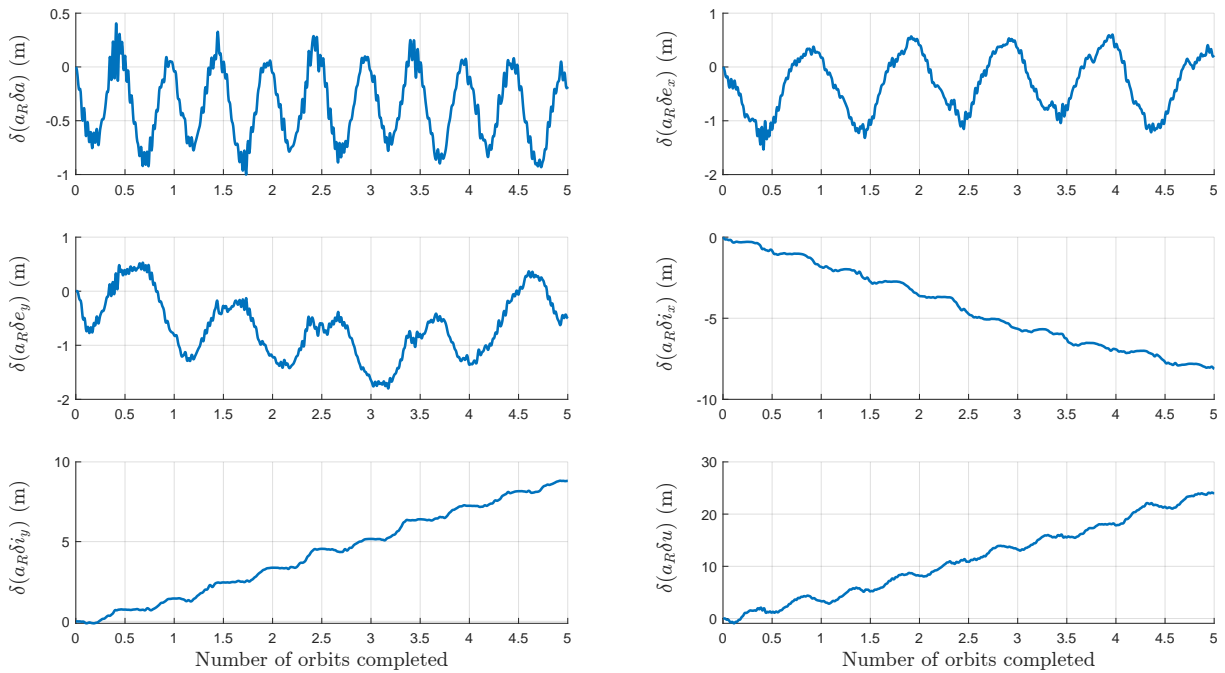


Figure 5.7: Difference between propagation with a high-fidelity simulator and the LTP model (free fall).

The propagation of the semi-major axis and the argument of latitude, over 100 orbits (approximately 7 days) is displayed in Figure 5.8. The observed 10.7-cm Solar Radio Flux and Ap index, which measure solar particle radiation, vary over the week of the simulation and, as a result, the atmospheric drag varies not only over the orbit, but also over time for the same location. Despite this fact, the linear periodic model obtains an accurate estimate of the decrease in the semi-major axis (error of 4% after 100 orbits). Still, for long satellite missions, it will prove beneficial to routinely update the model with a better prediction of the atmospheric density. Moreover, if atmospheric models predict a substantial change in atmospheric density along the spacecraft's path, the model must be updated with a more

recent estimate of the atmospheric density.

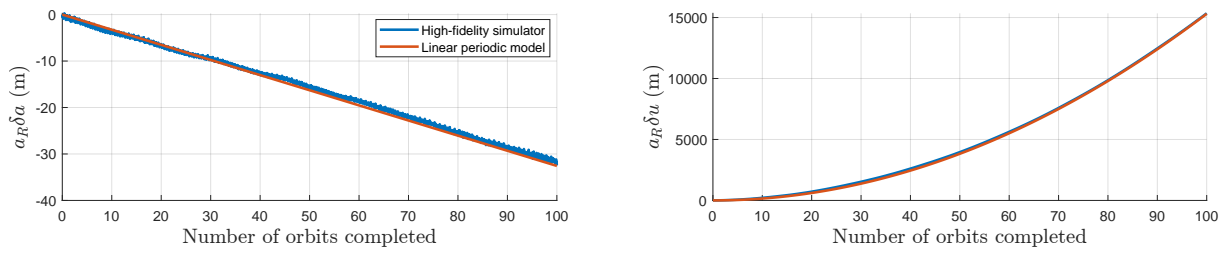


Figure 5.8: Difference between propagation with linear model and high-fidelity simulator (free fall).

The motion of the spacecraft was also propagated with constant actuation in the along-track and cross-track directions, chosen as  $\Delta v_T = 5 \cdot 10^{-7}$  m/s and  $\Delta v_N = 10^{-5}$  m/s, respectively (with  $\Delta t = 10$  s). The error of the LTP model for this scenario is shown in Figure 5.9, alongside the error for the scenario where the spacecraft is in free fall. Since the error for these two scenarios is similar, it can be deduced that the effect of the maneuvers on the spacecraft's orbit is accurately modelled by the linear model (i.e. adding the maneuvers does not introduce a substantial amount of error to the linear system's prediction of the satellite's motion). This is expected, as the input matrix results directly from the Gauss' form of Lagrange's planetary equations, and the assumption of a near-circular orbit.

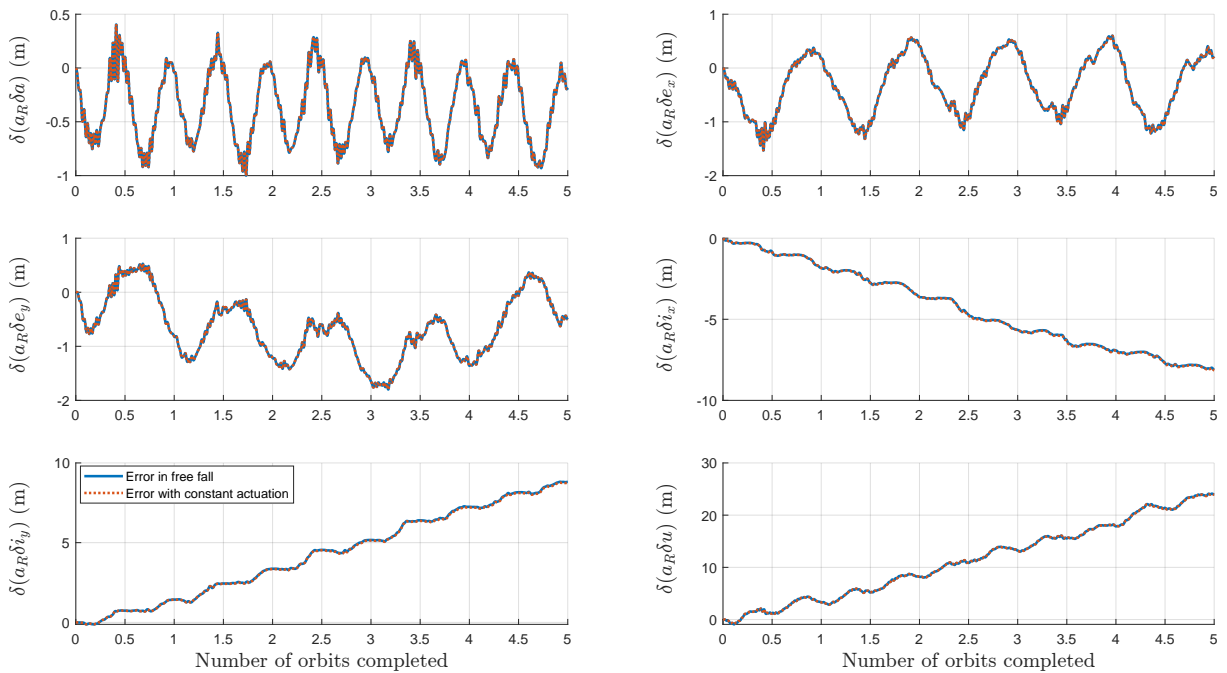


Figure 5.9: Difference between propagation with a high-fidelity simulator and the LTP model.

### 5.3.2 Effect of the Earth's gravitational field and the atmospheric drag

This section aims to determine if the differences between the linear periodic model and the high-fidelity simulator are due to the model failing to represent the perturbations that are considered (drag and the Earth's gravitational field), or due to the effect of other (unmodelled) perturbations. With this goal, consider Figure 5.10, where the results of the linear periodic model are displayed alongside the

results of the high-fidelity simulator, considering only the atmospheric drag and the Earth's gravitational field. In this case, the results obtained by the periodic model more closely resemble the results of the high-fidelity propagator. There still exists a small periodic variation on the orbit's semi-major axis for the high-fidelity simulator (caused by the change in the atmospheric density along the spacecraft's path) that the LTP model does not capture. However, the amplitude of this variation is much smaller than in the previous section, where other perturbations were considered, causing the propagation of the argument of latitude by the LTP model to be more accurate in this case. The main difference is noted in the orbital element differences  $\delta e_x$  and  $\delta e_y$ , which have a slow secular change that the model does not predict. This is likely because of the assumption of constant atmospheric density. The high-fidelity simulator also shows a secular change in the orbit's inclination. However, this secular change is around 300 times smaller (after 5 orbits) than when other perturbations are included. The error of the LTP model in the estimate of  $\delta i_y$  is also significantly smaller than when other perturbations are included. As a result, it can be concluded that the lack of accuracy of the model when compared to the propagation using a high-fidelity simulator can be in large part attributed to the fact that the unmodelled perturbations, which were not considered on the original nonlinear model, have noticeable effects on the system.

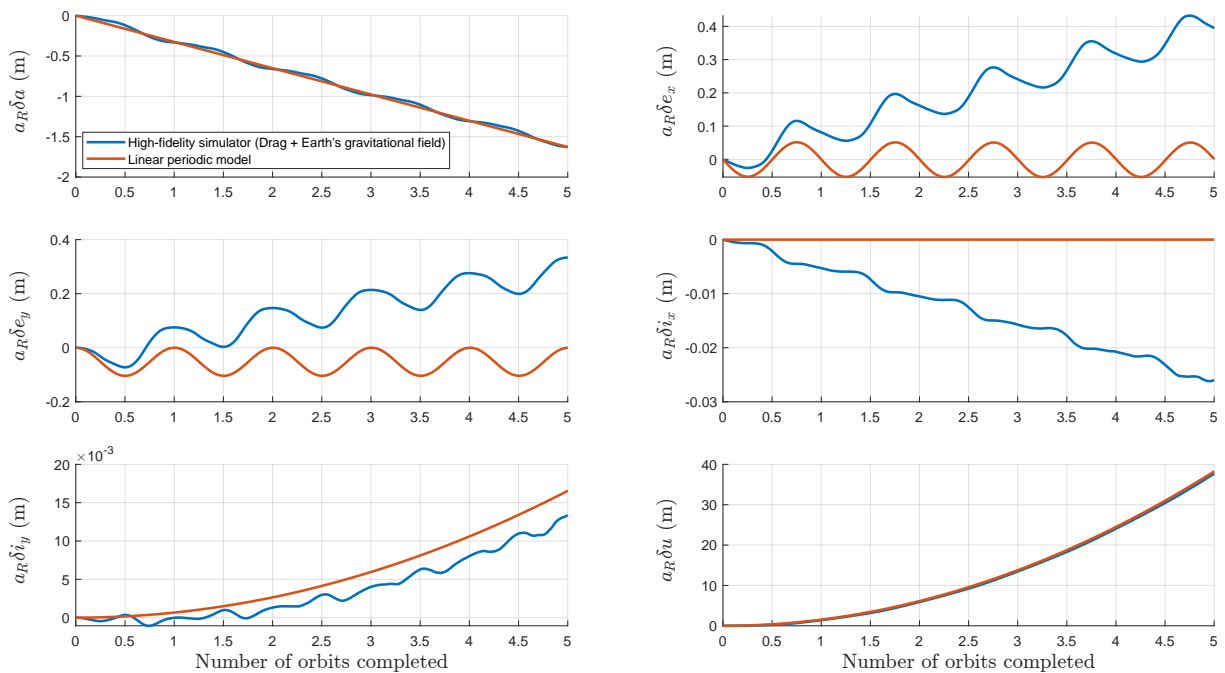


Figure 5.10: Evolution of the relative orbital element vector (considering drag and the Earth's gravitational field).

In conclusion, the discrete-time linear periodic model, and its time-invariant equivalent, allow for accurate short and long term prediction of the secular variation of the semi-major axis, as long as there are no phenomena which significantly alter the atmospheric density during the simulation period. Moreover, the linear periodic system accurately models the effects of orbital maneuvers on the spacecraft's orbit. Periodic changes in  $\delta e_x$  and  $\delta e_y$  are not accurately predicted by the model. On the other hand, these elements have a slow secular change. The estimation of the out-of-plane motion ( $\delta i_x$ ,  $\delta i_y$ ) is the most significant shortcoming of the model, as the secular variations of the inclination and the longitude of the

ascending node are not properly modelled. The shortcomings of the nonlinear and linear models studied are mostly due to the fact that the unmodelled perturbations have relatively large effects on the satellite's orbit. This is particularly true for the out-of-plane motion of the satellite, since none of the perturbations which primarily affect this motion are modelled. As a result, for better prediction of the satellite's motion (especially for the out-of-plane motion), other perturbations must be included in the model. Third-body perturbations, from the Moon and the Sun, have the largest effect besides the perturbations already modelled [78], and including these in the model would allow for better results in the prediction of the out-of-plane motion. Finding a method to include the effects of these perturbations, while maintaining the periodicity of the model, can lead to significant improvements.

For the sake of developing a feedback law, the LTP model developed herein may be utilized. In fact, it was concluded that the LTP model has similar accuracy to the nonlinear and linear time-varying models utilized in the literature, as these also solely model the effect of the atmospheric drag and  $J_2$ . While the effects of perturbations on the out-of-plane motion are not well modelled, the effects of orbital maneuvers on the out-of-plane motion are accurately represented by the periodic input matrix derived, as noted in Section 5.3.1.

Finally, it is important to note that the results are presented for an orbit with an altitude of approximately 700 km. The validity of the model employed rests on the fact that the atmospheric drag and the Earth's gravitational field (up to  $J_2$ ) are the dominant perturbations on the satellite's orbit. As discussed in Chapter 2, and observed in Figure 2.4, this becomes an erroneous assumption as the orbit's height increases, particularly since the atmospheric density decreases exponentially with height. The upper bound of a low Earth orbit is often defined as 2000 km [5]. However, at this altitude, the effect of the atmospheric drag is already less significant than the third-body perturbations caused by the Moon and the Sun [36]. Generally, the models studied in this thesis will perform significantly better when applied to orbits at lower altitudes, even within the height boundary that defines a low Earth orbit.

## Chapter 6

# Controller design and simulation results

In the present chapter, the proposed control system is designed and validated. Section 6.1 outlines the LQR design process. Furthermore, the proposed control solution is validated with ideal sensors and actuators (i.e. no navigation or actuation errors are considered), for the control of all orbital elements. In Section 6.2, it is discussed how the problem can be formulated to fulfill mission requirements provided in terms of Earth-fixed operational parameters (ground-track latitude, longitude, and orbit altitude). The performance of the proposed control solution is compared with the precise impulsive control methodology employed in the PRISMA mission, both with ideal sensors and actuators, and while including on-board navigation errors and realistic actuators. Finally, in Section 6.3, the controller is validated for the correction of initial errors from the orbit injection process.

### 6.1 LQR design and controller validation

Let the linear periodic system (5.17) be discretized considering 300 samples per period (i.e.  $p = 300$ , leading to  $\Delta t \approx 19$  s). The performance of the discrete-time LTP model does not deteriorate significantly due to considering  $\Delta t \approx 19$  s instead of a smaller time step, as the choice of a time step between 10 s and 20 s is well within tolerance for the study of a LEO satellite (see [27, 79]). The choice of the time step was motivated by the fact that a decrease in the number of samples per period leads to a decrease in the computational time of the algorithm proposed in Chapter 4 (or any other algorithm for the solution of the DPRE, for that matter). This is a significant benefit due to the limited CPU capability on-board a satellite. Forming the augmented LTI system, as described in Chapter 4, it can be noted that the pair  $(\bar{\mathbf{A}}, \bar{\mathbf{B}})$  is stabilizable, even though only actuation in the along-track and cross-track directions is considered.

In order to validate the control methodology developed, assume that the main goal of the mission is to keep the relative orbital vector  $\delta\epsilon$  small, in order to achieve accurate reference tracking of all Keplerian elements throughout the entire simulation (e.g. keeping the distance between the true and reference spacecraft below 10 m). With that goal, an LQR problem with relatively inexpensive control will be

considered (in order to attain accurate reference following). Let the matrices  $\mathbf{Q}_l$  and  $\mathbf{R}_l$  be chosen as diagonal and time-invariant, with  $\mathbf{Q}_l = \text{diag}(1.5^2, 2^2, 2^2, 3^2, 3^2, 5^2)^{-1}$  and  $\mathbf{R}_l = \text{diag}(10^{11}/1.225, 8 \cdot 10^8)$ , for all  $l$ . It can be noted that the pair  $(\bar{\mathbf{A}}, \bar{\mathbf{C}})$  is observable. Therefore, the algorithm proposed in Chapter 4 can be applied, resulting in the set of optimal periodic state feedback matrices  $\mathbf{K}_l$  ( $l = 0, \dots, p-1$ )  $\in \mathbb{R}^{2 \times 6}$ . Recall that the relative orbital element vector is  $\delta\epsilon = a_R(\delta a, \delta e_x, \delta e_y, \delta i_x, \delta i_y, \delta u)^T$  and that the optimal feedback law is given by  $\delta(\Delta \mathbf{v}_2)_l = -\mathbf{K}_l \delta\epsilon$ , with  $\mathbf{K}_l = \mathbf{K}_{l+p}$ . Let the entries of the feedback matrices  $\mathbf{K}_l$  be represented as

$$\mathbf{K}_l = \begin{bmatrix} g_{T_1}(l) & g_{T_2}(l) & g_{T_3}(l) & g_{T_4}(l) & g_{T_5}(l) & g_{T_6}(l) \\ g_{N_1}(l) & g_{N_2}(l) & g_{N_3}(l) & g_{N_4}(l) & g_{N_5}(l) & g_{N_6}(l) \end{bmatrix}. \quad (6.1)$$

To perform an initial sanity check of the proposed control system, consider the optimal feedback matrices resultant from the LQR problem defined in this section. The first row of these feedback matrices (which influences the along-track actuation) is displayed in Figure 6.1, over one period. The feedback gains for the states  $\delta i_x$  and  $\delta i_y$  ( $g_{T_4}$  and  $g_{T_5}$ , respectively) are one to three orders of magnitude smaller than the remaining gains. This is the case since  $\delta i_x$  and  $\delta i_y$  are not directly altered by along-track maneuvers, and are also not substantially affected by changes in the other orbital elements. The evolution of  $g_{T_2}$  over the period resembles a cosine wave, whereas  $g_{T_3}$  approximately follows a sine wave (with some offset). This can be explained by the fact that the *efficiency* of an along-track maneuver  $\Delta v_T$  on the orbital parameters  $e_x$  and  $e_y$  is a function of  $\cos u_R$  and  $\sin u_R$ , respectively. The entry  $g_{T_1}$  does not vary substantially over the period, as the effect of an along-track maneuver in the semi-major axis does not depend on the location of the maneuver. While  $\delta u$  cannot be directly controlled by along-track impulses, the entry  $g_{T_6}$  is still large (considering that  $\delta u$  is often the largest error of the system). This is due to the fact that  $\delta u$  is essentially an integrator of  $\delta a$ , and it is more effectively controlled by altering the semi-major axis, rather than applying cross-track maneuvers which directly affect  $\delta u$ .

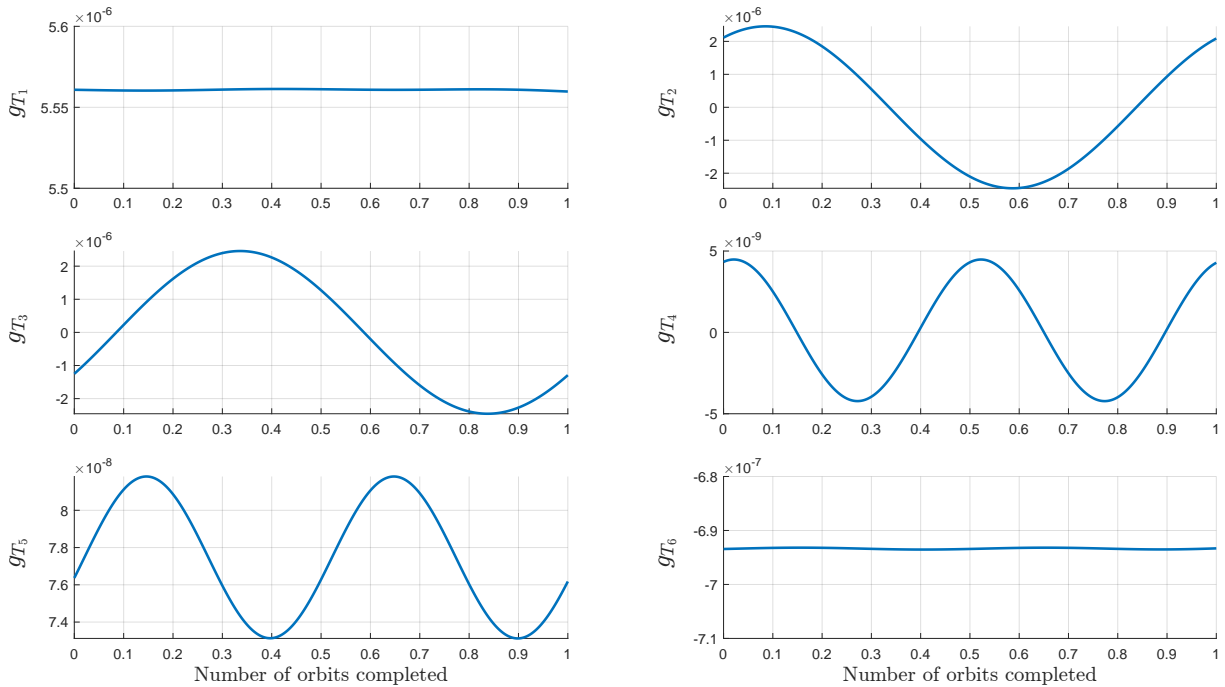


Figure 6.1: Along-track optimal periodic feedback gains over a reference orbit.

The second row of the entries of the periodic feedback matrices is displayed in Figure 6.2. It can be noted that  $g_{N_4}$  and  $g_{N_5}$  are one to three orders of magnitude larger than the remaining entries. Thus, it can be deduced that the along-track maneuvers mostly depend on  $\delta a, \delta e_x, \delta e_y$  and  $\delta u$ , whereas the cross-track maneuvers are mostly a function of  $\delta i_x$  and  $\delta i_y$ . The entry  $g_{N_4}$  approximately follows a cosine wave over the period, whereas the evolution of  $g_{N_5}$  resembles a sine wave. Similarly to the along-track case, this is influenced by the fact that the *efficiency* of a cross-track maneuver  $\Delta v_N$  on the orbital parameters  $i_x$  and  $i_y$  is a function of  $\cos u_R$  and  $\sin u_R$ , respectively. As previously mentioned, a cross-track maneuver also has an effect on the argument of latitude. As a result, the entries  $g_{N_1}$  and  $g_{N_6}$  are only one and two orders of magnitude smaller than  $g_{N_4}$ , respectively. Since the change in the argument of latitude due to a cross-track maneuver depends on  $\sin u_R$ , the evolution of both  $g_{N_1}$  and  $g_{N_6}$  resembles a sine wave. In conclusion, the evolution of the feedback gains over the period (one reference orbit) comply with the orbital mechanics associated with the problem.

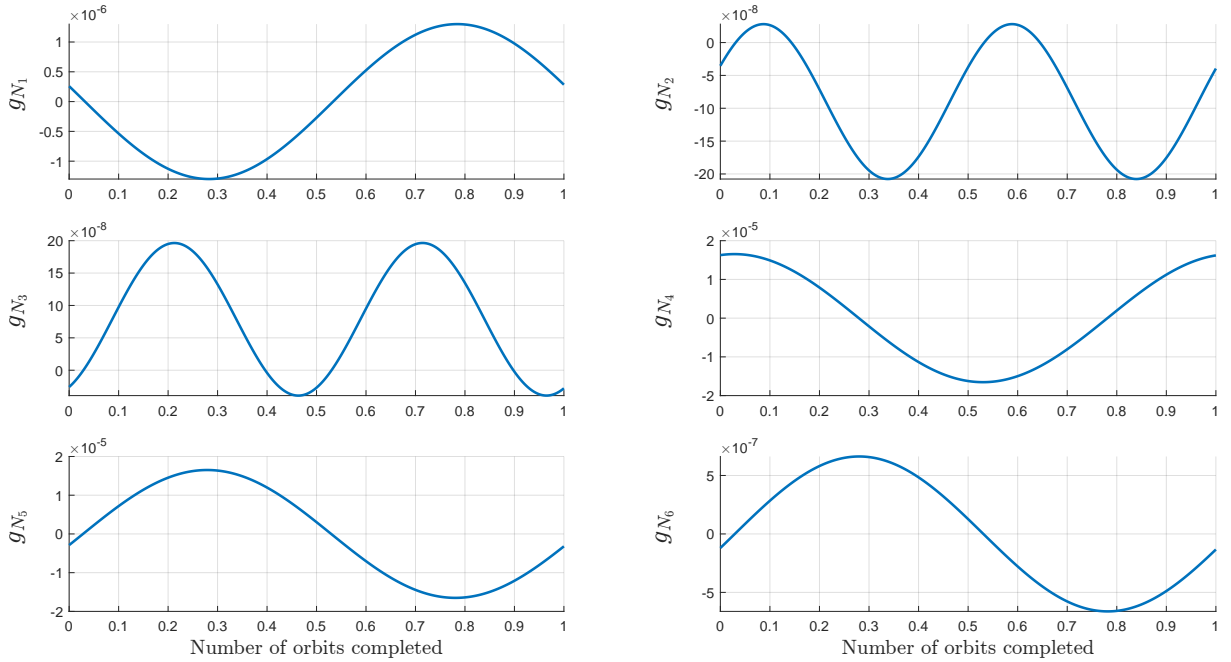


Figure 6.2: Cross-track optimal periodic feedback gains over a reference orbit.

For the simulations conducted in the present chapter, the reference and the true orbits are propagated by a high-fidelity simulator (Tudat). The reference orbit considered is the orbit employed on the PRISMA mission, whose initial state is displayed in Table 5.1. The spacecraft model and the propagation parameters for the high-fidelity simulator are displayed in Table 5.3.

In order to validate the control algorithm proposed, consider that the controller designed in the current section is employed to maintain the orbit of the PRISMA mission, aiming for accurate reference tracking of all Keplerian elements. The high-fidelity simulation of the satellite's motion was conducted over one month (approximately 440 orbits), considering ideal sensors and actuators. The distance between the true and the (virtual) reference spacecraft (averaged over one orbit) is shown in Figure 6.3. Henceforth, this quantity will also be referred to as the distance between the true and the reference orbit. The main results of the simulation are summarized in Table 6.1. The evolution of the relative orbital elements

is displayed in Figure 6.4. It can be noted that the intended precision (10 m) can be achieved. All the relative orbital parameters are kept within a small window of 2 m, except the tracking error of the argument of latitude (multiplied by  $a_R$ ), which is kept within a window of 10 m (i.e. the maximum error for the tracking of the argument of latitude is approximately  $8.1 \cdot 10^{-5}$  degrees).

Table 6.1: Performance and maneuver budget.

| $\delta\epsilon$ | Mean (m)                | $\sigma$ (m) |
|------------------|-------------------------|--------------|
| $a_R\delta a$    | 0.28                    | 0.50         |
| $a_R\delta e_x$  | 0.42                    | 0.72         |
| $a_R\delta e_y$  | -0.10                   | 0.81         |
| $a_R\delta i_x$  | 0.23                    | 0.70         |
| $a_R\delta i_y$  | 0.71                    | 0.37         |
| $a_R\delta u$    | 3.11                    | 3.21         |
| Maneuvers        | Max.                    | Total (m/s)  |
| $\Delta v_T$     | $1.1 \cdot 10^{-5}$ m/s | 0.41         |
| $\Delta v_N$     | $3.8 \cdot 10^{-5}$ m/s | 1.56         |
| $T_T$            | 88 $\mu$ N              | —            |
| $T_N$            | 293 $\mu$ N             | —            |

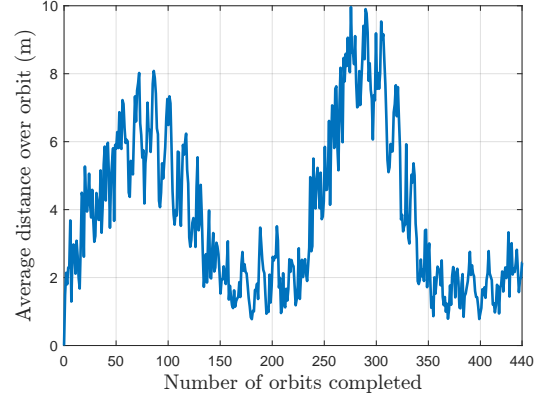


Figure 6.3: Distance between real and virtual spacecraft.

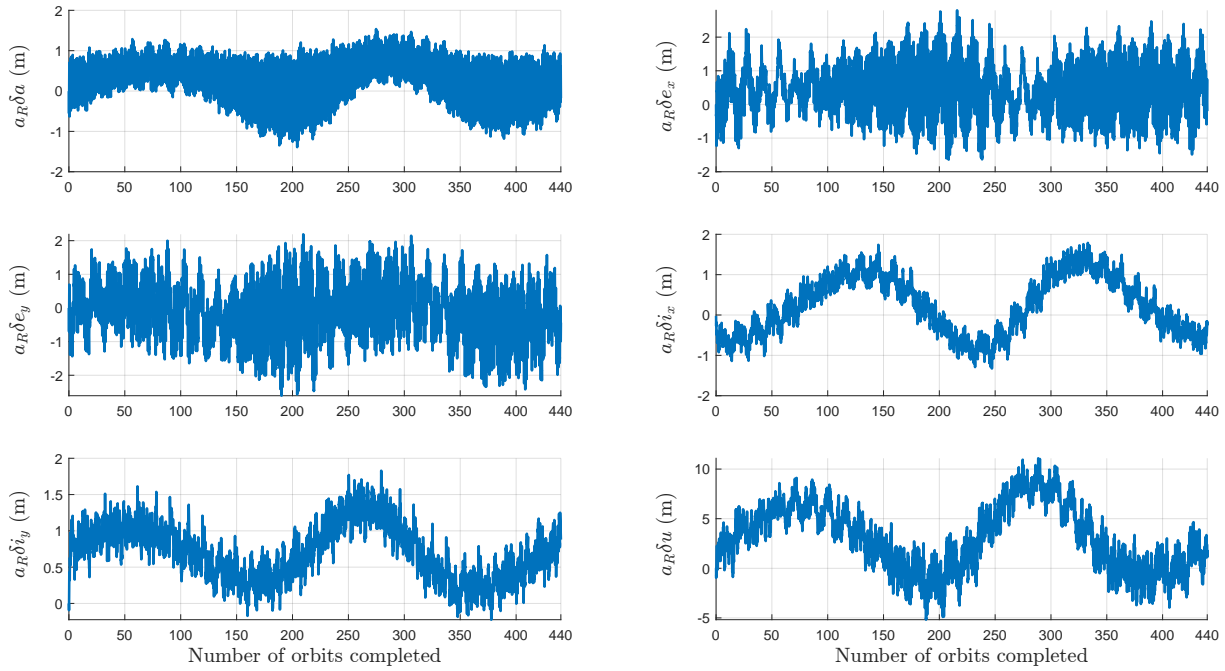


Figure 6.4: Evolution of the relative orbital elements over one month.

The actuation is displayed in Figure 6.5. Henceforth, actuation will be represented in terms of commanded delta-v for the time step (it is assumed that constant thrust is applied over the time step). It can be noted that negative along-track actuation is often applied, in order to keep the values of  $\delta a$ ,  $\delta e_x$ ,  $\delta e_y$  and  $\delta u$  low throughout the entire simulation period. It is important to note that negative along-track actuation adds to the effect that the atmospheric drag has on lowering the orbit, increasing the amount of (positive) change in velocity that will have to eventually be applied, and can therefore be considered inefficient. However, negative along-track actuation is often necessary for missions with strict position

requirements. The maximum commanded thrust is in the order of  $10^2 \mu\text{N}$ . Due to the low maximum thrust required, a very efficient low-thrust propulsion system can be employed, resulting in low fuel consumption despite the relatively large delta-v. The total delta-v required for station-keeping will heavily depend on the mission requirements, and thus is relatively large in this case, as the LQR design aimed for very precise orbit control.

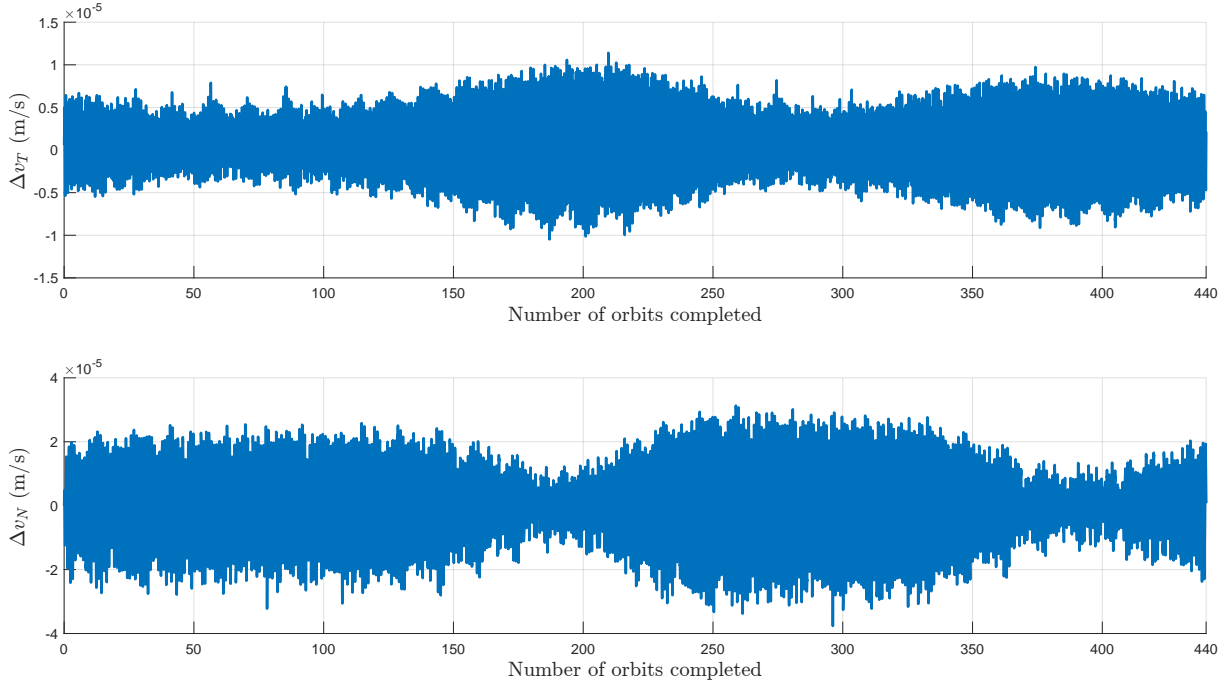


Figure 6.5: Executed maneuvers, in terms of delta-v per time step.

## 6.2 PRISMA mission

In this section, the performance of the proposed control methodology is compared with the impulsive feedback methodology proposed in [16, 80], for the PRISMA mission.

### 6.2.1 Relative Earth-fixed elements

The mission requirements for the PRISMA mission are given in terms of the relative Earth-fixed elements (REFEs). This parameterization is analogous to the relative orbital elements ( $\delta\epsilon$ ) [81, 82] and describes the relative motion of the real and reference subsatellite points on the Earth's surface. Employing the REFE parametrization is often helpful for designing a control system, as mission requirements are usually expressed through Earth-fixed operational parameters [80]. As shown in Figure 6.6, the  $\{\lambda, \varphi, \eta\}$  reference frame has the origin in the subsatellite point considered, and at the altitude of the satellite. The  $\lambda$  (longitude) axis is tangent to the local line of latitude and points east, the  $\varphi$  (latitude) axis is tangent to the local meridian and points north, and the  $\eta$  axis points along the orbit radius. The relative position of the real and reference subsatellite points (on the Earth's surface) is defined in the  $\{\lambda_R, \varphi_R, \eta_R\}$  frame of reference by the phase difference vector  $\delta\mathbf{L} = (\delta L_\lambda, \delta L_\varphi)^T$  and the normalized altitude difference  $\delta h = \Delta h/a_R$  [80]. These parameters are likewise represented in Figure 6.6, and can

be written as a function of the relative orbital elements ( $\delta\epsilon$ ) as

$$\frac{\delta L_\lambda}{a_R} = \frac{1}{\sin i_R} (-\delta i_x \sin u + \delta i_y \cos u) + \frac{|\omega_\oplus - \dot{\Omega}_R|}{n} \sqrt{1 - (\sin u \sin i)^2} \left( \frac{\cos i_R}{\sin i_R} \right) [\delta i_x \sin u + \delta i_y (1 - \cos u)] + \frac{|\omega_\oplus - \dot{\Omega}_R|}{n} \sqrt{1 - (\sin u \sin i)^2} \left[ \delta u - \frac{3}{2} u \delta a + 2(\delta e_x \sin u - \delta e_y \cos u) \right], \quad (6.2)$$

$$\frac{\delta L_\varphi}{a_R} = \cos i_R [\delta i_x \sin u + \delta i_y (1 - \cos u)] + \sin i_R \left[ \delta u - \frac{3}{2} u \delta a + 2(\delta e_x \sin u - \delta e_y \cos u) \right], \quad \text{and} \quad (6.3)$$

$$\frac{\delta h}{a_R} = \delta a - (\delta e_x \cos u + \delta e_y \sin u), \quad (6.4)$$

for near-circular orbits, assuming that the separation between the reference and real orbits is small in comparison to the radius of the reference orbit [16].

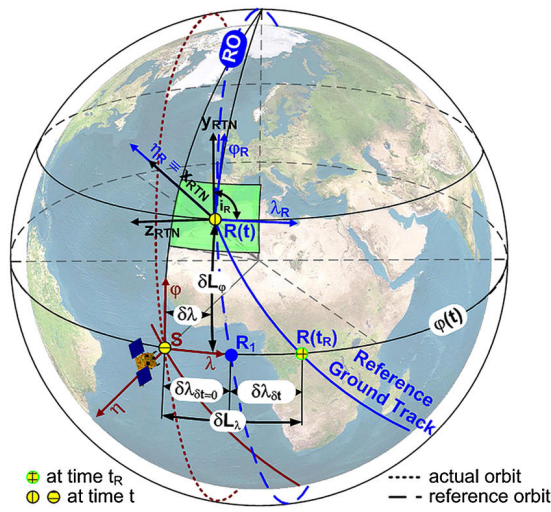


Figure 6.6: Geometry of the relative Earth-fixed elements. Retrieved from [80].

This section will consider one of the cases studied in [16, 80], where the system design aims to control the relative Earth-fixed elements  $\delta L_\lambda$  and  $\delta L_\varphi$  at the ascending node, by means of along-track and cross-track maneuvers. These relative Earth-fixed parameters are commonly used as operational parameters for orbit maintenance [80]. At the ascending node, (6.2)-(6.4), and the rate of change of the difference in ground-track longitude  $d(\delta L_\lambda)/dt$ , can be written as

$$\begin{aligned} \left. \delta L_\lambda \right|_{u=0} &= c_1 (\delta i_y a_R) + c_2 (a_R \delta u - 2a_R \delta e_y), \\ \left. \frac{d(\delta L_\lambda)}{dt} \right|_{u=0} &\approx c_3 a_R \delta a, \\ \left. \delta L_\varphi \right|_{u=0} &= \sin i_R (a_R \delta u - 2a_R \delta e_y), \quad \text{and} \\ \left. \delta h \right|_{u=0} &= a_R (\delta a - \delta e_x), \end{aligned} \quad (6.5)$$

where  $c_1 = 1/\sin i_R$ ,  $c_2 = |\omega_\oplus - \dot{\Omega}_R|/n$ , and  $c_3 = a_{r1}/\sin i_R + a_{r2}c_2$  (with  $a_{r1}$  and  $a_{r2}$  corresponding to the entries  $a_{51}$  and  $a_{61}$  of the state matrix  $\mathbf{A}$ ) [80]. The impulsive control methodology proposed in [16], and further developed in [80], is summarized in the following section.

## 6.2.2 PRISMA's linear feedback methodology

The linear control system of [16, 80] was designed by means of pole placement, employing a simplified model (which considers only the state parameters  $a$ ,  $i_y$ , and  $u$ ) and separating the problems of in-plane and out-of-plane control. Studying (6.5) it can be noted that, at the ascending node,  $\delta L_\lambda = k_1 \delta i_y + k_2 L_\varphi$ , where  $k_1, k_2 \in \mathbb{R}$ . Therefore, the only solution to control both  $\delta L_\lambda$  and  $\delta L_\varphi$  is to select  $\delta i_y$  as one of the control outputs. As a result, three outputs ( $\delta L_\lambda, \delta L_\varphi, \delta i_y$ ) and two inputs ( $\Delta v_T, \Delta v_N$ ) are considered.

The impulsive control scheme computes along-track maneuvers at the ascending node every 6 hours (four orbital periods) and cross-track maneuvers every 12 hours (eight orbital periods). The along-track impulsive maneuvers are scheduled to be executed at

$$u_{R_T} = \arctan\left(\frac{\delta e_y}{\delta e_x}\right) + k\pi, \text{ where } \begin{cases} k = 0 & \text{if } \delta e_x \Delta v_T < 0, \\ k = 1 & \text{if } \delta e_x \Delta v_T > 0, \end{cases} \quad (6.6)$$

and the cross-track maneuvers are scheduled to be executed at  $u_{R_N} = \pi/2$ , to maximize their effectiveness on altering  $\delta i_y$ . The analytical rule (6.6), to select the location of the along-track maneuvers, is an ingenious solution to controlling the eccentricity vector, employing only (at most) one maneuver per orbit. Recall that the rate of change of  $\delta e_x$  and  $\delta e_y$ , caused by an along-track maneuver, can be written as

$$\delta \dot{e}_x = \frac{\Delta v_T}{n_R \Delta t} 2 \cos u_R \text{ and } \delta \dot{e}_y = \frac{\Delta v_T}{n_R \Delta t} 2 \sin u_R, \quad (6.7)$$

respectively. Consider that  $\delta e_x \Delta v_T < 0$ . Since  $\sin(\arctan x) = x/\sqrt{1+x^2}$  and  $\cos(\arctan x) = 1/\sqrt{1+x^2}$ , (6.6) can be substituted in (6.7) to obtain

$$\begin{aligned} \delta \dot{e}_x \delta e_x &= \underbrace{\frac{2}{n_R \Delta t}}_{\geq 0} \underbrace{\frac{1}{\sqrt{1 + (\delta e_y / \delta e_x)^2}}}_{\geq 0} \underbrace{\delta e_x \Delta v_T}_{< 0} \leq 0, \text{ and} \\ \delta \dot{e}_y \delta e_y &= \underbrace{\frac{2(\delta e_y)^2}{n_R \Delta t}}_{\geq 0} \underbrace{\frac{1}{\sqrt{1 + (\delta e_y / \delta e_x)^2}}}_{\geq 0} \underbrace{\frac{\Delta v_T}{\delta e_x}}_{< 0} \leq 0. \end{aligned} \quad (6.8)$$

As a result, if neither  $\delta e_x$  nor  $\delta e_y$  is null, the along-track maneuver causes both  $\|\delta e_x\|$  and  $\|\delta e_y\|$  to decrease. If  $\delta e_x$  is null, then the along-track maneuver only affects  $\delta e_y$ , and vice versa. The same process can be applied to prove that this is also true for the case where  $\delta e_x \Delta v_T > 0$ . Hence, both of the eccentricity parameters are controlled by determining the location of the along-track maneuver, even though these orbital elements are not included in the model, and thus have no effect on the magnitude or direction of the along-track maneuver  $\Delta v_T$ .

For the scheduled along-track maneuvers to be executed, the orbit's parameters must be outside a certain maximum design parameter ( $\|\delta L_\lambda\| > 10$  m), otherwise, the scheduled maneuver is not executed. The along-track velocity increment is given by  $\Delta v_T = -[g_1(c_1 \delta i_y + c_2 \delta u) + g_2 c_3 \delta a] a_R$ , where  $g_1$  and  $g_2$  are gains based on constraints required to stabilize the system and limits imposed by design,

and then tuned as necessary [80]. The gain values chosen are

$$g_1 = \text{sgn}(c_3) \frac{\Delta v_{T(\max)}}{a_R \delta L_{\lambda(\max)}} \text{ and } g_2 = \text{sgn}(c_3) \frac{\Delta v_{T(\max)}}{a_R d(\delta L_{\lambda})/dt_{(\max)}}, \quad (6.9)$$

where "sgn" represents the sign function. To control the element  $\delta i_y$ , the cross-track velocity increment is  $\Delta v_N = -g_N \delta i_y a_R$ , where  $g_N = \Delta v_{N(\max)} / a_R \delta i_{y(\max)}$  is a gain that depends on the limitations of the system [16]. This feedback routine will lead to the maximum  $\Delta v_{N(\max)}$  (e.g. the saturation of the actuator) to be applied once the system is at the maximum acceptable deviation ( $a_R \delta i_{y(\max)}$ ), from the reference orbit. The tuning parameters chosen were retrieved from [80], and are shown in Table 6.2.

Table 6.2: Design parameters.

| $\delta L_{\lambda(\max)}$ | $d(\delta L_{\lambda})/dt_{(\max)}$ | $a_R \delta i_{y(\max)}$ | $\Delta v_{T(\max)}$ | $\Delta v_{N(\max)}$    |
|----------------------------|-------------------------------------|--------------------------|----------------------|-------------------------|
| 10 m                       | 10/86400 m/s                        | 40 m                     | $10^{-3}$ m/s        | $1.5 \cdot 10^{-2}$ m/s |

### 6.2.3 LQR design: relative Earth-fixed elements

As previously mentioned, the main mission requirement is the control of the phase differences  $\delta L_{\lambda}, \delta L_{\varphi}$  at the ascending node. However, the linear feedback law described in the previous section also maintains the deviation of the altitude  $\delta h$ . This is due to the fact that  $\delta h$  is a function of the semi-major axis and the eccentricity vector. The linear feedback law of [16, 80] controls the semi-major axis by means of along-track maneuvers (to keep  $d(\delta L_{\lambda})/dt$  and  $\delta u$ ), and the eccentricity vector by means of the placement of the impulsive along-track maneuvers. Since the control scheme proposed in this thesis includes every orbital element, the eccentricity vector can be continuously corrected to maintain the altitude, as well as the phase difference vector. Therefore,  $\delta h$  (at the ascending node) can simply be included as one of the outputs. Hence, a possible choice for the output vector is

$$\mathbf{y} = \left[ \delta L_{\lambda} \quad \delta L_{\varphi} \quad d(\delta L_{\lambda})/dt \quad \delta h \right]_{u=0}^T, \quad (6.10)$$

which can be written in function of the state  $\delta \epsilon$  as

$$\mathbf{y} = \mathbf{H} \delta \epsilon = \begin{bmatrix} 0 & 0 & -2c_2 & 0 & c_1 & c_2 \\ 0 & 0 & -2/c_1 & 0 & 0 & 1/c_1 \\ c_3 & 0 & 0 & 0 & 0 & 0 \\ 1 & -1 & 0 & 0 & 0 & 0 \end{bmatrix} \delta \epsilon. \quad (6.11)$$

The cost function of the LQR problem can then be written as

$$J = \frac{1}{2} \sum_{l=0}^{\infty} (\delta \epsilon_l^T \mathbf{Q}_l \delta \epsilon_l + \delta(\Delta \mathbf{v}_2)_l^T \mathbf{R}_l \delta(\Delta \mathbf{v}_2)_l) = \frac{1}{2} \sum_{l=0}^{\infty} (\mathbf{y}_l^T \mathbf{Q}_l^* \mathbf{y}_l + \delta(\Delta \mathbf{v}_2)_l^T \mathbf{R}_l \delta(\Delta \mathbf{v}_2)_l), \quad (6.12)$$

where  $\mathbf{Q}_l$  can be written in function of the weighting matrix of the outputs  $\mathbf{Q}_l^*$ , as  $\mathbf{Q}_l = \mathbf{H}^T \mathbf{Q}_l^* \mathbf{H}$ , and the output matrix  $\mathbf{H}$  can be considered as constant, evaluated at the initial state of the reference orbit. The LQR weighting matrices were set to  $\mathbf{Q}_l^* = \text{diag}(2.25^2, 15^2, (300/86400)^2, 3^2)^{-1}$ , and  $\mathbf{R}_l = \text{diag}((6.5 \cdot 10^{-7})^2, (2.25 \cdot 10^{-6})^2/2)^{-1}$ , for all  $l$ . Employing this method, the LQR algorithm can be applied to control the phase difference parameters  $\delta L_\lambda$  and  $\delta L_\varphi$ , and the altitude deviation  $\delta h$ , despite being designed in terms of the relative orbital element vector. Note that the primary goal set in [80] is to control the phase difference parameters  $\delta L_\lambda$  and  $\delta L_\varphi$  evaluated at the ascending node ( $u = 0$ ). However, the LQR design proposed in this thesis allows for the problem to be extended to control these parameters at all  $u$ . Examining (6.2) and (6.3), a time-periodic output vector  $\mathbf{H}$  can be developed, noting that  $u \approx u_R$ . This would result in a problem with a periodic tuning matrix with a period of one reference orbit ( $\mathbf{Q}_l = \mathbf{Q}_{l+p}$ ), which can also be solved by the algorithms studied in Chapter 4.

## 6.2.4 Ideal simulation scenario

The relative Earth-fixed elements of the controlled orbit are represented in Figure 6.7, over 1 month, when employing the impulsive control scheme of [16, 80] and when applying the LQR control methodology proposed in this thesis (considering ideal sensors and actuators). The main advantage of the LQR is the vastly superior reference tracking of  $L_\varphi$ . The continuous and impulsive methodologies lead to similar results for the phase difference  $\delta L_\lambda$  and the altitude deviation  $\delta h$ . Still, the impulsive scheme leads to larger variation of the parameters, as the station-keeping maneuvers are larger.

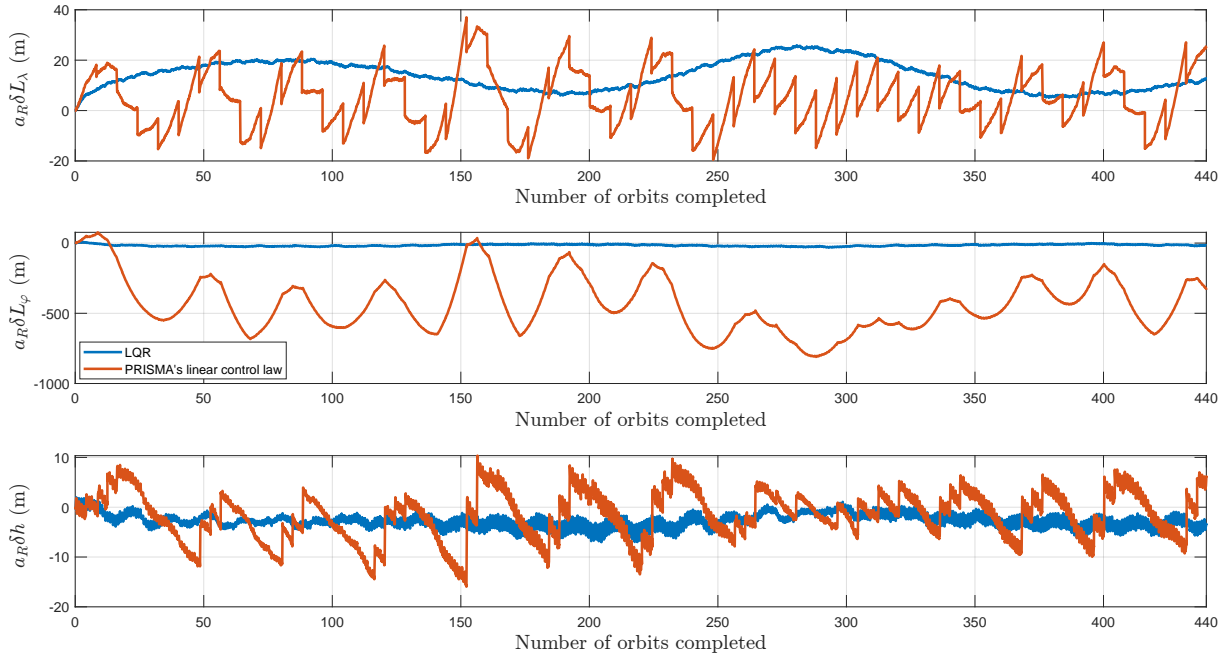


Figure 6.7: Evolution of the relative Earth-fixed elements (at the ascending node).

The relative orbital elements of the controlled orbit are displayed in Figure 6.8. Studying the evolution of  $\delta a$ , it can be noted that due to the scarcity and aggressiveness of the maneuvers commanded by the impulsive scheme, this parameter has a much larger variation for the impulsive scheme than for the continuous control scheme. Since  $\delta u$  is essentially an integrator of  $\delta a$ , the impulsive methodology

displays poor tracking of the reference argument of latitude. The eccentricity parameter  $\delta e_y$  is often larger for the LQR methodology than for the impulsive methodology. This can be explained by the fact that altering  $\delta e_y$  can be used, by the LQR methodology, to decrease  $\delta L_\lambda$  or  $\delta L_\varphi$ . In fact, one of the primary advantages of the methodology proposed in this thesis is that the six orbital parameters are included in the model, whereas the impulsive methodology of [80] separates the problem of in-plane and out-of-plane control, and uses a simplified model without the eccentricity parameters. As a result, the control system proposed herein can directly control  $\delta L_\lambda$  and  $\delta L_\varphi$  by means of small changes to the eccentricity vector and  $\delta i_y$ , unlike the methodology of [80]. Note that the evolution of the parameter  $\delta i_x$  hardly differs between the continuous control scheme and the impulsive control methodology (that places the cross-track maneuvers at  $u = \pi/2$  rad, not affecting the orbit's inclination). This shows that while the control scheme is continuous, fuel is not wasted by applying large maneuvers where these affect  $\delta i_x$  instead of  $\delta i_y$ . In fact, from (6.11), it can be concluded that none of the outputs directly depend on the orbit's inclination. Still, according to the linear time-varying model derived, every other orbital element (except the semi-major axis) depends on  $\delta i_x$ .

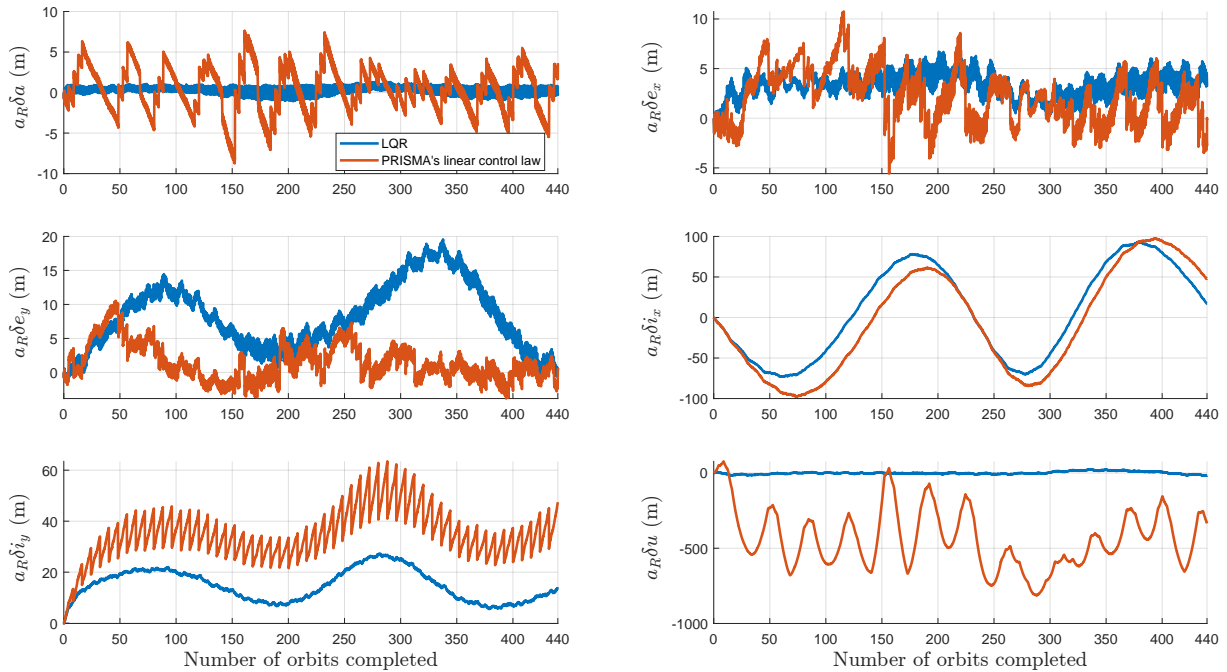


Figure 6.8: Evolution of the relative orbital elements.

The actuation commanded by PRISMA's impulsive control technique is displayed in Figure 6.9, and the actuation of the proposed LQR control methodology is displayed in Figure 6.10. The impulsive cross-track maneuvers, executed at  $u_R = \pi/2$  rad, are always applied in the negative direction in order to decrease  $\delta i_y$ . On the other hand, the continuous cross-track actuation is applied in both directions, as maneuvers applied near  $u_R = 3\pi/2$  rad must be positive in order to decrease  $\delta i_y$ . For both control methodologies, positive and negative along-track delta-v are applied. As previously noted, while negative along-track actuation adds to the effect that the atmospheric drag has on lowering the orbit, it may be necessary to realize such maneuvers in order to meet strict mission requirements.

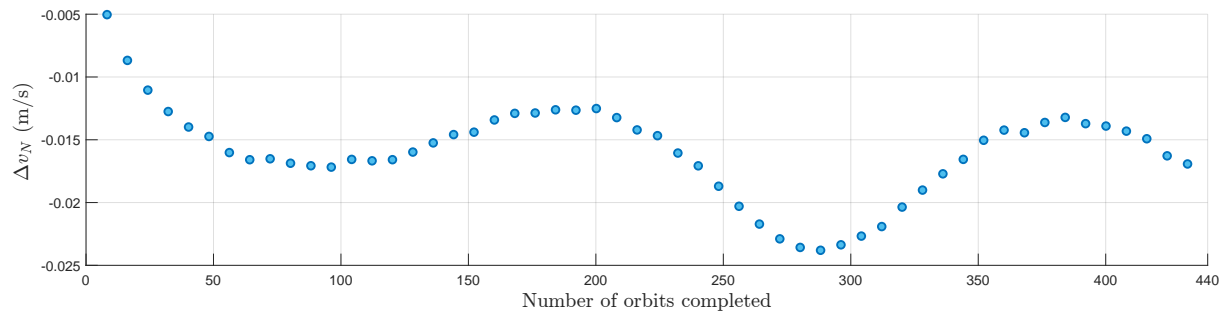
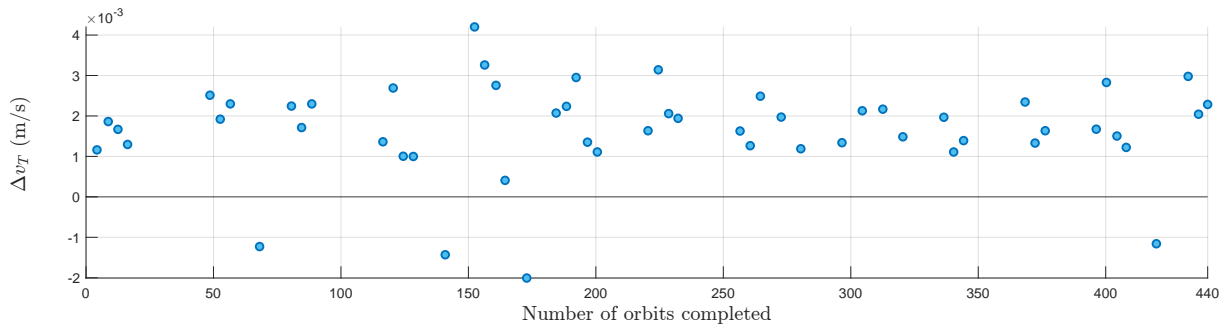


Figure 6.9: Executed maneuvers for the impulsive control scheme.

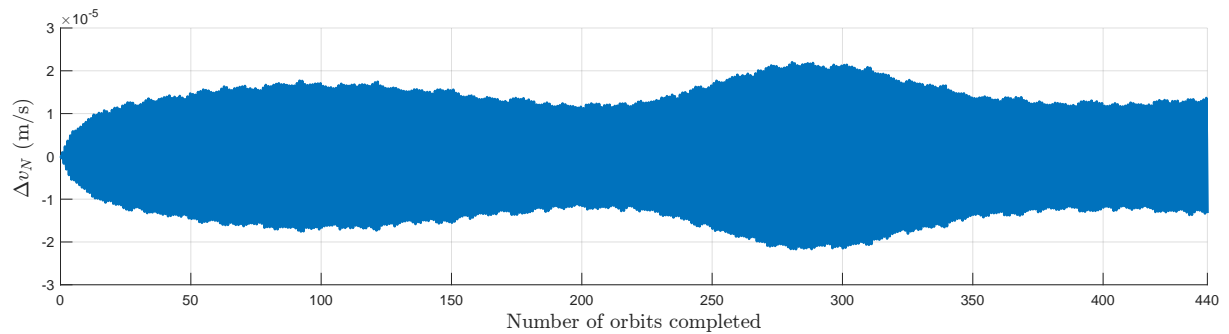
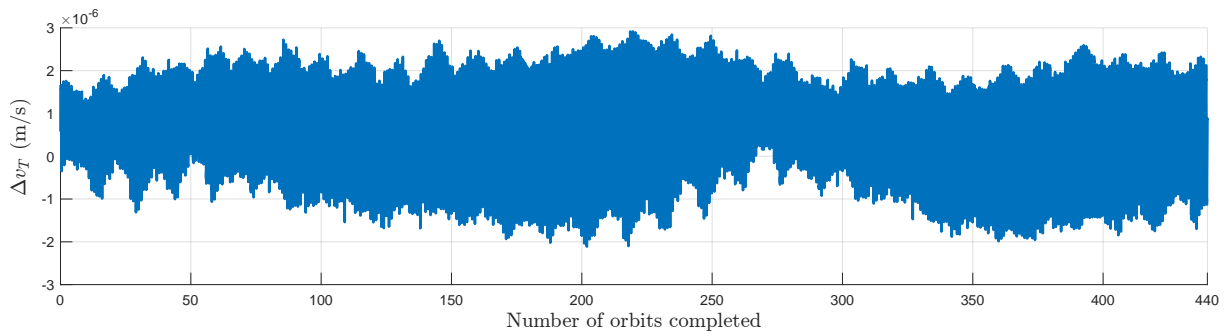


Figure 6.10: Executed maneuvers for the proposed continuous control scheme.

To enrich the analysis of the executed maneuvers for the continuous control scheme, consider Figure 6.11, where the actuation over 15 orbits (orbit 20 to orbit 35) is shown, alongside the equilibrium along-track velocity increment  $\Delta v_{T_0}$ . The cross-track velocity increments are maximum around one fourth and three fourths of every orbit (i.e.  $u_R \approx \pi/2$  rad and  $u_R \approx 3\pi/2$  rad). This is the case since, as previously noted, the error in the tracking of the ascending node  $\delta i_y$  is more vital than the difference in the inclination  $\delta i_x$ , for the mission requirements set. Therefore, the actuation is larger when  $\sin u_R$

is maximum (in magnitude) and almost null when  $\cos u_R$  is large (i.e. the start and half-way point of every orbit). The along-track actuation depends particularly on the tracking error of the semi-major axis,  $\delta a$ . However, it is also strongly influenced by all other parameters except  $\delta i_x$ . As a result, it is more difficult to intuitively understand the commanded along-track velocity increments. Still, it is possible to conclude that throughout the entire month, negative along-track actuation is applied very sparsely. If negative along-track actuation is applied, this is often done in the last fourth of the orbit ( $u_R$  is in the fourth quadrant). This manipulates the eccentricity parameters  $\delta e_x$  and  $\delta e_y$  such that  $\delta L_\lambda$  decreases (since throughout most of the simulation  $\delta L_\lambda > 0$ ) and causes an increase in  $\delta h$  (since during most of the simulation  $\delta h < 0$ ). Very rarely, as seen in orbits 28 to 34, there is also negative actuation in the first quarter of the orbit, which causes an increase in  $\delta L_\varphi$  (since throughout most of the simulation  $\delta L_\varphi < 0$ ).

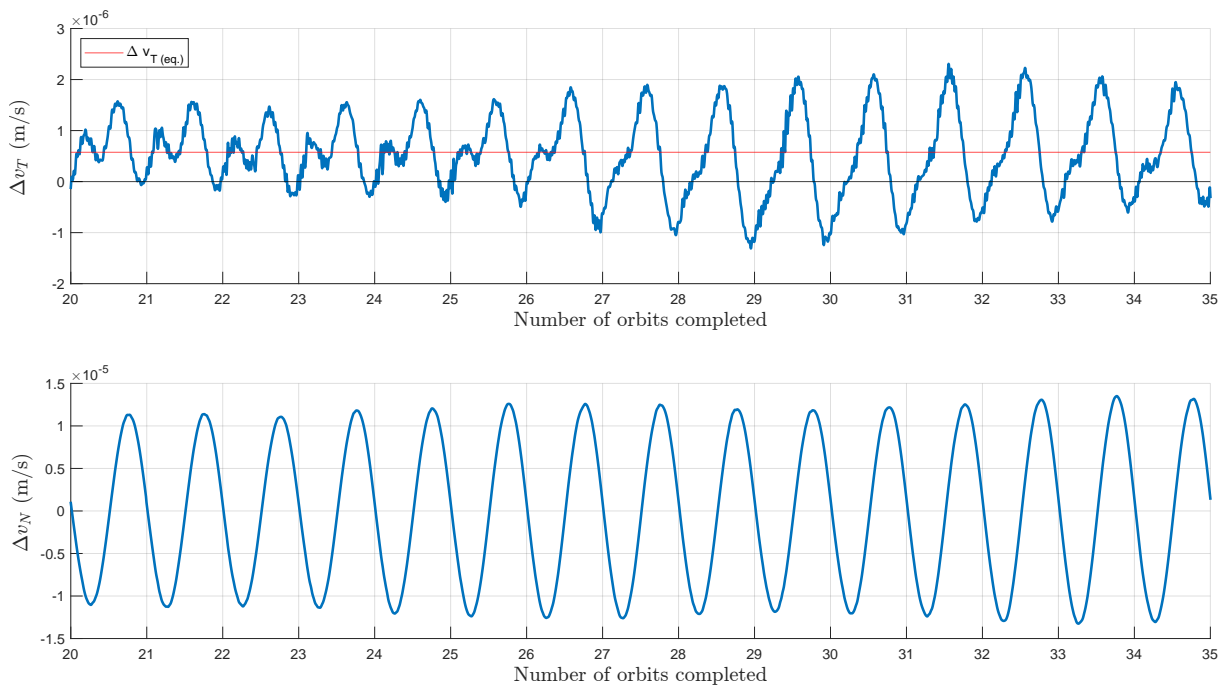


Figure 6.11: Continuous maneuvers executed between orbits 20 and 35.

The distance between the true and reference orbits is shown in Figure 6.12. The control methodology proposed herein leads to more accurate reference tracking than the impulsive control scheme of [16, 80].

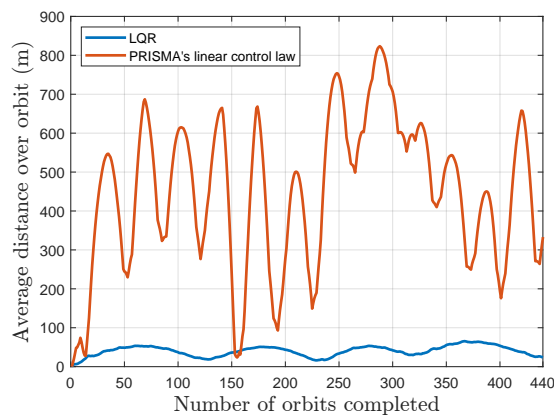


Figure 6.12: Distance between the true and the reference orbit.

The main results are summarized in Table 6.3. The fuel mass was computed taking into account suitable actuators for each control scheme (as will be discussed in Section 6.2.5). Despite the continuous control scheme applying a larger total delta-v, the corresponding fuel consumption is much smaller than for the impulsive scheme. The continuous control scheme allows for the application of low-thrust, efficient propulsion technologies, leading to lower fuel usage than the impulsive scheme, while simultaneously providing better overall performance. Better accuracy can be achieved by tuning the LQR differently for the continuous case, or by decreasing the time between maneuvers, for the impulsive case. However, this would lead to an increase in the fuel consumption for both methods.

Table 6.3: Main characteristics - Ideal scenario.

| Relative Earth-fixed elements |                    | Mean (m) | $\sigma$ (m) | $\Delta v$   | Total (m/s) | Fuel mass                     |
|-------------------------------|--------------------|----------|--------------|--------------|-------------|-------------------------------|
| Control law of [16, 80]       | $\delta L_\lambda$ | 4.9      | 10.8         | $\Delta v_R$ | —           | 61.2 g<br>( $I_{sp} = 252$ s) |
|                               | $\delta L_\varphi$ | -434.8   | 194.6        | $\Delta v_T$ | 0.10        |                               |
|                               | $\delta h$         | -1.7     | 4.8          | $\Delta v_N$ | 0.88        |                               |
| LQR                           | $\delta L_\lambda$ | 13.9     | 5.8          | $\Delta v_R$ | —           | 4.8 g<br>( $I_{sp} = 4500$ s) |
|                               | $\delta L_\varphi$ | -15.7    | 6.8          | $\Delta v_T$ | 0.13        |                               |
|                               | $\delta h$         | -3.0     | 1.4          | $\Delta v_N$ | 1.24        |                               |

## 6.2.5 Realistic simulation scenario

In this section, realistic sensors and actuators are considered. The impulsive and continuous control schemes will employ the same sensors. However, the actuators are chosen in order to fulfill the specific thrust range required by each methodology.

### Sensors and actuators

The GNSS/GPS receiver considered is the PODRIX GNSS Receiver, designed for LEO applications. With Precise Orbit Determination based on on-ground post-processed receiver data, excellent satellite position measurement accuracy can be achieved. An optional software upgrade for Precise Point Positioning (PPP) based on Galileo's High Accuracy Service is also available, providing centimeter level precision for the spacecraft's position [83]. The absolute navigation accuracy for this navigation system is displayed in Table 6.4. The navigation system was modelled considering the *standard performance* (without the PPP software upgrade), as the goal of this section is to study the effects of sensor noise in the control methodologies. The error of the navigation system is modelled as white Gaussian noise, where  $3\sigma$  is chosen as the system's accuracy (so that approximately 99.7% of measurements fall within the accuracy limits). Employing this navigation system, the orbit of the spacecraft (in free fall) was determined over 5 days. The accuracy in the determination of the relative mean orbital elements is displayed in Table 6.5.

Table 6.4: Absolute navigation accuracy - PODRIX GNSS receiver. Retrieved from [83].

| On-board navigation                           | Position accuracy (m) | Velocity accuracy (mm/s) |
|---|-----------------------|--------------------------|
| Standard performance                          | 1                     | 2                        |
| With PPP software upgrade (Galileo-only mode) | 0.2                   | 1                        |

Table 6.5: Orbit determination accuracy with data from the PODRIX GNSS Receiver.

| Relative (mean) orbital element | Mean (cm) | $\sigma$ (m) |
|---------------------------------|-----------|--------------|
| $a_R \delta a$                  | -1        | 0.82         |
| $a_R \delta e_x$                | -0.6      | 0.61         |
| $a_R \delta e_y$                | 0.3       | 0.61         |
| $a_R \delta i_x$                | -0.1      | 0.29         |
| $a_R \delta i_y$                | 0.2       | 0.29         |
| $a_R \delta u$                  | 0.3       | 0.75         |

The PRISMA mission employed a novel high performance green propellant (HPGP) technology for space applications [84]. The propulsion system can be characterized by a minimum impulse value (MIV) and a minimum impulse bit (MIB). Consequently, the thrusters can only deliver values of  $\Delta v$  which are larger than MIV and integer multiples of MIB. Furthermore, the execution error of the thrusters is quantified by the relation  $e_{dV} = \|\Delta v_{\text{real}} - \Delta v_{\text{cmd}}\|/100$ , where  $\Delta v_{\text{cmd}}$  is the velocity increment commanded by the on-board controller, and  $\Delta v_{\text{real}}$  is the actual velocity increment executed by the propulsion system [80]. The parameters characterizing this propulsion system are displayed in Table 6.6.

Table 6.6: PRISMA's propulsion system: performance parameters. Retrieved from [80, 84].

| Accuracy    | Value                 |
|-------------|-----------------------|
| MIV         | $7 \cdot 10^{-4}$ m/s |
| MIB         | $7 \cdot 10^{-5}$ m/s |
| $e_{dV}$    | 5%                    |
| Performance | Value                 |
| $I_{sp}$    | 252 s                 |

The continuous control scheme that is proposed in this thesis requires an actuator which can reliably apply continuous thrust in the range of  $10^0 - 10^2 \mu\text{N}$  (for the studied orbit). It is also desirable to take advantage of the increased efficiency of low-thrust propulsion, employing an actuator with large specific impulse ( $I_{sp}$ ). Consider the Alta's FT-150 FEEP microthruster system (FEEP - Field Emission Electric Propulsion). FEEP is an electrostatic propulsion technology, that uses a liquid metal as a propellant. The characteristics of this propulsion system are displayed in Table 6.7 [85, 86]. Note that the  $I_{sp}$  of this propulsion technology is vastly superior to the one employed in the PRISMA mission, as propulsion technologies tend to be more efficient when less thrust is required.

Table 6.7: Alta's FT-150 Thruster: performance parameters.

| Parameter               | Value                      | Remarks  |
|-------------------------|----------------------------|--|
| Thrust range            | 0.1 to 150 $\mu\text{N}$   | Measured up to 350 $\mu\text{N}^*$                 |
| Thrust resolution (MIB) | Below 100 nN               | —  |
| Thrust accuracy         | See Figure 6.13            | —  |
| $I_{sp}$                | 4500 s (Beginning-of-Life) | 3200 s (End-of-Life)                               |
| Thrust response time    | 50 - 150 ms                | Depending on thrust step                           |
| Propellant mass         | 92 g (per thruster)        | —  |
| Power (nominal)         | 6 W                        | Operative condition at 100 $\mu\text{N}$ of thrust |

\* The power conditioning unit is designed to operate up to 200  $\mu\text{N}$ . Maximum thrust on lab supplies was measured to be 350  $\mu\text{N}$  [86].

The accuracy of the propulsion system depends on the commanded thrust  $T_{\text{cmd}}$ , as noted in Figure 6.13. The propulsion system error will be modelled as white Gaussian noise, with standard deviation chosen such that  $3\sigma$  equals the accuracy range provided in Figure 6.13. Hence, the standard deviation of the white noise is modelled as

$$\begin{cases} 3\sigma = 0.4 \mu\text{N} & \text{if } \|T_{\text{cmd}}\| \leq 4 \mu\text{N}, \\ 3\sigma = \frac{1}{63}\|T_{\text{cmd}}\| + 0.4 \mu\text{N} & \text{if } \|T_{\text{cmd}}\| > 4 \mu\text{N}. \end{cases} \quad (6.13)$$

In conclusion, the propulsion system is modelled with a thrust range between  $0.1 \mu\text{N}$  and  $150 \mu\text{N}$  and a resolution (MIB) of  $100 \text{ nN}$ . The actuation error is modelled as white Gaussian noise, with standard deviation defined by (6.13). The thrust response time ( $50\text{-}150 \text{ ms}$ ) is neglected, since it is considered that the thrust applied is constant throughout the time step of the discretized periodic system ( $\sim 20 \text{ s}$ ), which is much larger than the response time.

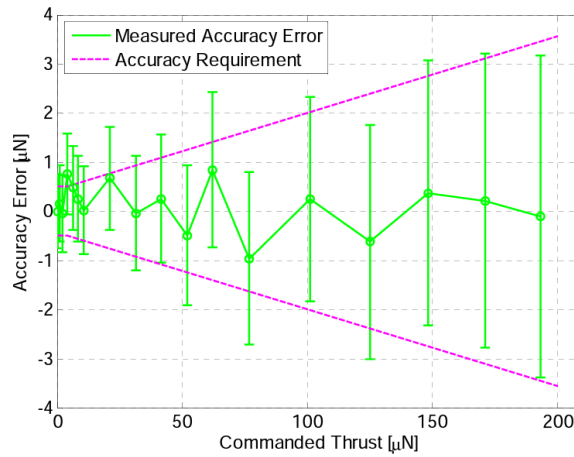


Figure 6.13: Thrust accuracy of Alta's microthruster at nominal temperature. Retrieved from [86].

The controllers were tuned in order to achieve better results for the simulation with realistic sensors and actuators. For the continuous scheme, the weighting matrices were set to

$$\begin{aligned} \mathbf{Q}'_l &= \text{diag} (1.75^2, 15^2, (400/86400)^2, 2.25^2)^{-1} \text{ and} \\ \mathbf{R}_l &= \text{diag} ((4.25 \cdot 10^{-7})^2, (1.8 \cdot 10^{-6})^2/2)^{-1}, \text{ for all } l. \end{aligned} \quad (6.14)$$

The impulsive control methodology did not see tangible improvements with the change of the tuning parameters, so the original controller was used. The evolution of the relative Earth-fixed elements is displayed in Figure 6.14. The evolution of the relative orbital elements vector is displayed in Figure 6.15. Despite the measurement and actuator noise, both methodologies remain capable of controlling the three relative Earth-fixed elements. The control methodology developed in this thesis still attains superior results for the latitude phase difference  $\delta L_\varphi$ .

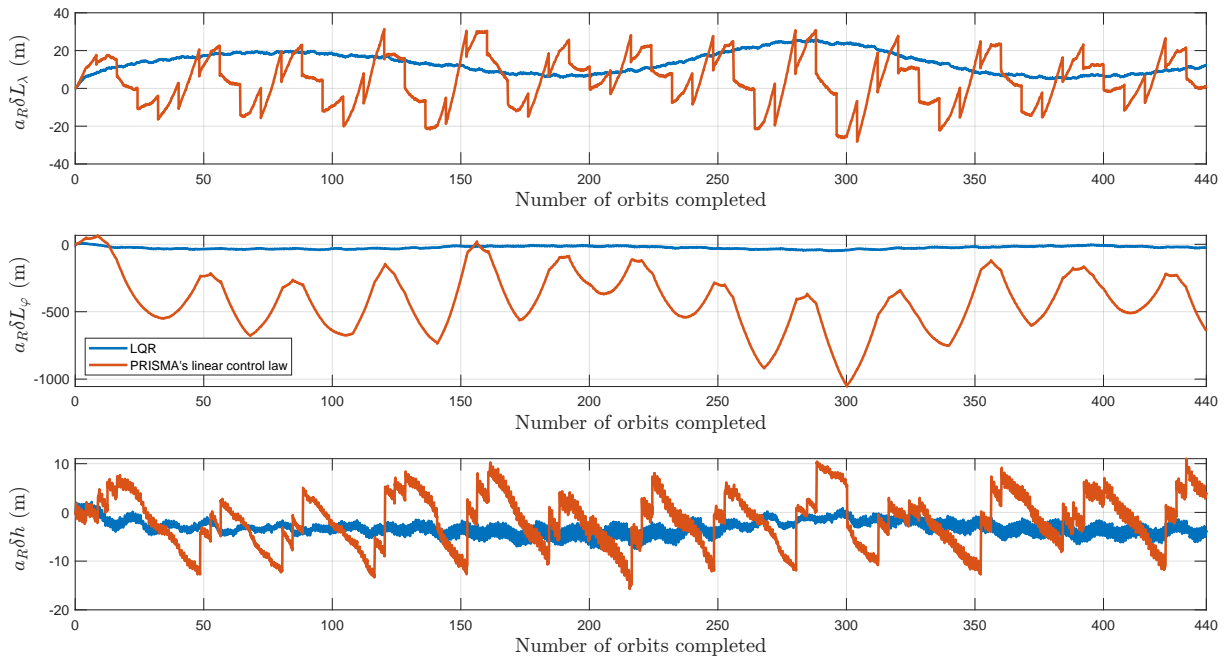


Figure 6.14: Evolution of the relative Earth-fixed elements - Realistic scenario.

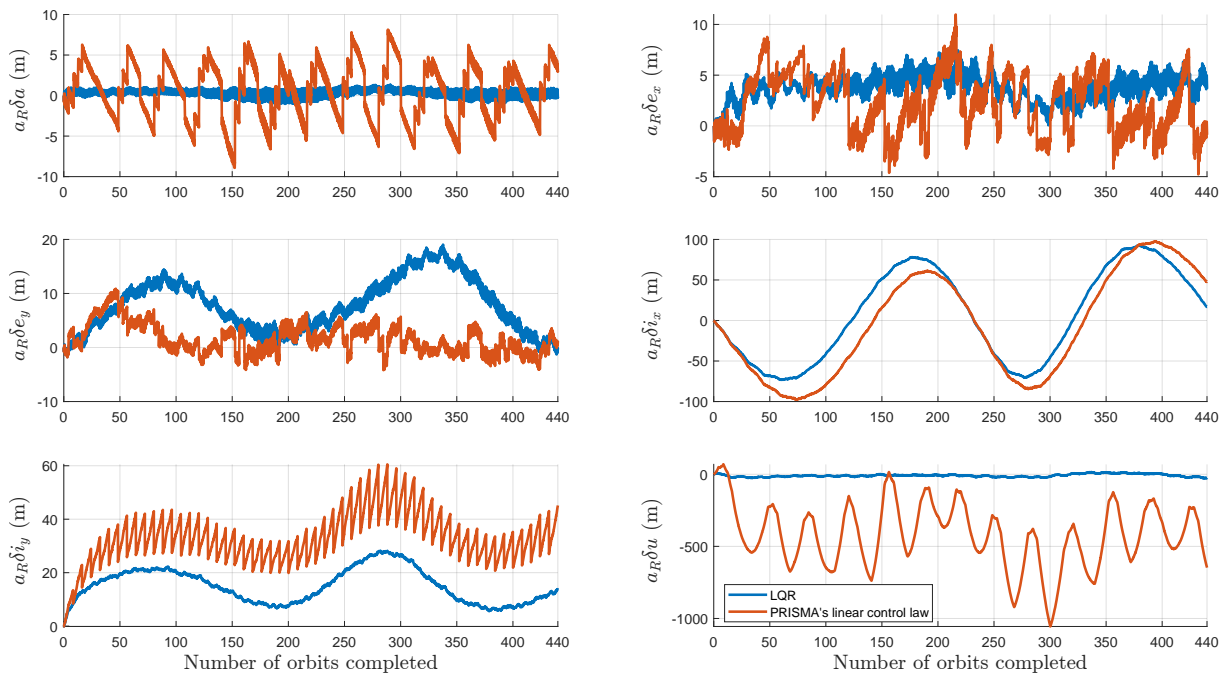


Figure 6.15: Evolution of the relative orbital element vector - Realistic scenario.

The actuation of both methodologies with realistic actuators and sensors are displayed in Figure 6.16 and in Figure 6.17. The actuation noise for the continuous actuation is noticeable (particularly in  $\Delta v_T$ ). The accuracy of the continuous propulsion system is somewhat poor when the commanded thrust is very small (the accuracy of the propulsion system is 400% of the commanded thrust when the minimum thrust of  $0.1 \mu\text{N}$  is commanded). The along-track actuator for the continuous methodology is saturated between the orbits 250 and 325, as the maximum thrust was set to  $150 \mu\text{N}$ . Since the power conditioning unit of the system was designed to operate up to  $200 \mu\text{N}$  [86], better results may be obtained, without

damaging the propulsion system, by increasing the maximum thrust to  $200 \mu\text{N}$  for a short window of time.

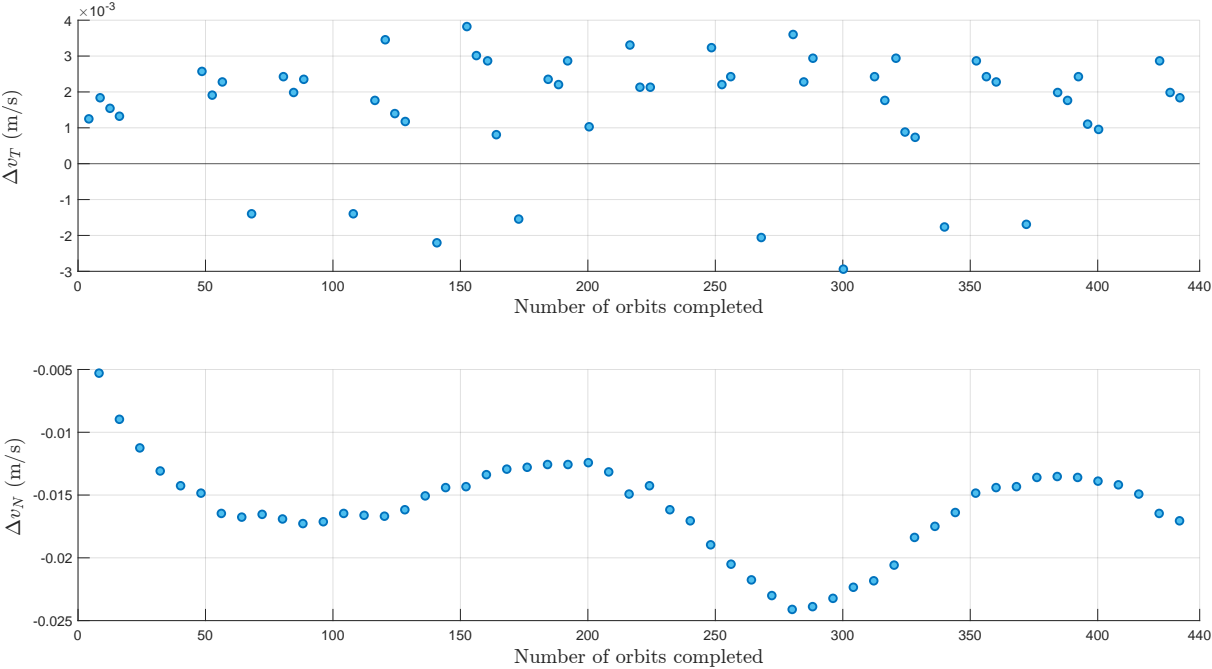


Figure 6.16: Executed maneuvers for the impulsive control scheme - Realistic scenario.

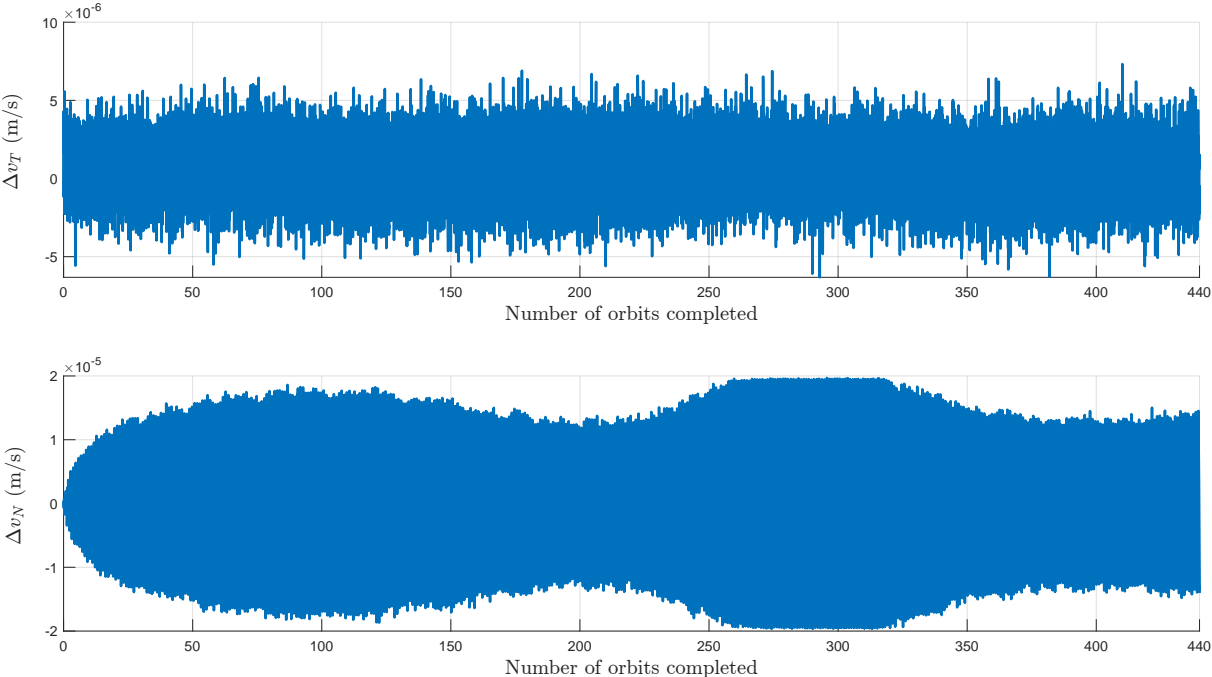


Figure 6.17: Executed maneuvers for the continuous control scheme - Realistic scenario.

The main details are summarized in Table 6.8. The focal difference between the realistic results and the ideal results is an increase in the along-track actuation for both methodologies (increase of 20% for the linear control law of [16, 80], and of 15% for the LQR). The total  $\Delta v$  for the cross-track maneuvers remained approximately the same. Moreover, the tracking of most parameters is slightly

less accurate than for the ideal case (particularly noticed in an increase in the standard deviation of the REFES). It can be concluded that the addition of sensor and actuator noise leads to more fuel consumption being required to achieve similar reference tracking as in the ideal case. However, similarly to the ideal case, both methodologies can still keep  $\delta L_\lambda$  and  $\delta h$  inside a small control window. The LQR method still achieves significantly better results for the tracking of the latitude of the subsatellite point at the ascending node ( $L_\varphi$ ). Moreover, the LQR methodology still accomplishes accurate tracking of  $L_\lambda$ ,  $\delta L_\varphi$ , and  $h$ , with significantly lower fuel usage than the control law of [16, 80].

Table 6.8: Main characteristics - Realistic scenario.

| Relative Earth-fixed elements |                    | Mean (m) | $\sigma$ (m) | $\Delta v$   | Total (m/s) | Fuel mass                     |
|-------------------------------|--------------------|----------|--------------|--------------|-------------|-------------------------------|
| Control law of [16, 80]       | $\delta L_\lambda$ | 3.9      | 12.7         | $\Delta v_R$ | —           | 62.5 g<br>( $I_{sp} = 252$ s) |
|                               | $\delta L_\varphi$ | -421.3   | 217.7        | $\Delta v_T$ | 0.12        |                               |
|                               | $\delta h$         | -1.8     | 5.3          | $\Delta v_N$ | 0.88        |                               |
| LQR                           | $\delta L_\lambda$ | 13.5     | 5.7          | $\Delta v_R$ | —           | 4.9 g<br>( $I_{sp} = 4500$ s) |
|                               | $\delta L_\varphi$ | -24.3    | 10.8         | $\Delta v_T$ | 0.16        |                               |
|                               | $\delta h$         | -3.4     | 1.5          | $\Delta v_N$ | 1.24        |                               |

### 6.3 Orbit injection

In this section, the proposed control scheme is validated for the correction of orbit injection errors. Consider the Ariane 6 launch system, operated from the Guiana Space Center. The typical standard deviation ( $1\sigma$ ) for injection in sun-synchronous orbits at 800 km of altitude (similar to the 710 km of altitude of the PRISMA mission) is displayed in Table 6.9. In addition to the injection errors of Table 6.9, consider also an initial error of 0.02 degrees in the argument of latitude ( $u$ ).

Table 6.9: Ariane 6 launcher's sun-synchronous orbit injection accuracy. Adapted from [87].

| Orbital element             | Accuracy ( $1\sigma$ ) |
|-----------------------------|------------------------|
| Semi-major axis ( $a$ )     | 2.5 km                 |
| Eccentricity ( $e$ )        | $3.5 \cdot 10^{-4}$    |
| Inclination ( $i$ )         | $0.04^\circ$           |
| Ascending node ( $\Omega$ ) | $0.03^\circ$           |

The propulsion system employed consists of four QinetiQ GIE T5 ion thrusters in the along-track and cross-track directions. The actuator dynamics are displayed in Table 6.10 [88, 89]. The sensor employed was the PODRIX GNSS Receiver (with standard performance), whose parameters are displayed in Table 6.4.

Table 6.10: 4x QinetiQ T5 ion thrusters: performance parameters.

| Parameter                     | Value                  |
|-------------------------------|------------------------|
| Thrust range                  | 0.6 to 100 mN          |
| Thrust resolution (MIB)       | 12 $\mu$ N             |
| Thrust accuracy ( $3\sigma$ ) | $\pm 1\%$ of $T_{cmd}$ |
| $I_{sp}$                      | 500 – 3000 s           |
| Power                         | 60 – 600 W             |

The LQR was tuned for the new problem with  $\mathbf{Q}_l = \text{diag}(1/25^2, 1/75^2, 1/75^2, 1/80^2, 1/80^2, 1/80^2)$ , and  $\mathbf{R}_l = \text{diag}(4 \cdot 10^6, 1.25 \cdot 10^5)$ , for all  $l$ . The evolution of the relative orbital element vector, for the first 5 orbits, is displayed in Figure 6.18. It can be noted that the spacecraft is placed in the reference orbit approximately three reference periods after the initial orbit injection (approximately five hours). The error in the semi-major axis decreases rapidly throughout the first half orbit. Then,  $\delta a$  is kept negative for the next orbit and a half in order to increase  $\delta u$  (which is essentially an integrator of  $\delta a$ ). The error in both eccentricity parameters quickly decreases during the first quarter of the reference orbit. However,  $\delta e_x$  quickly rises during the second quarter of the reference orbit, as a consequence of the necessary negative along-track actuation to decrease  $\delta a$ . The error in the eccentricity parameter  $e_x$  then steadily decreases during the following two orbits. As a result of the cross-track maneuvers executed,  $\delta i_x$  and  $\delta i_y$  steadily decrease. Cross-track maneuvers can only simultaneously decrease  $\delta i_x$  and  $\delta i_y$  for half of the orbit (when  $\sin u_R$  and  $\cos u_R$  have the same sign), so there are portions of the orbit where there is a small increase in one of these parameters in order to decrease the other.

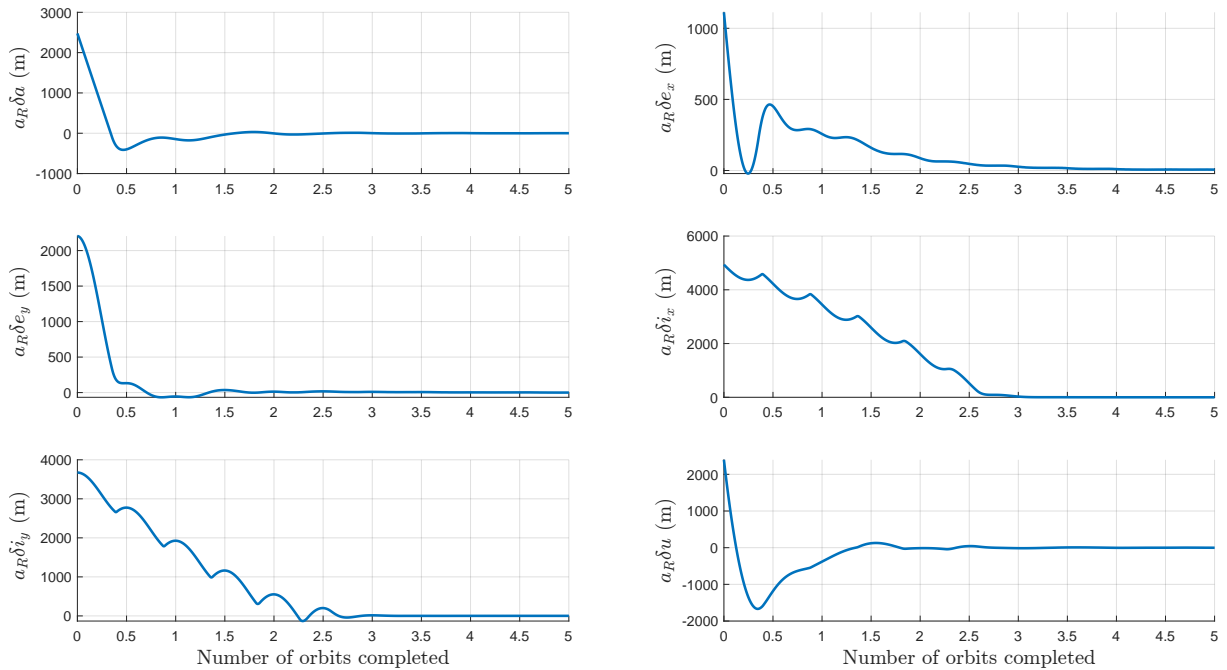


Figure 6.18: Evolution of the relative orbital element vector.

The actuation is displayed in Figure 6.19. The propulsion system is saturated for the along-track direction for the start of the simulation. The thrusters aligned in the cross-track direction are saturated for a large part of the simulation. As expected from observing the evolution of the orbital elements, negative along-track actuation is applied initially to decrease the semi-major axis of the true orbit. The cross-track actuation must always be negative for the first quarter of the orbit, and always positive for the third quarter, in order to decrease both  $\delta i_x$  and  $\delta i_y$ . For the second and third quarter of the orbit, the direction of the maneuvers is mostly decided according to whether the magnitude of  $\sin u_R$  or  $\cos u_R$  is larger, in order to decrease one of the out-of-plane parameters without substantially increasing the other. Hence, the change between negative and positive cross-track maneuvers is performed approximately at 37.5% and 87.5% of a completed orbit (i.e. at  $u_R = 3\pi/4$  rad and  $u_R = 7\pi/4$  rad, respectively, when

$\sin u_R = -\cos u_R$ ). Obviously, other factors such as whether  $\delta i_x$  or  $\delta i_y$  is larger will have an influence on the cross-track actuation (as well as the fact that  $\delta \dot{i}_y$  depends on  $\delta i_x$ , according to the linear models derived).

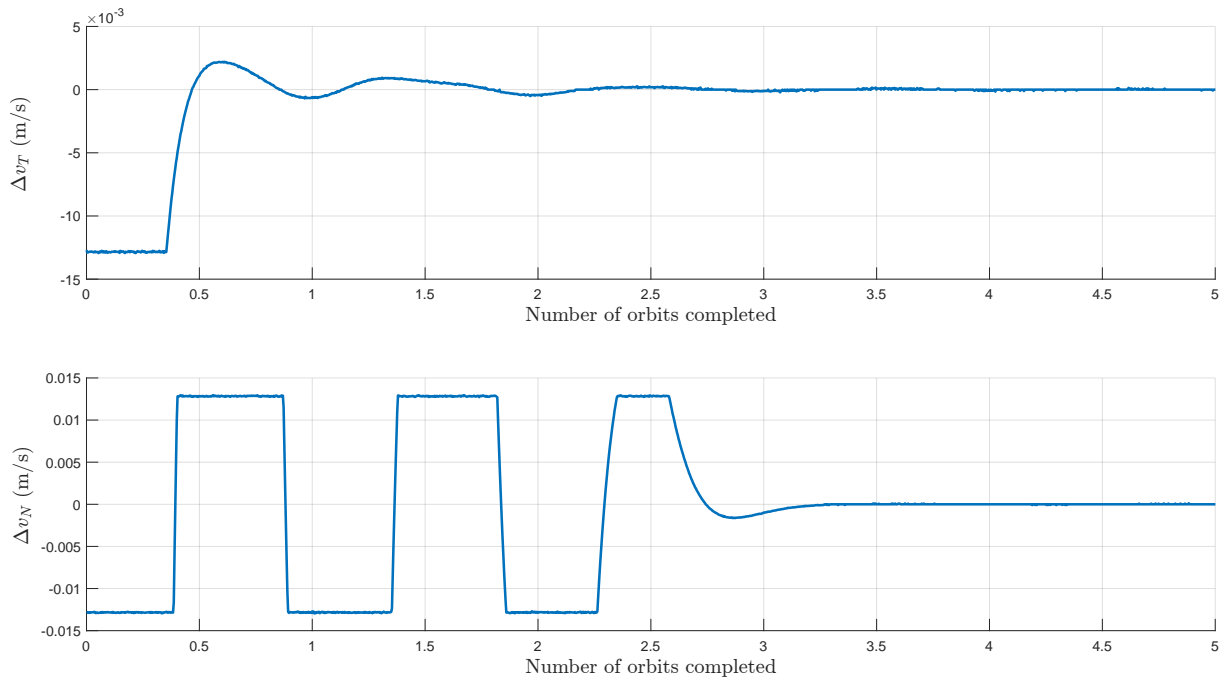


Figure 6.19: Executed maneuvers.

The average distance (per orbit) between the true and the reference spacecraft is displayed in Figure 6.20. It can be noted that the distance between the true and reference orbits is almost null after three reference orbits.

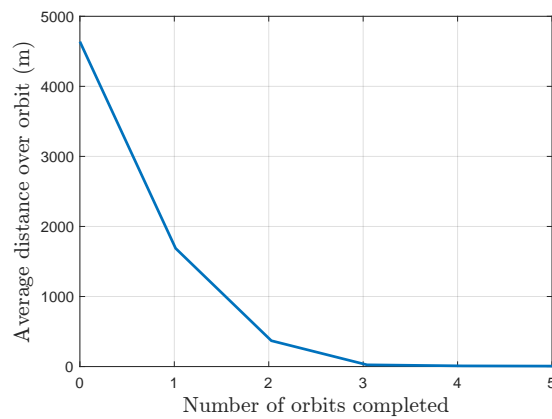


Figure 6.20: Distance between the reference and the true spacecraft.

# Chapter 7

## Conclusions

One of the main contributions of this thesis was showing that the nonlinear model proposed in [16] can be accurately approximated by a discrete-time linear periodic model and, by extension, represented as a linear time-invariant system. It was discussed how the LQR design, for discrete-time linear periodic systems, is associated with the discrete-time periodic Riccati equation. Consequently, an efficient algorithm for the solution of the discrete-time Riccati equation was developed. The proposed algorithm is generally faster than existing methods and solves an important problem, as it can be efficiently applied to singular systems, contrary to algorithms found in the literature. The developed algorithm for the solution of the DPRE was then leveraged in the design of an LQR for autonomous orbit control. The resulting continuous control scheme was compared with the impulsive control scheme proposed in [16], for the PRISMA mission. It was shown that the control method proposed herein can achieve tighter reference tracking than the impulsive method of [16], with a fraction of the fuel consumption. Additionally, the proposed methodology was shown to be capable of correcting orbit injection errors. From the analysis of the continuous actuation employed to maintain the orbit of the PRISMA mission, it became clear that the control scheme developed in this thesis can take advantage of the orbital mechanics associated with the problem, prioritizing maneuvers at the optimal locations along the orbit. This fundamental property results from the fact that the augmented LTI system contains the entire information about an orbital period and models the evolution of every orbital element.

The proposed control scheme does not have the downfalls of various existing autonomous orbit control systems, which require that the location of the maneuvers be chosen *a priori*, employ models which do not include the dynamics of the eccentricity vector, and separately analyze the in-plane and out-of-plane motion of the satellite. An additional benefit of the developed control algorithm is that it does not require costly hardware on-board the spacecraft, as it is computationally light and only requires along-track and cross-track actuation.

In conclusion, all the objectives of this thesis, outlined in Section 1.3, were achieved. The proposed model of the effects of the perturbations on a LEO satellite is simple yet accurate, as suitable LTP and LTI models were derived. As a result, the proposed model can be leveraged in future work, using advanced control methodologies. The control system was validated via high-fidelity simulations, and it was shown

to be vastly more precise and efficient than one of the latest and most accurate autonomous orbit control methods: the control system proposed in [16], for the PRISMA mission.

## 7.1 Future Work

Relevant future work can be separated in three sections. First, it can be noted that while the linear periodic model is quite accurate in relation to the original nonlinear model, neither accurately represents the out-of-plane motion of the satellite, since (less significant) perturbations such as the gravitational pull of the Moon and the Sun are not modelled. The possibility of including these effects in the model should be studied. It is particularly interesting to compute the average of these effects over the orbit of the third-body, so that the periodicity of the model (one reference orbit) can be kept. Secondly, other advanced control methodologies can be applied to this problem. This thesis developed a discrete-time linear periodic model and an equivalent linear time-invariant model. The simplicity of the models derived opens the door to the implementation of complex control methodologies, such as MPC, which are often limited by their substantial computational complexity. Moreover, it can be reasoned that the application of robust control methodologies or adaptive control strategies can prove advantageous, as the erratic variation of the atmospheric density is a roadblock to increasing the performance of orbit control methodologies. Finally, motivated by the large satellite constellations in low Earth orbits, an extension of the proposed control solution to networked satellites can prove fruitful.

In summary, the main recommendations for future work are:

1. Derive suitable mathematical descriptions of the out-of-plane perturbations affecting a satellite's motion, particularly the (averaged) effect of the Moon and the Sun on the satellite's orbit.
2. Take advantage of the models derived herein to design novel advanced automatic control systems for single satellites, aiming for good reference tracking with minimal fuel usage.
3. Extend the control solutions developed for single satellites to networked formations of satellites, while keeping the key properties of the previously derived solutions.

# Bibliography

- [1] ESA Space Debris Office. ESA's Annual Space Environment Report. Technical report, ESA, 2023.
- [2] J. McDowell et al. Orbiting now. <https://orbit.ing-now.com/>. Last accessed: 19/10/2023.
- [3] A. S. Jessica West, Wesley Wark. The Importance of Satellites to Life on Earth. <https://www.cigionline.org/multimedia/the-importance-of-satellites-to-life-on-earth/>. Last accessed: 8/10/2023.
- [4] S. May. What is a satellite? <https://www.nasa.gov/audience/forstudents/5-8/features/nasa-knows/what-is-a-satellite-58.html>. Last accessed: 16/10/2023.
- [5] ESA. Types of orbits. [https://www.esa.int/Enabling\\_Support/Space\\_Transportation/Types\\_of\\_orbits](https://www.esa.int/Enabling_Support/Space_Transportation/Types_of_orbits). Last accessed: 16/10/2023.
- [6] F. Scala et al. Analysis and design of future multiple satellite formation flying L-band missions in low Earth orbit. In *Proceedings of the 73rd International Astronautical Congress*, 2022.
- [7] S. Ji et al. Mega satellite constellation system optimization: From a network control structure perspective. *IEEE Transactions on Wireless Communications*, 21(2), 2022.
- [8] N. Crisp et al. The benefits of very low earth orbit for earth observation missions. *Progress in Aerospace Sciences*, 117, 2020.
- [9] SatNow. What are Low Earth Orbits (LEO)? <https://www.satnow.com/community>. Last accessed: 23/10/2022.
- [10] OECD. *OECD Handbook on Measuring the Space Economy*. OECD, 2020.
- [11] S. D. Florio and S. D'Amico. The precise autonomous orbit keeping experiment on the PRISMA mission. *The Journal of the Astronautical Sciences*, 56, 2008.
- [12] K. Neokleous. Modeling and control of a satellite's geostationary orbit. Master's thesis, Luleå University of Technology, 2007.
- [13] Y. Jiang et al. Aerodynamic drag analysis and reduction strategy for satellites in very low earth orbit. *Aerospace Science and Technology*, 132, 2023.
- [14] H. J. Königsmann et al. Autonomous orbit maintenance system. *Acta Astronautica*, 39(9), 1997.

- [15] C. Cappelletti, S. Battistini, and B. K. Malphrus. *Cubesat Handbook*. Academic Press, 2020.
- [16] S. D. Florio, S. D'Amico, and G. Radice. Precise autonomous orbit control in Low Earth Orbit. In *Proceedings of the AIAA/AAS Astrodynamics Specialist Conference*, 2012.
- [17] A. Garulli et al. Autonomous Low-Earth-Orbit station-keeping with electric propulsion. *Journal of Guidance, Control, and Dynamics*, 34(6), 2011.
- [18] H. Bolandi and S. Abrehdari. Precise autonomous orbit maintenance of a Low Earth Orbit satellite. *Journal of Aerospace Engineering*, 31(4), 2018.
- [19] D. Werner. Living on the edge: Satellites adopt powerful computers. <https://spacenews.com/living-on-the-edge-satellites-adopt-powerful-computers/>. Last accessed: 19/10/2023.
- [20] J. P. Diris et al. Autonomous Orbit Determination and Control in Constellations of Satellites. In *Mission Design and Implementation of Satellite Constellations*, 1998.
- [21] W. JR, C. JL, and C. JT. Autonomous orbit control, initial flight results from UoSAT-12. In *Proceedings of the 23rd annual AAS Guidance and Control Conference*, 2000.
- [22] Y. Plam et al. Autonomous orbit control experience on TacSat-2 using Microcosm's Orbit Control Kit (OCK). In *Proceedings of the 31st annual AAS Guidance and Control Conference*, 2008.
- [23] F. Duchevet and A. Lamy. DEMETER: Experience feedback on operations with an autonomous orbit control demonstrator. In *Proceedings of the SpaceOps Conference*, 2008.
- [24] S. De Florio, S. D'Amico, and G. Radice. Operation concept of the precise autonomous orbit keeping experiment on the PRISMA mission. In *Proceedings of the 8th IAA Symposium on Small Satellites for Earth Observation*, 2011.
- [25] M. Tavakoli and N. Assadian. Model predictive orbit control of a Low Earth Orbit satellite using gauss's variational equations. *Journal of Aerospace Engineering*, 228(13), 2013.
- [26] M. Balandat. Constrained robust optimal trajectory tracking: Model predictive control approaches. Master's thesis, TU Darmstadt, 2010.
- [27] B. J. Naasz. Classical element feedback control for spacecraft orbital maneuvers. Master's thesis, Virginia Polytechnic Institute, 2002.
- [28] H. Schaub et al. Spacecraft formation flying control using mean orbit elements. *Journal of the Astronautical Sciences*, 48(1), 2000.
- [29] R. R. Bate, D. D. Mueller, and J. E. White. *Fundamentals of Astrodynamics*. Dover Publications, 1971.
- [30] R. H. Battin. *An Introduction to the Mathematics and Methods of Astrodynamics, Revised Edition*. American Institute of Aeronautics and Astronautics, 2nd edition, 2001.

- [31] D. Vallado. *Fundamentals of Astrodynamics and Applications*. Springer Dordrecht, 2001.
- [32] W. E. Wiesel. *Modern Astrodynamics*. Aphelion Press Beaver creek, 2nd edition, 2010.
- [33] C. D. Murray and S. F. Dermott. *Solar System Dynamics*. Cambridge University Press, 2000.
- [34] M. Leomanni et al. A class of globally stabilizing feedback controllers for the orbital rendezvous problem. *International Journal of Robust and Nonlinear Control*, 27(18), 2017.
- [35] D. J. Scheeres. *Orbital Motion in Strongly Perturbed Environments*. Springer Berlin, Heidelberg, 2012.
- [36] U. Walter. *Orbit Perturbations*. Springer International Publishing, 2018.
- [37] K. Wakker. *Fundamentals of Astrodynamics*. TU Delft Library, 2015.
- [38] Y. Skiba. *Mathematical Problems of the Dynamics of Incompressible Fluid on a Rotating Sphere*. Springer International, 2017.
- [39] P. Gil. Elementos de mecânica orbital, 2020. In Portuguese.
- [40] C. L. Hassa. Drag coefficient estimation using satellite attitude and orbit data. Master's thesis, Pennsylvania State University, 2013.
- [41] R. Sedwick, D. Miller, and E. Kong. Mitigation of Differential Perturbations in Formation Flying Satellite Clusters. *Journal of the Astronautical Sciences*, 47(3-4), 1999.
- [42] R. Danchick. Conversion of osculating orbital elements. In *Proceedings of the Flight Mechanics/Estimation Theory Symposium*, 1996.
- [43] H. Schaub and J. L. Junkins. *Analytical Mechanics of Space Systems*. AIAA Education Series, 2003.
- [44] H. G. Walter. Conversion of osculating orbital elements into mean elements. *Astronomical Journal*, 72, 1967.
- [45] D. Brouwer. Solution of the problem of artificial satellite theory without drag. *The Astronomical Journal*, 64, 1959.
- [46] B. J. Cain. Determination of mean elements for Brouwer's satellite theory. *Astronomical Journal*, 67, 1962.
- [47] B. Ustinov. Motion of satellites along low-eccentricity orbits in a noncentral terrestrial gravitational field. *Cosmic research*, 2, 1967.
- [48] M. Eckstein and H. Hechler. A reliable derivation of the perturbations due to any zonal and tesseral harmonics of the geopotential for nearly-circular satellite orbits. *Cosmic research*, 1970.
- [49] S. Spiridonova and M. Kirschner. Precise mean orbital elements determination for leo monitoring and maintenance. In *Proceeding of the International Symposium on Space Flight Dynamics*, 2014.

- [50] L. Pedroso. `osculating2mean`. <https://github.com/decenter2021/osculating2mean>. Last accessed: 20/10/2023.
- [51] P. Gurfil and P. Seidelmann. *Celestial Mechanics and Astrodynamics: Theory and Practice*. Springer Berlin, Heidelberg, 2016.
- [52] H. Curtis. *Orbital Mechanics for Engineering Students (Aerospace Engineering)*. John Wiley & Sons, 4th edition, 2019.
- [53] P. J. Teunissen and O. Montenbruck. *Springer Handbook of Global Navigation Satellite Systems*. Springer Cham, 2017.
- [54] C. Koppel and G. Quinsac. Electric thruster selection criteria. In *Proceeding of the 8th European Conference for Aeronautics and Space Sciences (EUCASS)*, 2019.
- [55] F. L. Lewis, D. Vrabie, and V. L. Syrmos. *Optimal control of discrete-time systems*, chapter 2, pages 19–109. John Wiley & Sons, Ltd, 2012.
- [56] J. Hench and A. Laub. Numerical solution of the discrete-time periodic Riccati equation. *IEEE Transactions on Automatic Control*, 39(6), 1994.
- [57] M. Di Carlo, S. d. Graça Marto, and M. Vasile. Extended analytical formulae for the perturbed Keplerian motion under low-thrust acceleration and orbital perturbations. *Celestial Mechanics and Dynamical Astronomy*, 133(3), 2021.
- [58] J. Sharma, B. S. Ratanpal, S. Munshi, and V. Shah. Controllability analysis of motion of artificial satellite under the effect of oblateness of the Earth. Preprint on webpage at <https://arxiv.org/abs/2203.01410>, 2022.
- [59] *Tudat Space*. TU Delft. <https://docs.tudat.space/en/stable/>. Last accessed: 17/10/2023.
- [60] Tudat Team. `tudat-bundle`. <https://github.com/tudat-team/tudat-bundle>. Last accessed: 23/10/2023.
- [61] L. Pedroso and P. Batista. `tudat-matlab-thrust-feedback`. <https://github.com/decenter2021/tudat-matlab-thrust-feedback>. Last accessed: 23/10/2023.
- [62] A. Varga. Computational issues for linear periodic systems: paradigms, algorithms, open problems. *International Journal of Control*, 86(7), 2013.
- [63] F. A. Cuzzola and S. Bittanti. Periodic control of vibrations in helicopters. *IFAC Proceedings Volumes*, 33(9), 2000.
- [64] M. Lovera. Periodic attitude control for satellites with magnetic actuators: An overview. *IFAC Proceedings Volumes*, 34(12), 2001.
- [65] J. F. Camino and I. F. Santos. A periodic linear-quadratic controller for suppressing rotor-blade vibration. *Journal of Vibration and Control*, 25(17), 2019.

- [66] R. Meyer and C. Burrus. A unified analysis of multirate and periodically time-varying digital filters. *IEEE Transactions on Circuits and Systems*, 22(3), 1975.
- [67] S. Bittanti and A. J. Laub. *The Riccati equation*. Springer Berlin, 1991.
- [68] Y. Yang. An efficient algorithm for periodic Riccati equation with periodically time-varying input matrix. *Automatica*, 78, 2017.
- [69] Y. Yang. An efficient LQR design for discrete-time linear periodic system based on a novel lifting method. *Automatica*, 87, 2018.
- [70] I. Andrushka et al. Decentralized control and state estimation of linear time-periodic systems. *International Journal of Robust and Nonlinear Control*, 33, 2022.
- [71] F. Liao, M. Sun, and Usman. Optimal preview control for linear discrete-time periodic systems. *Mathematical Problems in Engineering*, 2019, 2019.
- [72] A. Laub. A Schur method for solving algebraic Riccati equations. *IEEE Transactions on Automatic Control*, 24(6), 1979.
- [73] T. Pappas, A. Laub, and N. Sandell. On the numerical solution of the discrete-time algebraic Riccati equation. *IEEE Transactions on Automatic Control*, 25(4), 1980.
- [74] W. Arnold and A. Laub. Generalized eigenproblem algorithms and software for algebraic Riccati equations. *Proceedings of the IEEE*, 72(12), 1984.
- [75] J. Tyler and F. Tuteur. The use of a quadratic performance index to design multivariable control systems. *IEEE Transactions on Automatic Control*, 11(1), 1966.
- [76] R. Horn and C. Johnson. *Matrix Analysis*. Cambridge University Press, 2013.
- [77] S. De Florio and S. D'Amico. Optimal autonomous orbit control of remote sensing spacecraft. In *Proceedings of the 19th AAS/AIAA Space Flight Mechanics Meeting*, 2009.
- [78] A. F. B. de Almeida Prado. Third-body perturbation in orbits around natural satellites. *Journal of Guidance, Control, and Dynamics*, 26(1), 2003.
- [79] T. Papanikolaou and D. Tsoulis. Assessment of numerical integration methods in the context of low earth orbits and inter-satellite observation analysis. *Acta Geodaetica et Geophysica*, 51, 2016.
- [80] S. Florio, S. D'Amico, and G. Radice. Virtual formation method for precise autonomous absolute orbit control. *Journal of Guidance, Control, and Dynamics*, 37, 2014.
- [81] P. Gurfil and K. Kholoshevnikov. Manifolds and metrics in the relative spacecraft motion problem. *Journal of Guidance, Control, and Dynamics*, 29(4), 2006.
- [82] H. Schaub. Relative orbit geometry through classical orbit element differences. *Journal of Guidance, Control, and Dynamics*, 27, 2004.

- [83] *PODRIX GNSS Receiver*. Beyond Gravity. <https://www.satcatalog.com/component/podrix-gnss-receiver/>. Last accessed: 14/09/2023.
- [84] K. Anflo and R. Möllerberg. Flight demonstration of new thruster and green propellant technology on the PRISMA satellite. *Acta Astronautica*, 65(9), 2009.
- [85] L. Paita et al. Alta's FT-150 FEEP microthruster: Development and qualification status. In *Proceedings of the 31st International Electric Propulsion Conference*, 2009.
- [86] D. Nicolini et al. Direct thrust and thrust noise measurements on the lisa pathfinder field emission thruster. In *Proceedings of the 31st International Electric Propulsion Conference*, 2009.
- [87] *ARIANE 6 User's manual*. Arianspace. <https://www.arianespace.com/vehicle/ariane-6/>. Last accessed: 14/09/2023.
- [88] N. Wallace et al. The GOCE ion propulsion assembly - lessons learnt from the first 22 months of flight operations. In *Proceeding of the 32nd International Electric Propulsion Conference*, 2011.
- [89] P. N. Randall, R. A. Lewis, S. D. Clark, and K. W. Hall. T5 performance, industrialisation and future applications. In *Proceeding of the 36th International Electric Propulsion Conference*, 2019.
- [90] J. P. Hespanha. *Linear Systems Theory*. Princeton University Press, 2nd edition, 2018.

## Appendix A

# Linear model's state and input matrices

This section aims to obtain the state and input matrices of the linear time-varying model (5.10). To that end, recall that the state matrix of the linear time-varying model (5.10) can be written as

$$\mathbf{A}(\mathbf{k}_R, \Delta \mathbf{v}_0) = \left. \frac{\partial [\mathbf{A}_g(\mathbf{k}_f) + \mathbf{A}_d(\mathbf{k}_f) + \mathbf{B}(\mathbf{k}_f) \Delta \mathbf{v}]}{\partial \boldsymbol{\epsilon}} \right|_{\substack{\boldsymbol{\epsilon}_0 \\ \Delta \mathbf{v}_0}} = \mathbf{A}'_g(\mathbf{k}_R) + \mathbf{A}'_d(\mathbf{k}_R) + \mathbf{B}'(\mathbf{k}_R, \Delta \mathbf{v}_0), \quad (\text{A.1})$$

where  $\mathbf{A}'_g$ ,  $\mathbf{A}'_d$  and  $\mathbf{B}'$  are the jacobians of  $\mathbf{A}_g$ ,  $\mathbf{A}_d$  and  $\mathbf{B}$ , respectively. Note that the partial derivatives of any function  $\hbar$  with respect to  $e_x$  and  $e_y$  can be obtained as

$$\begin{bmatrix} \frac{\partial \hbar}{\partial e_x} \\ \frac{\partial \hbar}{\partial e_y} \end{bmatrix} = \begin{bmatrix} \frac{\partial e_x}{\partial e} & \frac{\partial e_y}{\partial e} \\ \frac{\partial e_x}{\partial \omega} & \frac{\partial e_y}{\partial \omega} \end{bmatrix}^{-1} \begin{bmatrix} \frac{\partial \hbar}{\partial e} \\ \frac{\partial \hbar}{\partial \omega} \end{bmatrix}, \quad (\text{A.2})$$

since the transformation  $(e, \omega) \rightarrow (e_x, e_y)$  was employed for the parametrization  $\mathbf{k}$ . That is,

$$\frac{\partial \hbar}{\partial e_x} = \cos \omega \frac{\partial \hbar}{\partial e} - \frac{\sin \omega}{e} \frac{\partial \hbar}{\partial \omega}, \quad \text{and} \quad (\text{A.3a})$$

$$\frac{\partial \hbar}{\partial e_y} = \sin \omega \frac{\partial \hbar}{\partial e} + \frac{\cos \omega}{e} \frac{\partial \hbar}{\partial \omega}. \quad (\text{A.3b})$$

The Jacobian of  $\mathbf{A}_d$  can then be written as

$$\mathbf{A}'_d(\mathbf{k}_R) = \left. \frac{\partial \mathbf{A}_d(\mathbf{k}_f)}{\partial \boldsymbol{\epsilon}} \right|_{\substack{\boldsymbol{\epsilon}_0 \\ \Delta \mathbf{v}_0}} = -\frac{A}{m} C_d \rho \begin{bmatrix} a_{d11} & 0 & 0 & 0 & 0 & 0 \\ a_{d21} & a_{d22} & 0 & 0 & 0 & a_{d26} \\ a_{d31} & 0 & a_{d33} & 0 & 0 & a_{d36} \\ 0 & 0 & 0 & 0 & 0 & 0 \\ 0 & 0 & 0 & 0 & 0 & 0 \\ 0 & 0 & 0 & 0 & 0 & 0 \end{bmatrix}, \quad (\text{A.4})$$

where

$$a_{d11} = \left. \frac{\partial(\sqrt{ua})}{\partial a} \right|_{\substack{\epsilon_0 \\ \Delta \mathbf{v}_0}} = \frac{1}{2} \sqrt{\frac{\mu_\oplus}{a_R}}, \quad (\text{A.5a})$$

$$a_{d21} = \left. \frac{\partial\left((e_x + \cos u)\sqrt{\mu_\oplus/a}\right)}{\partial a} \right|_{\substack{\epsilon_0 \\ \Delta \mathbf{v}_0}} = -\frac{1}{2} n_R (e_{xR} + \cos u_R) a_R, \quad (\text{A.5b})$$

$$a_{d31} = \left. \frac{\partial\left((e_y + \sin u)\sqrt{\mu_\oplus/a}\right)}{\partial a} \right|_{\substack{\epsilon_0 \\ \Delta \mathbf{v}_0}} = -\frac{1}{2} n_R (e_{yR} + \sin u_R) a_R, \quad (\text{A.5c})$$

$$a_{d22} = \left. \frac{\partial\left((e_x + \cos u)\sqrt{\mu_\oplus/a}\right)}{\partial e_x} \right|_{\substack{\epsilon_0 \\ \Delta \mathbf{v}_0}} = \sqrt{\frac{\mu_\oplus}{a_R}}, \quad (\text{A.5d})$$

$$a_{d33} = \left. \frac{\partial\left((e_y + \sin u)\sqrt{\mu_\oplus/a}\right)}{\partial e_y} \right|_{\substack{\epsilon_0 \\ \Delta \mathbf{v}_0}} = \sqrt{\frac{\mu_\oplus}{a_R}}, \quad (\text{A.5e})$$

$$a_{d26} = \left. \frac{\partial\left((e_x + \cos u)\sqrt{\mu_\oplus/a}\right)}{\partial u} \right|_{\substack{\epsilon_0 \\ \Delta \mathbf{v}_0}} = -\sqrt{\frac{\mu_\oplus}{a_R}} \sin u_R, \text{ and} \quad (\text{A.5f})$$

$$a_{d36} = \left. \frac{\partial\left((e_y + \sin u)\sqrt{\mu_\oplus/a}\right)}{\partial u} \right|_{\substack{\epsilon_0 \\ \Delta \mathbf{v}_0}} = \sqrt{\frac{\mu_\oplus}{a_R}} \cos u_R. \quad (\text{A.5g})$$

Since the equilibrium delta-v in the radial and cross-track direction ( $\Delta v_{R_0}$  and  $\Delta v_{N_0}$ , respectively) is null, the Jacobian of  $\tilde{\mathbf{B}}\Delta\mathbf{v}$ , at the equilibrium point, is given by

$$\mathbf{B}'(\mathbf{k}_R, \Delta\mathbf{v}_0) = \left. \frac{\partial(\mathbf{B}(\mathbf{k}_f)\Delta\mathbf{v})}{\partial \epsilon} \right|_{\substack{\epsilon_0 \\ \Delta \mathbf{v}_0}} = \begin{bmatrix} b_{11} & 0 & 0 & 0 & 0 & 0 \\ b_{21} & 0 & 0 & 0 & 0 & b_{26} \\ b_{31} & 0 & 0 & 0 & 0 & b_{36} \\ 0 & 0 & 0 & 0 & 0 & 0 \\ 0 & 0 & 0 & 0 & 0 & 0 \\ 0 & 0 & 0 & 0 & 0 & 0 \end{bmatrix} \frac{\Delta v_{T_0}}{\Delta t}, \quad (\text{A.6})$$

where  $\Delta v_{T_0}$  is the equilibrium delta-v in the along-track direction and

$$b_{11} = \left. \frac{\partial(2a/v)}{\partial a} \right|_{\substack{\epsilon_0 \\ \Delta \mathbf{v}_0}} = 3\sqrt{\frac{a_R}{\mu_\oplus}}, \quad (\text{A.7a})$$

$$b_{21} = \left. \frac{\partial(2\cos u/v)}{\partial a} \right|_{\substack{\epsilon_0 \\ \Delta \mathbf{v}_0}} = 3\cos u_R \sqrt{\frac{a_R}{\mu_\oplus}}, \quad (\text{A.7b})$$

$$b_{31} = \left. \frac{\partial(2\sin u/v)}{\partial a} \right|_{\substack{\epsilon_0 \\ \Delta \mathbf{v}_0}} = 3\sin u_R \sqrt{\frac{a_R}{\mu_\oplus}}, \quad (\text{A.7c})$$

$$b_{26} = \left. \frac{\partial(2\cos u/v)}{\partial u} \right|_{\substack{\epsilon_0 \\ \Delta \mathbf{v}_0}} = -2\sin u_R \sqrt{\frac{a_R}{\mu_\oplus}}, \quad (\text{A.7d})$$

$$b_{36} = \left. \frac{\partial(2\sin u/v)}{\partial u} \right|_{\substack{\epsilon_0 \\ \Delta \mathbf{v}_0}} = 2\cos u_R \sqrt{\frac{a_R}{\mu_\oplus}}. \quad (\text{A.7e})$$

The Jacobian of  $\tilde{\mathbf{A}}_g$  can be obtained through the same process, resulting in

$$\mathbf{A}'_g(\mathbf{k}_R) = \frac{3}{4} \left( \frac{R_\oplus}{a_R} \right)^2 \frac{n_R J_2}{(1 - e_R^2)^2} \begin{bmatrix} 0 & 0 & 0 & 0 & 0 & 0 \\ a_{g21} & a_{g22} & a_{g23} & a_{g24} & 0 & 0 \\ a_{g31} & a_{g32} & a_{g33} & a_{g34} & 0 & 0 \\ 0 & 0 & 0 & 0 & 0 & 0 \\ a_{g51} & a_{g52} & a_{g53} & a_{g54} & 0 & 0 \\ a_{g61} & a_{g62} & a_{g63} & a_{g64} & 0 & 0 \end{bmatrix} - \begin{bmatrix} 0 & \dots & 0 \\ \vdots & \ddots & \vdots \\ \frac{3n_R}{2} & \dots & 0 \end{bmatrix}, \quad (\text{A.8})$$

where

$$\begin{aligned} a_{g21} &= \frac{7}{2}(5 \cos^2 i_R - 1)e_{y_R}, & a_{g22} &= -\frac{4(5 \cos^2 i_R - 1)}{(1 - e_R^2)}e_{x_R}e_{y_R}, \\ a_{g23} &= -(5 \cos^2 i_R - 1) \left( \frac{4e_{y_R}^2}{(1 - e_R^2)} + 1 \right), & a_{g24} &= 10e_{y_R} \sin i_R \cos i_R, \\ a_{g31} &= -\frac{7}{2}(5 \cos^2 i_R - 1)e_{x_R}, & a_{g32} &= (5 \cos^2 i_R - 1) \left( \frac{4e_{x_R}^2}{(1 - e_R^2)} + 1 \right), \\ a_{g33} &= \frac{4(5 \cos^2 i_R - 1)}{(1 - e_R^2)}e_{x_R}e_{y_R}, & a_{g34} &= -10e_{x_R} \sin i_R \cos i_R, \\ a_{g51} &= 7 \cos i_R \sin i_R, & a_{g52} &= -\frac{8e_{x_R}}{(1 - e_R^2)} \sin i_R \cos i_R, \\ a_{g53} &= -\frac{8e_{y_R}}{(1 - e_R^2)} \sin i_R \cos i_R, & a_{g54} &= 2 \sin^2 i_R, \\ a_{g61} &= -\frac{7}{2}[5 \cos^2 i_R - 1 + (3 \cos^2 i_R - 1)\sqrt{1 - e_R^2}], \\ a_{g62} &= \frac{e_{x_R}}{(1 - e_R^2)}[4(5 \cos^2 i_R - 1) + 3(3 \cos^2 i_R - 1)\sqrt{1 - e_R^2}], \\ a_{g63} &= \frac{e_{y_R}}{(1 - e_R^2)}[4(5 \cos^2 i_R - 1) + 3(3 \cos^2 i_R - 1)\sqrt{1 - e_R^2}], \\ a_{g64} &= -2(5 + 3\sqrt{1 - e_R^2}) \sin i_R \cos i_R. \end{aligned}$$

As noted in (A.1), the input matrix  $\mathbf{A}$  is given by  $\mathbf{A}(\mathbf{k}_R, \Delta \mathbf{v}_0) = \mathbf{A}'_g(\mathbf{k}_R) + \mathbf{A}'_d(\mathbf{k}_R) + \mathbf{B}'(\mathbf{k}_R, \Delta \mathbf{v}_0)$ .

The input matrix  $\mathbf{B}(\mathbf{k}_R)$  can be obtained directly by adapting (3.16) to the new parametrization  $\epsilon$ , as per (5.2), resulting in

$$\mathbf{B}(\mathbf{k}_R) = \frac{1}{n_R \Delta t} \begin{bmatrix} 0 & 2 & 0 \\ \sin u_R & 2 \cos u_R & 0 \\ -\cos u_R & 2 \sin u_R & 0 \\ 0 & 0 & \cos u_R \\ 0 & 0 & \sin u_R \\ -2 & 0 & -\sin u_R / \tan i_R \end{bmatrix}. \quad (\text{A.9})$$



# Appendix B

## Addendums to Chapter 4

Various theorems and remarks necessary for the development of the algorithm proposed in Chapter 4 are proved in this annex.

### B.1 Necessary conditions for the solution of the DPRE

This section aims to show that the condition that all the pairs  $(\mathbf{A}_l, \mathbf{B}_l)$  are stabilizable is not equivalent to the stabilizability of  $(\bar{\mathbf{A}}, \bar{\mathbf{B}})$ , and the condition that the pairs  $(\mathbf{A}_l, \mathbf{C}_l)$  are detectable is not equivalent to the detectability of  $(\bar{\mathbf{A}}, \bar{\mathbf{C}})$ , following the examples of [71].

Consider a periodic system, with  $p = 2$ , where

$$\begin{aligned} \mathbf{A}_0 &= \begin{bmatrix} 1 & 0 \\ 0 & 1 \end{bmatrix} & \mathbf{B}_0 &= \begin{bmatrix} 1 \\ 0 \end{bmatrix} & \mathbf{C}_0 &= \begin{bmatrix} 1 & 0 \end{bmatrix} \\ \mathbf{A}_1 &= \begin{bmatrix} 1 & 2 \\ 2 & 1 \end{bmatrix} & \mathbf{B}_1 &= \begin{bmatrix} 0 \\ 1 \end{bmatrix} & \mathbf{C}_1 &= \begin{bmatrix} 1 & 0 \end{bmatrix}. \end{aligned} \tag{B.1}$$

Using the Popov-Belevitch-Hautus criterion, it can be shown that the pair  $(\mathbf{A}_0, \mathbf{B}_0)$  is not stabilizable, since  $\begin{bmatrix} \lambda \mathbf{I} - \mathbf{A}_0 & \mathbf{B}_0 \end{bmatrix}$  is not full rank for  $\lambda = 1$ . However, considering the resulting augmented state and input matrices, given by

$$\bar{\mathbf{A}} = \begin{bmatrix} 0 & 0 & 1 & 0 \\ 0 & 0 & 0 & 1 \\ 0 & 0 & 1 & 2 \\ 0 & 0 & 2 & 1 \end{bmatrix} \quad \text{and} \quad \bar{\mathbf{B}} = \begin{bmatrix} 1 & 0 \\ 0 & 0 \\ 1 & 0 \\ 2 & 1 \end{bmatrix}, \tag{B.2}$$

respectively, it can be noted that  $(\bar{\mathbf{A}}, \bar{\mathbf{B}})$  is stabilizable [71, 90]. Through the same discussion, it can be shown that the pairs  $(\mathbf{A}_l, \mathbf{C}_l)$  being detectable is not a necessary condition for the detectability of

$(\bar{\mathbf{A}}, \bar{\mathbf{C}})$ . Consider a different periodic system, with  $p = 2$  and

$$\mathbf{A}_0 = \begin{bmatrix} 0 & 1 \\ 1 & 0 \end{bmatrix} \quad \mathbf{B}_0 = \begin{bmatrix} 1 \\ 0 \end{bmatrix} \quad \mathbf{C}_0 = [0 \quad 1] \quad (\text{B.3})$$

$$\mathbf{A}_1 = \begin{bmatrix} 0 & 1 \\ 1 & 1 \end{bmatrix} \quad \mathbf{B}_1 = \begin{bmatrix} 0 \\ 1 \end{bmatrix} \quad \mathbf{C}_1 = [0 \quad 1].$$

It can be shown that both the pairs  $(\mathbf{A}_l, \mathbf{B}_l)$  are controllable, on the other hand, considering the resultant augmented state, given by

$$\bar{\mathbf{A}} = \begin{bmatrix} 0 & 0 & 0 & 1 \\ 0 & 0 & 1 & 0 \\ 0 & 0 & 1 & 0 \\ 0 & 0 & 1 & 1 \end{bmatrix} \quad \text{and} \quad \bar{\mathbf{B}} = \begin{bmatrix} 1 & 0 \\ 0 & 0 \\ 0 & 0 \\ 1 & 1 \end{bmatrix}, \quad (\text{B.4})$$

it can be noted that  $[\lambda \mathbf{I} - \bar{\mathbf{A}} \mid \bar{\mathbf{B}}]$  does not have full row rank (in fact the third row is null) for  $\lambda = 1$ , which implies that  $(\bar{\mathbf{A}}, \bar{\mathbf{B}})$  is not stabilizable. Additionally, it can be noted that the pairs  $(\mathbf{A}_l, \mathbf{C}_l)$  are observable (and therefore, also detectable). However, that is not the case for the pair  $(\bar{\mathbf{A}}, \bar{\mathbf{C}})$  [71].

## B.2 Solution to the augmented Riccati equation

This section aims to more thoroughly describe the efficient method proposed in Yang (2018), for the LQR design problem of the augmented system associated with the Riccati equation

$$\bar{\mathbf{A}}^T \bar{\mathbf{P}} \bar{\mathbf{A}} - \bar{\mathbf{A}}^T \bar{\mathbf{P}} \bar{\mathbf{B}} (\bar{\mathbf{R}} + \bar{\mathbf{B}}^T \bar{\mathbf{P}} \bar{\mathbf{B}})^{-1} \bar{\mathbf{B}}^T \bar{\mathbf{P}} \bar{\mathbf{A}} + \bar{\mathbf{Q}} = \bar{\mathbf{P}}. \quad (\text{4.13})$$

Consider the partitioned augmented state matrices

$$\bar{\mathbf{A}} = \left[ \begin{array}{ccc|ccc} \mathbf{0} & \cdots & \mathbf{0} & & & \mathbf{A}_0 \\ \mathbf{0} & \cdots & \mathbf{0} & & & \mathbf{A}_1 \mathbf{A}_0 \\ \vdots & \ddots & \vdots & & & \vdots \\ \mathbf{0} & \cdots & \mathbf{0} & & & \mathbf{A}_{p-2} \cdots \mathbf{A}_1 \mathbf{A}_0 \\ \hline \mathbf{0} & \cdots & \mathbf{0} & & & \mathbf{A}_{p-1} \cdots \mathbf{A}_1 \mathbf{A}_0 \end{array} \right] = \left[ \begin{array}{c|c} \mathbf{0} & \bar{\mathbf{A}}_1 \\ \hline \mathbf{0} & \bar{\mathbf{A}}_2 \end{array} \right] = \left[ \mathbf{0} \mid \bar{\mathbf{F}} \right], \quad (\text{B.5})$$

where  $\bar{\mathbf{A}}_2 \in \mathbb{R}^{n \times n}$ ,  $\bar{\mathbf{F}} = [\bar{\mathbf{A}}_1^T, \bar{\mathbf{A}}_2^T]^T$  and

$$\bar{\mathbf{B}} = \left[ \begin{array}{ccccc} \mathbf{B}_0 & \mathbf{0} & \cdots & \mathbf{0} & \mathbf{0} \\ \mathbf{A}_1 \mathbf{B}_0 & \mathbf{B}_1 & \cdots & \mathbf{0} & \mathbf{0} \\ \vdots & \vdots & \ddots & \vdots & \vdots \\ \hline \mathbf{A}_{p-2} \cdots \mathbf{A}_1 \mathbf{B}_0 & \mathbf{A}_{p-2} \cdots \mathbf{A}_2 \mathbf{B}_1 & \cdots & \mathbf{B}_{p-2} & \mathbf{0} \\ \mathbf{A}_{p-1} \cdots \mathbf{A}_1 \mathbf{B}_0 & \mathbf{A}_{p-1} \cdots \mathbf{A}_2 \mathbf{B}_1 & \cdots & \mathbf{A}_{p-1} \mathbf{B}_{p-2} & \mathbf{B}_{p-1} \end{array} \right] = \left[ \begin{array}{c} \bar{\mathbf{B}}_1 \\ \bar{\mathbf{B}}_2 \end{array} \right], \quad (\text{B.6})$$

where  $\bar{\mathbf{B}}_2 \in \mathbb{R}^{n \times pm}$ . Additionally, recall that

$$\bar{\mathbf{Q}} = \left[ \begin{array}{c|c} \bar{\mathbf{Q}}_1 & \mathbf{0} \\ \hline \mathbf{0} & \bar{\mathbf{Q}}_2 \end{array} \right], \text{ and } \bar{\mathbf{R}} = \left[ \begin{array}{c|c} \bar{\mathbf{R}}_1 & \mathbf{0} \\ \hline \mathbf{0} & \bar{\mathbf{R}}_2 \end{array} \right], \quad (\text{B.7})$$

where  $\bar{\mathbf{Q}}_1 = \text{diag}(\mathbf{Q}_0, \dots, \mathbf{Q}_{p-2})$ ,  $\bar{\mathbf{R}}_1 = \text{diag}(\mathbf{R}_0, \dots, \mathbf{R}_{p-2})$ ,  $\bar{\mathbf{Q}}_2 = \mathbf{Q}_{p-1} \in \mathbb{R}^{n \times n}$ , and  $\bar{\mathbf{R}}_2 = \mathbf{R}_{p-1} \in \mathbb{R}^{n \times n}$ . Finally, denote

$$\bar{\mathbf{P}} = \left[ \begin{array}{cc} \bar{\mathbf{P}}_{11} & \bar{\mathbf{P}}_{12} \\ \bar{\mathbf{P}}_{21} & \bar{\mathbf{P}}_{22} \end{array} \right] \left. \begin{array}{l} \left. \vphantom{\begin{matrix} \bar{\mathbf{P}}_{11} \\ \bar{\mathbf{P}}_{21} \end{matrix}} \right\} (p-1)n \\ \left. \vphantom{\begin{matrix} \bar{\mathbf{P}}_{12} \\ \bar{\mathbf{P}}_{22} \end{matrix}} \right\} n \end{array} \right\} n \quad (\text{B.8})$$

and

$$\bar{\mathbf{Y}} = \bar{\mathbf{P}}\bar{\mathbf{B}}(\bar{\mathbf{R}} + \bar{\mathbf{B}}^T\bar{\mathbf{P}}\bar{\mathbf{B}})^{-1}\bar{\mathbf{B}}^T\bar{\mathbf{P}}. \quad (\text{B.9})$$

Substituting (B.5)-(B.9) in the time-invariant Riccati equation (4.13), yields

$$\begin{bmatrix} \mathbf{0} \\ \bar{\mathbf{F}}^T \end{bmatrix} \bar{\mathbf{P}} \begin{bmatrix} \mathbf{0} & \bar{\mathbf{F}} \end{bmatrix} - \begin{bmatrix} \mathbf{0} \\ \bar{\mathbf{F}}^T \end{bmatrix} \bar{\mathbf{Y}} \begin{bmatrix} \mathbf{0} & \bar{\mathbf{F}} \end{bmatrix} + \begin{bmatrix} \bar{\mathbf{Q}}_1 & \mathbf{0} \\ \mathbf{0} & \bar{\mathbf{Q}}_2 \end{bmatrix} = \begin{bmatrix} \bar{\mathbf{P}}_{11} & \bar{\mathbf{P}}_{12} \\ \bar{\mathbf{P}}_{21} & \bar{\mathbf{P}}_{22} \end{bmatrix}, \quad (\text{B.10})$$

or equivalently

$$\begin{bmatrix} \mathbf{0} & \mathbf{0} \\ \mathbf{0} & \bar{\mathbf{F}}^T\bar{\mathbf{P}}\bar{\mathbf{F}} \end{bmatrix} - \begin{bmatrix} \mathbf{0} & \mathbf{0} \\ \mathbf{0} & \bar{\mathbf{F}}^T\bar{\mathbf{Y}}\bar{\mathbf{F}} \end{bmatrix} + \begin{bmatrix} \bar{\mathbf{Q}}_1 & \mathbf{0} \\ \mathbf{0} & \bar{\mathbf{Q}}_2 \end{bmatrix} = \begin{bmatrix} \bar{\mathbf{P}}_{11} & \bar{\mathbf{P}}_{12} \\ \bar{\mathbf{P}}_{21} & \bar{\mathbf{P}}_{22} \end{bmatrix}, \quad (\text{B.11})$$

which shows that  $\bar{\mathbf{P}}_{12} = \bar{\mathbf{P}}_{21} = \mathbf{0}$  and  $\bar{\mathbf{P}}_{11} = \bar{\mathbf{P}}_{11}^T = \bar{\mathbf{Q}}_1$ . From these considerations, and (B.8), it can be reasoned that

$$\bar{\mathbf{F}}^T\bar{\mathbf{P}}\bar{\mathbf{F}} = \bar{\mathbf{A}}_1^T\bar{\mathbf{Q}}_1\bar{\mathbf{A}}_1 + \bar{\mathbf{A}}_2^T\bar{\mathbf{P}}_{22}\bar{\mathbf{A}}_2 \quad (\text{B.12})$$

and, from (B.5) and (B.9) results that

$$\begin{aligned} \bar{\mathbf{F}}^T\bar{\mathbf{Y}}\bar{\mathbf{F}} &= \begin{bmatrix} \bar{\mathbf{A}}_1^T & \bar{\mathbf{A}}_2^T \end{bmatrix} \begin{bmatrix} \bar{\mathbf{Q}}_1 & \bar{\mathbf{B}}_1 \\ \bar{\mathbf{P}}_{22} & \bar{\mathbf{B}}_2 \end{bmatrix} \left[ \bar{\mathbf{R}} + \bar{\mathbf{B}}_1^T\bar{\mathbf{Q}}_1\bar{\mathbf{B}}_1 + \bar{\mathbf{B}}_2^T\bar{\mathbf{P}}_{22}\bar{\mathbf{B}}_2 \right]^{-1} = \\ &= \underbrace{\begin{bmatrix} \bar{\mathbf{A}}_1^T\bar{\mathbf{Q}}_1\bar{\mathbf{B}}_1 & \bar{\mathbf{A}}_2^T\bar{\mathbf{P}}_{22}\bar{\mathbf{B}}_2 \end{bmatrix}}_{n \times pm} \underbrace{\left[ \bar{\mathbf{R}} + \bar{\mathbf{B}}_1^T\bar{\mathbf{Q}}_1\bar{\mathbf{B}}_1 + \bar{\mathbf{B}}_2^T\bar{\mathbf{P}}_{22}\bar{\mathbf{B}}_2 \right]^{-1}}_{pm \times pm} \underbrace{\begin{bmatrix} \bar{\mathbf{B}}_1^T\bar{\mathbf{Q}}_1\bar{\mathbf{A}}_1 & \bar{\mathbf{B}}_2^T\bar{\mathbf{P}}_{22}\bar{\mathbf{A}}_2 \end{bmatrix}}_{pm \times n}. \end{aligned} \quad (\text{B.13})$$

Denote

$$\hat{\mathbf{A}} = \bar{\mathbf{A}}_2, \hat{\mathbf{B}} = \bar{\mathbf{B}}_2, \quad (\text{B.14a})$$

$$\hat{\mathbf{Q}} = \bar{\mathbf{Q}}_2 + \bar{\mathbf{A}}_1^T\bar{\mathbf{Q}}_1\bar{\mathbf{A}}_1 \in \mathbb{R}^{n \times n}, \quad (\text{B.14b})$$

$$\hat{\mathbf{R}} = \bar{\mathbf{R}} + \bar{\mathbf{B}}_1^T\bar{\mathbf{Q}}_1\bar{\mathbf{B}}_1 \in \mathbb{R}^{pm \times pm}, \quad (\text{B.14c})$$

$$\hat{\mathbf{S}} = \bar{\mathbf{A}}_1^T\bar{\mathbf{Q}}_1\bar{\mathbf{B}}_1 \in \mathbb{R}^{n \times pm}, \text{ and } \quad (\text{B.14d})$$

$$\hat{\mathbf{P}} = \bar{\mathbf{P}}_{22}. \quad (\text{B.14e})$$

Finally, the right lower block of (B.11) can be rewritten, using (B.12)-(B.14), as

$$\hat{\mathbf{A}}^T \hat{\mathbf{P}} \hat{\mathbf{A}} - \underbrace{\left( \hat{\mathbf{A}}^T \hat{\mathbf{P}} \hat{\mathbf{B}} + \hat{\mathbf{S}} \right)}_{n \times pm} \underbrace{\left( \hat{\mathbf{B}}^T \hat{\mathbf{P}} \hat{\mathbf{B}} + \hat{\mathbf{R}} \right)^{-1}}_{pm \times pm} \underbrace{\left( \hat{\mathbf{B}}^T \hat{\mathbf{P}} \hat{\mathbf{A}} + \hat{\mathbf{S}}^T \right)}_{pm \times n} + \hat{\mathbf{Q}} = \hat{\mathbf{P}}. \quad (\text{B.15})$$

In this section, the main result of Yang (2018) discussed in Chapter 4 was derived: the solution to the augmented Riccati equation (4.13) is given by  $\bar{\mathbf{P}} = \text{diag}(\bar{\mathbf{Q}}_1, \hat{\mathbf{P}})$ , where  $\hat{\mathbf{P}} \in \mathbb{R}^{n \times n}$  is the solution to the Riccati equation (4.15).

### B.3 Structure of the augmented state feedback matrix

This section aims to prove the following theorem, which makes the computation of the augmented state feedback matrix  $\bar{\mathbf{K}}$  more efficient and derives its very specific structure, in which the first  $(p-1)n$  columns are null.

**Theorem 1.** *The optimal feedback law for the lifted system can be written as  $\bar{\mathbf{u}}_k = - \left[ \mathbf{0}_{pm \times (p-1)n} \mid \hat{\mathbf{K}} \right]$ , where  $\hat{\mathbf{K}} \in \mathbb{R}^{pm \times n}$  is the optimal state feedback matrix associated with the Riccati equation (4.15).*

*Proof.* The optimal feedback law resultant from (4.15) is given as

$$\hat{\mathbf{K}} = \underbrace{\left( \hat{\mathbf{B}}^T \hat{\mathbf{P}} \hat{\mathbf{B}} + \hat{\mathbf{R}} \right)^{-1}}_{pm \times pm} \underbrace{\left( \hat{\mathbf{B}}^T \hat{\mathbf{P}} \hat{\mathbf{A}} + \hat{\mathbf{S}}^T \right)}_{pm \times n}, \quad (\text{B.15})$$

which, using (4.14), can be written as

$$\hat{\mathbf{K}} = (\bar{\mathbf{R}} + \bar{\mathbf{B}}_1^T \bar{\mathbf{Q}}_1 \bar{\mathbf{B}}_1 + \bar{\mathbf{B}}_2^T \bar{\mathbf{P}}_{22} \bar{\mathbf{B}}_2)^{-1} (\bar{\mathbf{B}}_1^T \bar{\mathbf{Q}}_1 \bar{\mathbf{A}}_1 + \bar{\mathbf{B}}_2^T \bar{\mathbf{P}}_{22} \bar{\mathbf{A}}_2). \quad (\text{B.16})$$

Considering (4.12), the optimal feedback matrix for the augmented system is given by

$$\bar{\mathbf{K}} = (\bar{\mathbf{R}} + \bar{\mathbf{B}}^T \bar{\mathbf{P}} \bar{\mathbf{B}})^{-1} \bar{\mathbf{B}}^T \bar{\mathbf{P}} \bar{\mathbf{A}}. \quad (\text{B.17})$$

It can be noted that

$$\begin{aligned} \bar{\mathbf{R}} + \bar{\mathbf{B}}^T \bar{\mathbf{P}} \bar{\mathbf{B}} &= \bar{\mathbf{R}} + \begin{bmatrix} \bar{\mathbf{B}}_1^T & \bar{\mathbf{B}}_2^T \end{bmatrix} \begin{bmatrix} \bar{\mathbf{Q}}_1 & \mathbf{0} \\ \mathbf{0} & \bar{\mathbf{P}}_{22} \end{bmatrix} \begin{bmatrix} \bar{\mathbf{B}}_1 \\ \bar{\mathbf{B}}_2 \end{bmatrix} = \\ &= \underbrace{\bar{\mathbf{R}} + \bar{\mathbf{B}}_1^T \bar{\mathbf{Q}}_1 \bar{\mathbf{B}}_1 + \bar{\mathbf{B}}_2^T \bar{\mathbf{P}}_{22} \bar{\mathbf{B}}_2}_{pm \times pm}, \end{aligned} \quad (\text{B.18})$$

and

$$\begin{aligned} \bar{\mathbf{B}}^T \bar{\mathbf{P}} \bar{\mathbf{A}} &= \begin{bmatrix} \bar{\mathbf{B}}_1^T & \bar{\mathbf{B}}_2^T \end{bmatrix} \begin{bmatrix} \bar{\mathbf{Q}}_1 & \mathbf{0} \\ \mathbf{0} & \bar{\mathbf{P}}_{22} \end{bmatrix} \begin{bmatrix} \mathbf{0} & \bar{\mathbf{A}}_1 \\ \mathbf{0} & \bar{\mathbf{A}}_2 \end{bmatrix} = \\ &= \begin{bmatrix} \mathbf{0} & \dots & \mathbf{0} & \underbrace{\bar{\mathbf{B}}_1^T \bar{\mathbf{Q}}_1 \bar{\mathbf{A}}_1 + \bar{\mathbf{B}}_2^T \bar{\mathbf{P}}_{22} \bar{\mathbf{A}}_2}_{pm \times n} \end{bmatrix}. \end{aligned} \quad (\text{B.19})$$

Substituting (B.18) and (B.19) into (B.17), and comparing the result with (B.16), yields

$$\begin{aligned}\bar{\mathbf{K}} &= (\bar{\mathbf{R}} + \bar{\mathbf{B}}_1^T \bar{\mathbf{Q}}_1 \bar{\mathbf{B}}_1 + \bar{\mathbf{B}}_2^T \bar{\mathbf{P}}_{22} \bar{\mathbf{B}}_2)^{-1} \left[ \underbrace{\mathbf{0} \quad \dots \quad \mathbf{0}}_{pm \times (p-1)n} \mid \underbrace{\bar{\mathbf{B}}_1^T \bar{\mathbf{Q}}_1 \bar{\mathbf{A}}_1 + \bar{\mathbf{B}}_2^T \bar{\mathbf{P}}_{22} \bar{\mathbf{A}}_2}_{pm \times n} \right] = \\ &= \left[ \mathbf{0}_{pm \times (p-1)n} \mid \hat{\mathbf{K}} \right].\end{aligned}\quad (\text{B.20})$$

□

## B.4 Equivalence of the Riccati solutions

This section aims to prove the following theorem, essential to connect the discrete-time periodic Riccati equation and the Riccati equation associated with the augmented time-invariant system.

**Theorem 3.** *The Riccati solution  $\hat{\mathbf{P}}$  is the initial solution  $\mathbf{P}_0$  of the DPRE (4.4).*

*Proof.* The proof follows a similar argument to that of [67]: the optimization problems of (4.1)-(4.2) and (4.7)-(4.11) are identical, therefore, the optimal values of the performance indices  $J$  and  $\bar{J}$  must coincide.

In order to obtain the optimal values of the performance indices, note that

$$\sum_{l=0}^{Np-1} (\mathbf{x}_{l+1}^T \mathbf{P}_{l+1} \mathbf{x}_{l+1} - \mathbf{x}_l^T \mathbf{P}_l \mathbf{x}_l) = \mathbf{x}_{Np}^T \mathbf{P}_{Np} \mathbf{x}_{Np} - \mathbf{x}_0^T \mathbf{P}_0 \mathbf{x}_0. \quad (\text{B.21})$$

Moreover, recall that  $\mathbf{S}_{Np} = \mathbf{P}_{Np}$ . Adding zero to the performance measure of (4.2), in the form of (half of) the difference between the left side and right side of (B.21), results in

$$J = \frac{1}{2} \lim_{N \rightarrow \infty} \left[ \mathbf{x}_0^T \mathbf{P}_0 \mathbf{x}_0 + \sum_{l=0}^{Np-1} (\mathbf{x}_{l+1}^T \mathbf{P}_{l+1} \mathbf{x}_{l+1} + \mathbf{x}_l^T (\mathbf{Q}_l - \mathbf{P}_l) \mathbf{x}_l + \mathbf{u}_l^T \mathbf{R}_l \mathbf{u}_l) \right]. \quad (\text{B.22})$$

The summand of (B.22) can then be rewritten as the perfect square of a norm [55]

$$J = \frac{1}{2} \lim_{N \rightarrow \infty} \left[ \mathbf{x}_0^T \mathbf{P}_0 \mathbf{x}_0 + \sum_{l=0}^{Np-1} \|(\mathbf{B}_l^T \mathbf{P}_{l+1} \mathbf{B}_l + \mathbf{R}_l)^{-1} \mathbf{B}_l^T \mathbf{P}_{l+1} \mathbf{A}_l \mathbf{x}_l + \mathbf{u}_l\|^2 \right]. \quad (\text{B.23})$$

Analyzing (B.23) it can be concluded that the optimal value of the performance index, achieved by selecting the optimal last state feedback law, is  $J_{\text{opt}} = \frac{1}{2} \mathbf{x}_0^T \mathbf{P}_0 \mathbf{x}_0$ . The same process can be applied to the performance measure of the augmented lifted system, resulting in the optimal performance index  $\bar{J}_{\text{opt}} = \frac{1}{2} \bar{\mathbf{x}}_0^T \bar{\mathbf{P}} \bar{\mathbf{x}}_0$ . Since the optimal values of these performance indices coincide, it can be written that

$$\frac{1}{2} \mathbf{x}_0^T \mathbf{P}_0 \mathbf{x}_0 = \frac{1}{2} \bar{\mathbf{x}}_0^T \bar{\mathbf{P}} \bar{\mathbf{x}}_0, \quad (\text{B.24})$$

which, considering the structure of  $\hat{\mathbf{P}}$ , shown in Section B.2, can be developed as

$$\mathbf{x}_0^T \mathbf{P}_0 \mathbf{x}_0 = \left[ \mathbf{0} \mid \mathbf{x}_0^T \right] \begin{bmatrix} \bar{\mathbf{Q}}_1 & \mathbf{0} \\ \mathbf{0} & \hat{\mathbf{P}} \end{bmatrix} \begin{bmatrix} \mathbf{0} \\ \mathbf{x}_0 \end{bmatrix}, \quad (\text{B.25})$$

that is

$$\mathbf{x}_0^T \mathbf{P}_0 \mathbf{x}_0 = \mathbf{x}_0^T \hat{\mathbf{P}} \mathbf{x}_0. \quad (\text{B.26})$$

Since  $\mathbf{P}_0$  and  $\hat{\mathbf{P}}$  are symmetric, it results that  $\hat{\mathbf{P}} = \mathbf{P}_0$ .  $\square$

## B.5 Validation for singular systems

In order to validate the algorithm proposed in Section 4 for systems where  $\tilde{\mathbf{A}}$  is singular, consider the following singular periodic system, with  $p = 3$  (adapted from [56]):

$$\begin{aligned} \mathbf{A}_1 &= \begin{bmatrix} -3 & 2 & 9 \\ 0 & 0 & -4 \\ 3 & -2 & 3 \end{bmatrix} & \mathbf{B}_1 &= \begin{bmatrix} 1 \\ 1 \\ 0 \end{bmatrix} & R_1 &= 1, \\ \mathbf{A}_2 &= \begin{bmatrix} 6 & -3 & 0 \\ 4 & -2 & 2 \\ 2 & -1 & 4 \end{bmatrix} & \mathbf{B}_1 &= \begin{bmatrix} 0 \\ 1 \\ 0 \end{bmatrix} & R_2 &= 2, \\ \mathbf{A}_3 &= \begin{bmatrix} 2 & -3 & -3 \\ 4 & -15 & -3 \\ -2 & 9 & 1 \end{bmatrix} & \mathbf{B}_1 &= \begin{bmatrix} 0 \\ 1 \\ 1 \end{bmatrix} & R_3 &= 1, \end{aligned} \quad (\text{B.27})$$

and  $\mathbf{Q}_l = \mathbf{I}_3$  (for  $l = 1, 2, 3$ ) [56]. For this system,  $\tilde{\mathbf{A}}$  is singular and, in fact, all  $\mathbf{\Pi}_l$  are singular. As a result, the Riccati equation associated with the lifted system equivalent to (B.27) cannot be solved by (4.30). However, it can be solved by implementing [73], or Matlab's `idare` function (that implements [74]), obtaining  $\hat{\mathbf{P}} = \mathbf{P}_0$ . Employing (4.4), the remaining solutions  $\mathbf{P}_l$  can be obtained, and the feedback matrices  $\mathbf{K}_l$  can be computed from (4.3). Consider that  $\mathbf{x}_0 = (1, 1, 1)^T$ . The evolution of the state vector is presented in Figure B.1, employing the last state feedback methodology and the augmented state feedback methodology. As expected, both methodologies can solve the LQR problem for systems with singular  $\tilde{\mathbf{A}}$ . Moreover, it can be noted that the feedback methodologies are equivalent, as no process or sensor noise was considered.

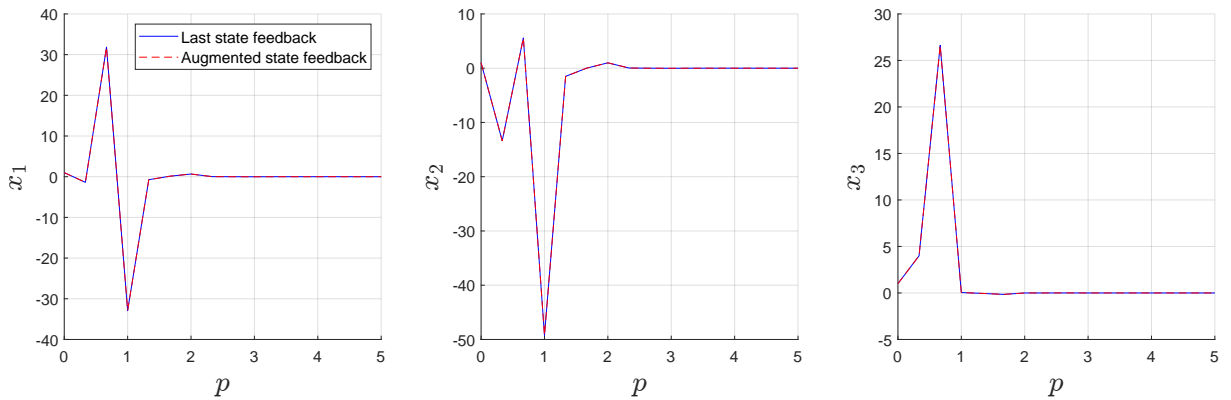


Figure B.1: Evolution of the state vector of a system with a singular  $\tilde{\mathbf{A}}$  matrix.